Fatigue Behaviour of GFRP-Reinforced UHPC Closure Strips in Prefabricated Bridge Deck Applications

by

Benjamin Dow

A thesis

presented to the University of Waterloo

in fulfillment of the

thesis requirement for the degree of

Master of Applied Science

in

Civil Engineering

Waterloo, Ontario, Canada, 2016

Author's Declaration

I hereby declare that I am the sole author of this thesis. This is a true copy of this thesis, including any required final revisions, as accepted by my examiners.

I understand that my thesis may be made electronically available to the public.

Abstract

Accelerated bridge construction techniques allow for bridges to be constructed or replaced more quickly in order to save commuter time and money. One of these techniques involved the use of prefabricated bridge deck panels, which are connected to each other by high strength closure strips. This thesis report investigates the performance of a closure strip filled with ultra-high performance concrete under fatigue loads at service levels as well as at failure loads.

Four nearly full-scale (150 mm deep) bridge deck specimens were constructed, each consisting of two panels connected by a UHPC filled closure strip. Two of the specimens were reinforced with ribbed glass fibre reinforced polymer (GFRP) reinforcing bars and the remaining two were reinforced with sand-coated GFRP bars. One specimen fabricated with each bar type was loaded under fatigue (cyclic) loading equivalent to the maximum wheel load specified in the Canadian Highway Bridge Design Code for 2,000,000 cycles at three locations: the centre of a precast concrete panel, the centre of the closure strip, and adjacent to the closure strip. The remaining specimen of each bar type was only fatigue tested adjacent to the closure strip at the same load level for 2,000,000 cycles. The slabs were then loaded monotonically to failure.

It was found that the specimens generally exhibited noticeably increased deflections during initial fatigue loading followed by a more gradual deflection increase for the remainder of the fatigue loading. The slabs reinforced with the ribbed GFRP bars were found to exhibit significantly larger deflections than the sand-coated bars. The slab with ribbed bars, which was intended to undergo fatigue loading at three locations, experienced failure of the bottom bars during testing at the second fatigue location. Similarly, the specimen with ribbed bars only loaded adjacent to the closure strip also did not complete the planned 2,000,000 cycles due to premature failure of the bottom transverse reinforcement.

When loaded to failure adjacent to the closure strip, both of the specimens reinforced with the sand-coated GFRP bars experienced a punching shear failure. The punching shear failure surface typically has a cone or pyramidal shape. However, the punching cone for both specimens was truncated by the UHPC closure strip, resulting in a three sided failure cone, with slip occurring along the interface between the precast concrete and the UHPC. The specimens reinforced with ribbed bars were also loaded to failure. However, these specimens failed due to

the top fibre of the concrete crushing along the length of the slab due to the lack of bottom reinforcement continuity resulting from the rebar failures during fatigue loading.

Finite element models were generated in ABAQUS to provide an understanding of the general stress patterns experienced throughout the slab. The initial load comparison (model vs. measured) yielded similar results, with the model showing slightly more initial stiffness, but cracking at approximately the same load. In addition, the failure loads were compared to two building and bridge code specifications: CSA S6 and CSA A23.3, and it was found that the punching shear failure for the two sand-coated GFRP reinforced specimens was less than the specified values for each of these design codes due to the punching failure occurring on only three sides of the load instead of the four sides assumed by the codes.

In conclusion, the specimens with sand-coated reinforcement maintained stiffness throughout fatigue loading and failed in a three-plane punching shear mode, and the specimens with ribbed reinforcement failed during fatigue loading when the bottom transverse reinforcement broke, resulting in significant deflections and pre-empting failure by punching shear.

Acknowledgements

At the University of Waterloo, I would like to thank my supervisors Dr. Jeffrey West, P. Eng., and Dr. Scott Walbridge, P. Eng., for their advice and guidance throughout the completion of this research. I would also like to thank Douglas Hirst, Richard Morisson, Rob Sluban, and Adam Felinczak for their assistance in the completion of work within the lab. Additionally, I would like to thank my colleagues Matthew Sjaarda and Taylor Porter for their lab assistance and advice. I would also like to thank Dr. Maria Anna Polak and Dr. Dipanjan Basu for their review of my thesis.

I would like to thank Pultrall for providing the reinforcement for two of the specimens. I would also like to thank Fibreline Composites and Dr. Dritan Topuzi for providing the reinforcement for the remaining two specimens. I would also like to thank LaFarge North America for providing the UHPC as well as the technical support of Mr. Andrew Ross and Mr. Gaston Doiron.

At the Ontario Ministry of Transportation, I would like to thank Dr. David Lai, Head Rehabilitation Engineer, MTO Bridge Office, for his input and advice.

Funding for this research was gratefully received from the Ontario Ministry of Transportation.

To the four people who must read this thesis, sorry.

Table of Contents

List of Figures

1 Introduction

The life cycle of bridge infrastructure includes initial construction, maintenance, repair, and replacement. During each of these activities, road users are negatively impacted through road work requiring detours, which adds significant time to their journey. When constructing or replacing a bridge, this process may take months to years to complete. In order to decrease the time required to construct or replace a bridge, several accelerated bridge construction techniques have been developed. This report will focus on the use of prefabricated bridge deck panels utilized in both initial construction and deck replacement.

Prefabricated bridge decks typically consist of precast concrete panels, which are transported to site and placed on either new or existing girders. Shear pockets are cast into the panels, which allow stud clusters to be housed within. The reinforcement of the panels extends beyond the concrete and overlaps with the reinforcement from the adjacent panel. This creates a joint, or closure strip, which is then filled with some form of concrete or grout. The minimal use of cast-in-place concrete allows for this technique to be completed in as little as 72 hours.

In addition to rapid construction, the longevity of the bridge infrastructure is also of paramount concern. In climates that require the use of chloride-based de-icing materials on bridges and roadways, any metal that is susceptible to corrosion will rapidly lose capacity due to the presence of these corrosion inducing agents. In reinforced concrete elements, loss of bond can also result. For this reason, alternatives to standard black steel reinforcement have been developed. These alternatives include various types of fibre-reinforced polymer and stainless steel reinforcement. The use of glass fibre reinforced polymer (GFRP) bars has grown in popularity due to their high strength-to-weight ratio and their lack of corrosion potential.

1.1 Scope and Objectives

The primary objective of this research is to understand the behaviour of prefabricated bridge decks that utilize GRFP reinforcing, along with an ultra-high performance concrete (UHPC) within their closure strips. The primary interest of this research is to understand the fatigue

performance of the slabs and closure strip connection, with a secondary interest being the ultimate failure load and failure pattern of the slabs following fatigue loading.

The specific objectives of this research are:

1. to construct and test precast concrete panels connected with GRFP reinforcing and a UHPC closure strip under service fatigue loading;

2. to load the precast concrete panels monotonically to failure after fatigue loading;

3. to compare failure results with existing structural design codes; and

4. to construct a finite element model that calculates stresses and strains for a better understanding of the overall slab behaviour.

The precast slab specimens tested in this study were reinforced with sand-coated or ribbed GFRP bars. Two specimens containing each bar type were tested (four in total).

1.1.1 Thesis Organization

This thesis is organized into six chapters and two appendices:

- Chapter 2 provides background information on research related to the current study. It provides information of all aspects of the project, including accelerated bridge construction in general, materials utilized, and mechanics of concrete bridge deck behaviour.

- Chapter 3 provides a detailed outline of the experimental setup used in testing the slabs.

- Chapter 4 is a detailed description of the experimental results including the fatigue and monotonic loading behaviour of the slabs. This chapter also includes materials test results, as well as autopsy results of the specimens following failure.

- Chapter 5 presents the analysis of the test results. This includes analysis using a finite element model generated in ABAQUS, in addition to comparisons of the experimental results to existing code requirements.

- Chapter 6 discusses the experimental and analytical results and evaluates the various effects of changing parameters.
- Chapter 7 summarizes the findings of the research and states conclusions as well as recommendations for future work.
- Appendix A contains supplementary photographs of the autopsied test specimens.
- Appendix B contains calculations of failure based on code requirements.

2 Literature Review

The literature review presented in this chapter summarizes the current state knowledge on the subjects of accelerated bridge construction, precast concrete bridge decks (configurations, failure modes, and reinforcing materials), and the use of ultra-high performance concrete as a closure strip material for full depth precast concrete bridge decks.

2.1 Accelerated Bridge Construction

As highways and bridges age, replacement of their components becomes required to ensure the safety of the road users. However, bridge installation can take a significant amount of time during which the bridge will be out of commission. During construction, road users are required to take detours, which can significantly increase the length of their trip. In order to minimize the amount of time roads are closed due to bridge construction, accelerated bridge construction (ABC) methods have begun to be extensively explored (Culmo, 2011). In addition to decreasing construction time, the quality of materials is increased using accelerated bridge methods since most components of the bridge can be manufactured in a controlled environment (e.g. a precast plant or steel fabrication shop) with higher construction tolerances.

Issa et al. (1995) indicate that in a replacement project can occur with no detour required since half of the bridge deck can be replaced at a time, allowing for the other half of the bridge to remain in use. Additionally, the use of early high strength grouts allow for the replaced deck to be put back into service within a few days of replacement.

This type of construction and deck replacement has been used across North America. Issa et al. (1995) described instances of bridge deck replacement using this method in 14 states and the province of Ontario. Each of these projects required deck replacement due to a variety of issues such as cracking, leaking, and settlement. This report further highlights the requirement that all joints in this type of construction must be designed to decrease cracking due to the increased risk of corrosion and damage from water infiltration.

Another example of this type of construction is the MacKenzie River Twin Bridges in Thunder Bay, Ontario described by Perry, Kriciunas, & Stofko (2014). These are a pair of three-span

bridges with a total span of about 180 metres (m). The bridges were constructed using steel plate girders with precast GFRP reinforced deck panels. The joints between the deck panels and the stud pockets located at the girders were filled with ultra-high performance concrete. At the time of the paper this project was the largest filed cast ultra-high performance concrete connection project in North America.

2.2 Precast Concrete Bridge Decks

Bridge decks are typically the first component of a bridge to deteriorate to the point where complete replacement is required (Biswas, 1986). A full bridge reconstruction is not usually a viable option since typically stringer beams and supports remain in satisfactory condition. Up until the 1980s the only viable replacement option was a new cast-in-place system, which could be very time consuming to install. Eventually it became possible to use partial-depth precast elements with cast-in-place concrete to level the surface and ultimately full-depth precast concrete panels. These full-depth panels came in a variety of shapes including boxes, channel shapes, single tees, and voided slabs (Biswas, 1986). Ultimately, solid full-depth precast panels are now being used in bridge deck replacements with various types of connections to the girders (longitudinal flexural members) or stringers (transverse flexural members).

Two primary types of reinforced concrete bridge decks are those that have post-tensioning forces applied in the direction of traffic to generate normal force at transverse joints and deck systems without post-tensioning to enable faster construction. Issa et al. (2000) tested both non-post tensioned and post-tensioned reinforced concrete bridge deck systems under fatigue and static loading conditions. The deck panels were precast panels measuring 600 mm by 600 mm with shear pockets spaced at 450 mm centre to centre. The slab thickness was 50 mm. The precast concrete had a compressive strength of 49.3 MPa with the polymer concrete utilized within the transverse joints having a compressive strength of 55.1 MPa. The steel reinforcement was wire mesh with a yield strength of 503 MPa. Specimens consisting of nine panels on two beams were fatigue tested under a cyclic concentrated load ranging from 18 to 53 kN based on equivalent AASHTO truck loading. This testing found that in a non-post tensioned system failure occurred at the transverse joint in negative bending over a support whereas post-tensioning delayed initial

cracking, allowing for increased loads to be applied during fatigue testing without cracks initiating.

El-Ragaby and El-Salakawy (2011) performed fatigue tests on a GFRP reinforced deck slab supported by steel girders. These tests includes fatigue testing and ultimate load testing of a 150 mm slab composed of 40 MPa concrete with a span of 1275 mm. A point load of 70 kN applied over a 375 x 250 mm area was used in fatigue testing for a total of 3,000,000 cycles. All slab specimens failed in punching shear at load levels greater than the punching shear load obtained on an unfatigued (control) specimen. Based on this result, they concluded that fatigue loading had little to no effect on the ultimate failure load of the slab.

Bouguerra et al. (2011) performed static tests on various depths of bridge decks reinforced with GFRP bars and steel bars (as a control). Each slab consisted of a single two metre span connected to two girders using 25 mm steel bolts to represent equivalent welded studs. These bolts were cast integrally with the slab and then placed into existing holes in the girders and tightened. A load was applied to the centre of the slab panel over an area of 250 mm x 600 mm. It was found that regardless of the depth of the slab or the reinforcement type, the decks slabs would fail in punching shear. It was concluded that the size of the cracks on the bottom face of the slab was dependent on the reinforcement ratio of bottom transverse reinforcement. All slabs were found to have sufficient ultimate capacity when compared to CAN/CSA S6 (CHBDC, 2013).

2.3 Arch Action

The ultimate strength of retrained reinforced concrete slabs is aided by compressive membrane action. This is a mechanism by which an arching compressive strut forms and thus increases the basic flexural capacity of a slab. Bridge deck slabs have sufficient axial and rotational stiffness at the stringer beams in order to allow for compressive membrane action to occur. This additional stiffness is provided by the shear studs which extend into the deck slab. Because of the formation of the arching thrust, members with compressive membrane action often fail when concrete crushes rather than by failure of the reinforcement (Zheng et al, 2008).

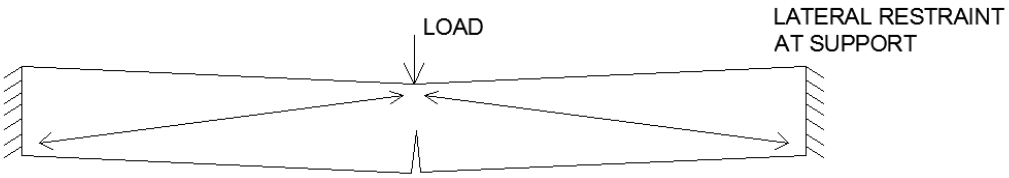

Figure 2-1. Diagram of compressive membrane or arch action.

Taylor & Mullin (2006) performed several experiments of one-way slab strips with conventional steel reinforcement and GFRP reinforcement with the same reinforcement ratio. The slabs were supported using an apparatus to simulate the restraints experienced in a bridge deck with a point load applied at the centreline of the span. This research found that compressive membrane action would be generated in a GFRP slab similar to a steel reinforced slab. It also concluded that the GFRP slabs with restraint performed marginally better than the equivalent steel reinforced slabs in terms of deflection and ultimate strength. However, it concluded that the concrete strength is a greater factor in determining the ultimate strength of a restrained slab rather than the type of reinforcement due to the similar behaviour of the steel and GFRP specimens.

2.4 Punching Shear

Due to the arch action behaviour often exhibited by bridge deck slabs, almost all bridge deck ultimate strength tests end with a punching shear failure mechanism. Several different sources provide recommendations for calculating the punching shear resistance of various types of slabs. Equation (1) is provided in ACI 440 (2006) for calculating the punching shear capacity of FRP-reinforced slabs at columns or under concentrated circular or square loads:

$$V_c = \frac{4}{5}\sqrt{f'_c}\, b_o c \qquad (1)$$

In this equation f'_c is the compressive strength of concrete, b_o is the perimeter of the critical section (in mm) located a distance $d/2$ from edge of the load and c is the cracked transformed section neutral axis depth. The neutral axis depth can be calculated as a function of the FRP

reinforcement ratio, ρ_f, and the modular ratio of the FRP and concrete, η_f, as shown in Equations (2) and (3):

$$c = kd \tag{2}$$

$$k = \sqrt{2\rho_f\eta_f + (\rho_f\eta_f)^2} - \rho_f\eta_f \tag{3}$$

However, this equation has been deemed to be overly conservative by several studies including Bouguerra et al (2011), which found that the expected punching shear capacity was 3.17 times greater than the value predicted by Equation (1). Additionally, Brunton et al (2012) found that Equation (1) was conservative by a factor of approximately 1.9 when testing punching shear in slabs reinforced with FRP grids.

Another empirical punching shear equation that was established through testing done by Matthys and Taerwe (2000) is shown in Equation (4):

$$Q = 1.36\frac{(100\rho f_{cm})^{1/3}}{d^{1/4}}u_{1.5d}d \tag{4}$$

In this equation, Q is defined as the ultimate punching load, ρ is the reinforcement ratio, which can be modified for FRP reinforcement by multiplying by E_f / E_s, f_{cm} is the compressive strength of concrete, $u_{1.5d}$ is the control perimeter a distance of $1.5 \cdot d$ from the edge of the applied load, and d is the depth of the reinforcement. Bouguerra et al (2011) found that this equation was conservative for their tests by a factor of 1.70.

CAN/CSA S6 (CHBDC, 2013) defines the two-way shear resistance of a slab using Equation (5) :

$$V_r = (\phi_c f_{cr} + 0.25 f_{pc})b_o d + V_p \tag{5}$$

In this equation ϕ_c is the reduction factor for concrete used in LSD, f_{cr} is the cracking strength of concrete, f_{pc} is the compressive stress in concrete after prestress losses, b_o is the critical perimeter measured a distance of half the depth of reinforcement, d, and V_p is the shear resistance due to prestressing.

2.5 Shear Connections

The precast concrete deck panels often used in accelerated bridge construction systems are typically placed on either precast concrete girders or steel plate girders. The deck is often designed to behave compositely with the girder below. In order to provide a shear connection between the deck and the girder, in order to achieve composite behaviour, several different details have been proposed and utilized to varying degrees of effectiveness. In general, these details usually consist of groups of headed studs connected to the girder and a corresponding opening in the deck panel, which fits over the stud group. This opening is then filled with a high strength grout in order to provide the composite action between the deck and girder.

The Conestogo River Bridge used 7/8" A235 Type 3 bolts as shear connectors in a cast-in-place deck to allow for movement during the deck prestressing procedure (Dorton et al, 1977). In order to confirm the feasibility of the system, several tests were performed including fatigue and static loading tests. Under static loads, the bolted system did not slip until a load of approximately 86 kN, which was greater than the required 56 kN. After bolt slip, it was found that the bolts would not fail until loaded beyond 200 kN in bearing. Finally, a test subjecting the bolts to 44.5 kN load cycles was performed for 500,000 cycles followed by increasing fatigue loads to 111.2 kN at 1,000,000 cycles followed by an additional 835,000 cycles at 111.2 kN. The bolts did not fail during the fatigue loading tests.

Au et al (2010) performed tests to investigate the suitability of bolted shear connections for precast decks with pockets for each individual bolt connection, which are then grouted. The system utilized through bolts with each bolt being placed within an individual hole which was predrilled into the slab to align with the bolt hole pattern in the girder flange. The test involved single beams with 12 mm diameter A325 bolts spaced at 110 mm. It was concluded that the ultimate strength of the system was not affected by cyclic loading of 30 kN per bolt as specified in CAN/CSA S6 (CHBDC, 2013) and that full composite action was achieved.

Kim and Trejo (2014) performed a number of push off tests on shear connectors in a pocket system filled with grout. The shear connectors used were ASTM A615 3/4 in threaded rods. The testing showed that five different stages existed in the shear connection behaviour during loading: adhesion loss, shear key action, shear key action failure, dowel action of shear

connections, and final failure. Based on this observation, a new equation to calculate the shear resistance of these systems was proposed (see Equation (6)):

$$V_{peak} = c' A'_{cv} + \mu_p (\sum A_{sc} f_y + P_n) \quad (6)$$

In this equation c' is the interlock of the crack surface in the shear pocket, A_{cv} is the interface area of the concrete engaged in shear transfer, μ_p is the coefficient of friction at peak shear force, A_{sc} is the cross-sectional area of shear connector, f_y is the yield strength of the connector and P_n is the permanent normal force in the shear plane.

CAN/CSA S6 (CHBDC, 2013) defines several requirements for the design of shear connectors. These include that a minimum cover of 25 mm must be provided between the top of the connector and the top of the concrete deck. For full-depth precast decks with block-outs for shear connectors the code requires that the precast deck be composed of concrete with a minimum compressive strength of 35 MPa and that the grout used in the shear pockets must have a compressive strength greater than or equal to that of the precast deck but less than 1.3 times the strength of the precast concrete. The code further specifies that stud clusters must be spaced less than 1200 mm apart with individual connectors at least $4 \cdot d$ away from another connector or $1.5 \cdot d$ away from the edge of the pocket, where d is the connector diameter. The strength of each individual connection is to be determined using Equation (7) where the properties for concrete are replaced with the equivalent properties for the grout in the pocket:

$$q_r = 0.5 \phi_{sc} A_{sc} \sqrt{f'_c E_c} \leq \phi_{sc} F_u A_{sc} \quad (7)$$

In this equation F_u is the minimum tensile strength of the steel stud, f'_c is the compressive strength of concrete, E_c is the modulus of elasticity for concrete, and A_{sc} is the cross-sectional area of a stud.

In addition to the ultimate strength requirements, CAN/CSA S6 (CHBDC, 2013) has requirements for the fatigue strength of stud shear connectors. It requires that studs operate within the stress range, τ_{rs}, as defined in Equation (8):

$$\tau_{rs} = 0.52 C_L \frac{V_{sc} Q_s}{A_{sc} I_t n} \quad (8)$$

In Equation 7 C_L is defined to be 1.0 except for when bridges are used for trucks heavier than 625 kN or have frequent heavy trucks, V_{sc} is the range of design shear force at the section of interest, Q is the first moment area of the transformed section at the concrete-to-steel interface, s is the shear stud group spacing, A_{sc} is the cross sectional area of a stud, n is the number of shear studs at the point of interest, and I_t is the transformed section moment of inertia.

2.6 GFRP Reinforcement

Baena et al. (2009) performed pullout tests on a variety of FRP bars to find the influence of surface type and concrete strength on the development length. This study concluded that surface treatment was not of great importance when the bars were embedded in low strength concrete, but in high strength concrete, the surface treatment becomes a controlling factor in the failure mode. It found that a sand coated GFRP develops a chemical bond with the concrete and once its maximum bond stress is reached a sudden drop occurs due to the sand debonding from the bar. Davalos, Chen and Ray (2008) also concluded that the strength of GFRP bars placed in high-strength concrete is governed by the bar failure rather than a concrete failure in pullout tests. Finally, Cosenza et al. (1997) describe the bond failure between a sand coated bar and concrete to be a brittle failure, which should be avoided.

Alves et al (2011) subjected GFRP bars to 1,000,000 cycles at 25% of the ultimate bar load in order to understand the fatigue response of GFRP reinforcing bars in concrete. It was found that fatigue loading resulting is a loss of up to 29% of the bond strength in the sand-coated bars. These tests also included some samples undergoing freeze-thaw cycles in addition to the fatigue loading. These samples showed that the fatigue load had a greater influence on the bond strength than the freeze-thaw cycles.

Esfahani et al (2013) performed tests to find the bond strength of GFRP lap splices in beams. The tests were set up with two varieties of GFRP reinforcement, sand-coated and deformed, in a 40 MPa concrete beam. A lap splice was created in the centre of the beam and a load applied in order to put the bars into tension. The deformed bars always failed by splitting of the bar

whereas two of the sand-coated specimens failed by pullout, indicating a poor bond. This test also concluded that the bond strength in a lap splice is not affected greatly by the concrete strength and that sand-coated bars were unaffected by transverse reinforcement.

Wambeke and Shield (2006) proposed Equation (9) to calculate the bond strength in a lap splice. In this equation, u is the bond strength, f'_c is the concrete compressive strength, C is the lesser of the cover to the centre of the bar and half of the bar spacing, d_b is the diameter of the bar, L_d is the embedment length inside the concrete, and α is a factor to account for top bar effect:

$$\frac{u}{0.083\sqrt{f'_c}} = \frac{1}{\alpha}(4.0 + 0.3\frac{c}{d_b} + 100\frac{d_b}{L_d}) \quad (9)$$

2.7 Ultra-High Performance Concrete

Ultra-high performance concrete (UHPC) is a type of concrete with increased modulus of elasticity, compressive strength, and tensile strength, as well as increased durability (Graybeal, 2007). The use of steel fibres mixed into the concrete creates a matrix of tensile load resisting elements within the concrete member. These fibres allow for a reliable post-cracking tensile strength to be achieved. The concrete contains no coarse aggregate and a very low water-to-cement ratio. Table 2-1 illustrates a typical UHPC concrete mix used by Graybeal (2007).

Table 2-1. Typical UHPC mixture (Graybeal, 2007).

Material	Amount (kg/m^3)	Percent by weight
Portland Cement	710	28.5
Fine Sand	1020	40.8
Silica Fume	230	9.3
Ground quartz	210	8.4
High-range water-reducing admixture	31	1.2
Accelerator	30	1.2
Steel fibres	156	6.2
Water	110	4.4

2.7.1 UHPC Mechanical Properties

UHPC has superior mechanical properties when compared to typical concrete. For this reason several considerations must be taken into account when calculating the expected mechanical properties of the material. The modulus of elasticity can be calculated using either Equation (10) (ACI 363R) or Equation (11) (Ma et al, 2004) in which f'_c is the compressive strength of the UHPC determined using a cylinder test:

$$E = 3320\sqrt{f'_c} + 6900 \text{ (in MPa)} \tag{10}$$

$$E = 19000\sqrt[3]{\frac{f'_c}{10}} \text{ (in MPa)} \tag{11}$$

Graybeal (2007) tested steam cured and untreated UHPC samples in order to determine the actual modulus of elasticity and found that Equation (12) provided a more accurate representation of the actual elastic modulus. However, both Equations (10) and (11) were fairly close to the real elastic modulus as well. Graybeal also provided Equation (13) as a means to calculate the expected compressive strength of UHPC at any time after 0.9 days (t in days):

$$E = 3840\sqrt{f'_c} \tag{12}$$

$$f'_{c,t} = f'_c[1 - \exp(-(\frac{t-0.9}{3})^{0.6})] \tag{13}$$

Graybeal (2007) indicates that the mixture described in Table 1 reaches a compressive strength of approximately 70 megapascals (MPa) within 2 days of placement. It was also noted that the UHPC stress-strain behaviour remains with 5% of linear elastic up to 80% of its ultimate strength. Additionally, it was concluded that the peak stress occurs at only a slightly higher strain than the maximum strain expected from normal strength concrete.

2.7.2 UHPC Durability

Graybeal and Tanesi (2007) performed a variety of tests on UHPC samples in order investigate the durability of UHPC in various applications. One of the tests was a freeze-thaw degradation

resistance test described in ASTM C 666-03 (ASTM, 2003) in which the UHPC samples were exposed to temperatures ranging from -18°C to 4.4°C. The UHPC samples were able to maintain 96% of their elastic moduli after samples were subject to 690 freeze-thaw cycles indicating good freeze-thaw resistance. Additionally, UHPC samples were subjected to abrasion testing using the method set forth in ASTM C 944-99 (ASTM, 1999). These tests found that samples subjected to steam curing were practically unchanged by abrasion tests while untreated samples lost about 10 times more weight than the steam cured samples. UHPC samples were exposed to the scaling resistance test described in ASTM C 672-03 (ASTM, 2003). This test involves exposing the samples to a calcium chloride solution and changing the temperature between -18°C and 23°C. Each type of curing showed that after 95 freeze-thaw cycles, little to no scaling occurred.

Samples cured using various methods were subjected to the Electrical Indication of Concrete's Ability to Resist Chloride Ion Penetration set out by ASTM C 1202-05 (ASTM, 2005). It was found that chloride permeability was either negligible or very low regardless of the curing procedure. Chloride ion penetration testing was also completed in accordance to the AASHTO T259-80 (AASHTO, 1980) specification. After being subjected to a 3% chloride solution for 90 days samples were obtained at various depths of the test cylinders to determine the chloride penetration. The tests found that the volume of chlorides penetrating UHPC is extremely low. Finally, the test described in ASTM C 1260-05 (ASTM, 2005) was used to test the alkali-silica reaction in the UHPC samples. The tests resulted in the conclusion that alkali-silica reactions should not be a concern with UHPC due to its low permeability preventing water infiltration for the reaction to occur (Graybeal & Tanesei, 2007).

2.7.3 UHPC Fatigue

Graybeal and Hartmann (2003) performed flexural fatigue tests on small scale UHPC sample prisms. The first set of fatigue tests were run on precracked specimens, which resulted in fatigue failures of the embedded fibres at ranges from 9,950 to 129,700 cycles. The failure occurred when the steel fibres ruptured due to the fatigue loading. The second set of fatigue tests were performed on uncracked specimens and showed that under fatigue loads the cracking stress of the UHPC was lower than the expected cracking stress under a static load case.

Ocel and Graybeal (2007) performed tests on a prestressed UHPC I-girder, which was subjected to fatigue loads. The girder was cast completely of UHPC with a height of 36 inches (914 mm) and a bottom bulb width of 18 inches (457 mm). The girder spanned 168 inches (4.27 m). The girder was exposed to a shear load of 170 kips (756 kN) for 12 million cycles. During this test Ocel and Graybeal observed that shear cracking had occurred but no significant failure.

2.8 Previous UHPC Joint Tests

Gar et al (2013) tested full-scale 2-span prestressed aramid fibre-reinforced polymer (AFRP) reinforced, non-post-tensioned slabs under static loads. In order to model the actual behaviour of the bridge deck, realistic support conditions were provided and a 150 mm panel-to-panel seam consisting of 38 MPa concrete. This study found that the deck was satisfactory for both strength and serviceability under the loads specified in AASHTO LRFD 2010 (AASHTO, 2010). Under static loads it was found that the seam provided sufficient shear capacity and allowed for cracks to propagate through to the non-loaded panel.

The precast concrete deck panels utilized in accelerated bridge construction are often reinforced with glass fibre reinforced polymer (GFRP). This reinforcement increases the durability of the deck as it does not corrode under the harsh conditions seen during the lifespan of the bridge deck. Under fatigue loading, Kumar & GangaRao (1998) found that bridge decks reinforced with GFRP degraded at a similar rate to steel reinforced bridge decks. It was also concluded that 2,000,000 cycles could be considered as 80% of the fatigue life of the deck for a load case designed for the concrete to reach 50% of ultimate compressive capacity and the FRP bars experiencing between 69 MPa and 131 MPa. This can be claimed since the stiffness degradation in the deck was linear until 2,000,000 cycles was reached.

Khalafalla and Sennah (2013) performed static tests on longitudinal joints connecting slab strips. These tests used GFRP reinforcement with a variety of layouts for the closure strip. The bottom reinforcement had headed attachments or bent ends to assist in decreasing the development length of the bars. This testing led to the conclusion that the ultimate load capacity of a GFRP-reinforced slab with a headed bar end in a 125 mm wide closure strip filled with UHPC had about a 27% greater capacity than a similar connection with steel reinforcement. This study also

found that a bent GFRP bar behaved better in non-shrink grout-filled closure strips than a headed bar in a non-shrink grout filled strip.

Au, Lam, and Tharambala (2011) performed tests on UHPC filled closure strips reinforced with steel rebars. This testing used a variety of reinforcement shapes within the closure strip to provide reinforcement continuity. The tests led to the finding that U-shaped, L-shaped, and welded bars provide continuity for steel reinforced closure strips and that early-high strength concrete does not affect the long term joint performance. Additionally, it was found that deflections were increased when a closure strip was present compared to a continuous slab specimen. Finally, it was concluded that steel spirals could be used at the lap location to create an effective full lap length splice, but that vertical stirrups did not provide sufficient confinement to generate an effective full length lap splice within the closure strip.

Lee et al (2011) performed shear strength tests on a bridge joint using a precast strip of UHPC. This precast member utilized either a female-to-female shear key, which would be filled with cast-in-place concrete or a male-to-female connection with the small gap filled with epoxy. Samples were subjected to direct shear. These tests found that the epoxied joint had a greater maximum shear stress of 18.7 MPa versus just 16 MPa for the cast-in-place joint. This showed that the critical shear force would occur either in the cast-in-place concrete or in the epoxy before the UHPC failed.

Au et al. (2011) performed tests on a variety of connections including deformed GFRP and sand-blasted GFRP reinforced precast panels with UHPC filled closure strips in one-way slab strips. The sand-coated bars were used in 225 mm wide strips with lapped top and bottom bars. The specimens were subjected to 2,000,000 cycles of fatigue loading prior to failure. It was concluded that steel reinforcement and GFRP reinforcement were both suitable in the applications tested. It was noted that fatigue loading did not have a great effect on the closure strips, the main failure mode was shear, the UHPC did not affect the overall stiffness of the slab, and its primary advantage in minimizing the size of the closure strip.

Additional tests have been completed on transverse joints with post-tensioning to maintain compression within the joint by Sullivan (2003) and Swenty et al. (2014). The connections

described in these studies are not directly applicable to the joint being investigated in the current study due to the presence of post-tensioning ducts and precompression.

3 Experimental Program

This chapter describes the specimen design and procedures for the laboratory testing. This includes the rationale for selecting the magnitude of the loading, loading locations, and loaded area, as well as the slab section and support system design.

3.1 Specimen Design

This section describes the design of the specimens constructed in order to perform the fatigue and static loading tests. The general layout of the specimen was designed to simulate a full size bridge deck at a somewhat reduced scale suitable for the lab setting. Due to space and loading restrictions, a slab thickness of 150 mm was selected instead of the CSA S6 (2010) standard 225 mm minimum depth for a real bridge deck. Similarly the support girders and shear pockets were designed to provide support and restraints similar to a full sized bridge deck system. Figure 3-1 shows the diagram of the test setup and Figure 3-2 is a photo of the setup, the details of which will be discussed in the following paragraphs.

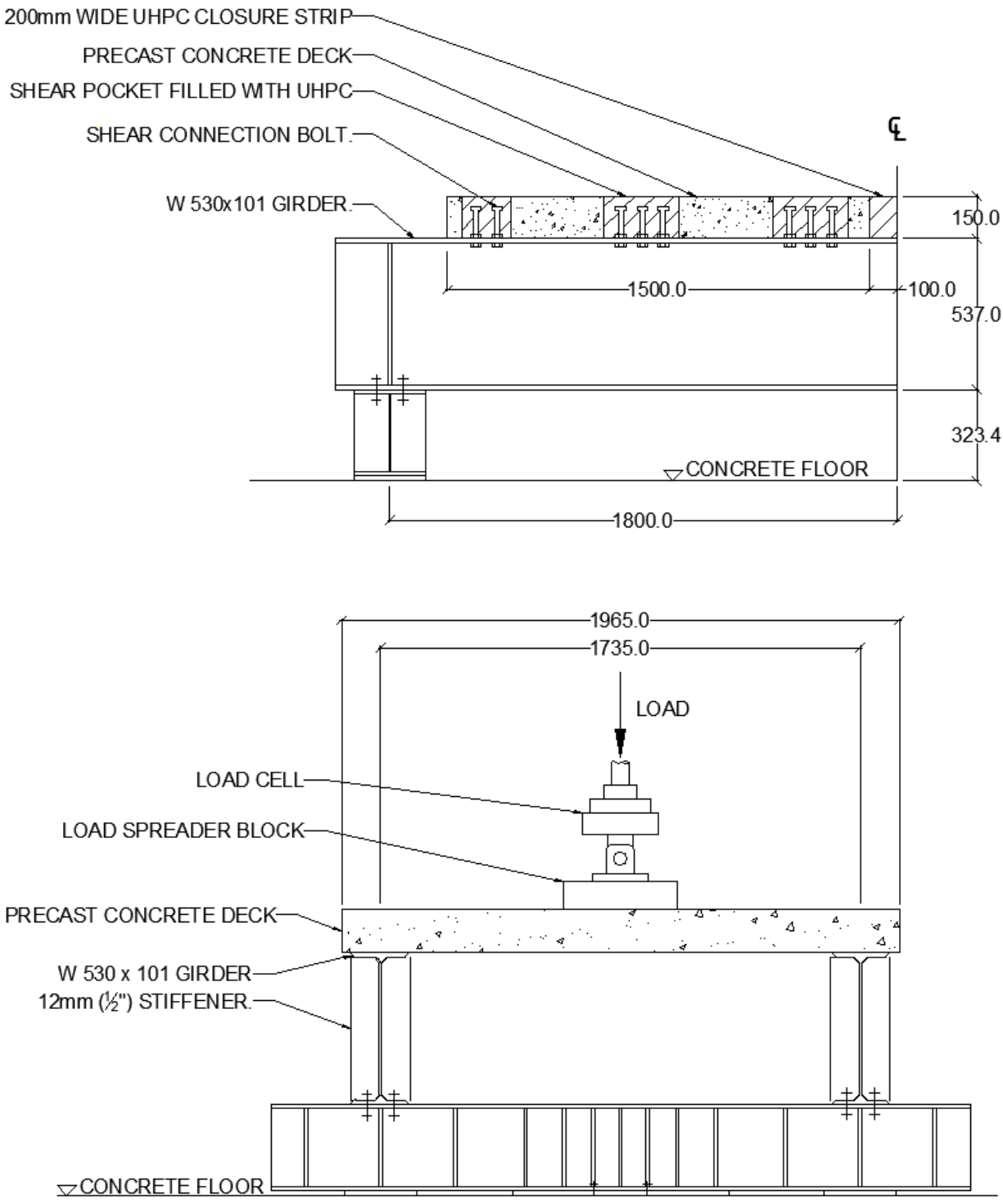

Figure 3-1. Elevations of test setup (dimensions in mm u.n.o.).

Figure 3-2. Photo of the overall test setup including supports.

A total of four specimens were created with two specimens utilizing sand-coated bars and two specimens utilizing ribbed bars. One specimen of each type was fatigued at three locations and the other specimen of each bar type was fatigued at one location adjacent to the closure strip. Table 3-1 shows the test matrix and names for the specimens tested.

Table 3-1. Test matrix of fatigue specimens with specimen names.

	Sand-Coated Bars	Ribbed Bars
3 Fatigue Locations	SB-3	RB-3
1 Fatigue Location	SB-1	RB-1

3.1.1 Material Properties

Two varieties of GFRP reinforcing were utilized in these tests. The first type of bar is a sand-coated bar and the second bar type has a mechanical anchorage system with ribs. Table 3-2 shows the nominal mechanical properties provided by the manufacturers.

Table 3-2. GFRP bar properties as reported by Manufacturer

Bar Type	Sand-Coated	Ribbed
Nominal Area (mm^2)	197.9	201
Tensile Modulus (GPa)	52.5 ± 2.5	>63.5
Nominal Flexural Strength (MPa)	930	>1000
Flexural Strain (%)	1.99	1.67
Nominal Bond Strength (MPa)	14	12.2

The concrete used in the precast concrete decks was designed to be 45 MPa concrete. The first specimen reinforced with the sand-coated bars (Specimen SB-3) was created approximately 18 months prior to the start of testing. The concrete utilized in this specimen was self-consolidating concrete provided by a precast concrete manufacturer. The remaining three specimens were created at the same time using a standard batch of concrete requiring vibration for consolidation. These specimens were all tested within five months. The UHPC used to form the closure strip between the specimen panels was mixed on site in three batches per specimen.

The UHPC utilized was Ductal manufactured by Lafarge North America. Ductal has low water content, no coarse aggregate, and steel fibres embedded within to provide tensile strength. The manufacturer claims that the expected compressive strength of the material to be in excess of 150 MPa with a flexural strength of 20 to 40 MPa. During compressive loading, the material remains linear elastic up to 80% of ultimate load with an elastic modulus ranging from 45 to 55 GPa (Lafarge, 2016).

3.1.2 Slab Design

The GFRP reinforcement was placed in two layers in both the lateral (between girders) and longitudinal (parallel to girders) directions. The lateral bars were placed at a spacing of 300 mm centre-to-centre and terminated approximately 25 mm from the edge of the slab. Longitudinal bars were placed at 250 mm centre-to-centre.. For all specimens the lateral bars were placed below the longitudinal bars in the bottom mat. The top mat for the first specimen (Specimen SB-3) featured the longitudinal bars above the transverse bars. In order to conform to standard bar placement convention, the top mat was subsequently changed for the remaining specimens, with

the transverse layer placed on top of the longitudinal layer. Figure 3-3 shows a plan view and cross section of the reinforcement layout.

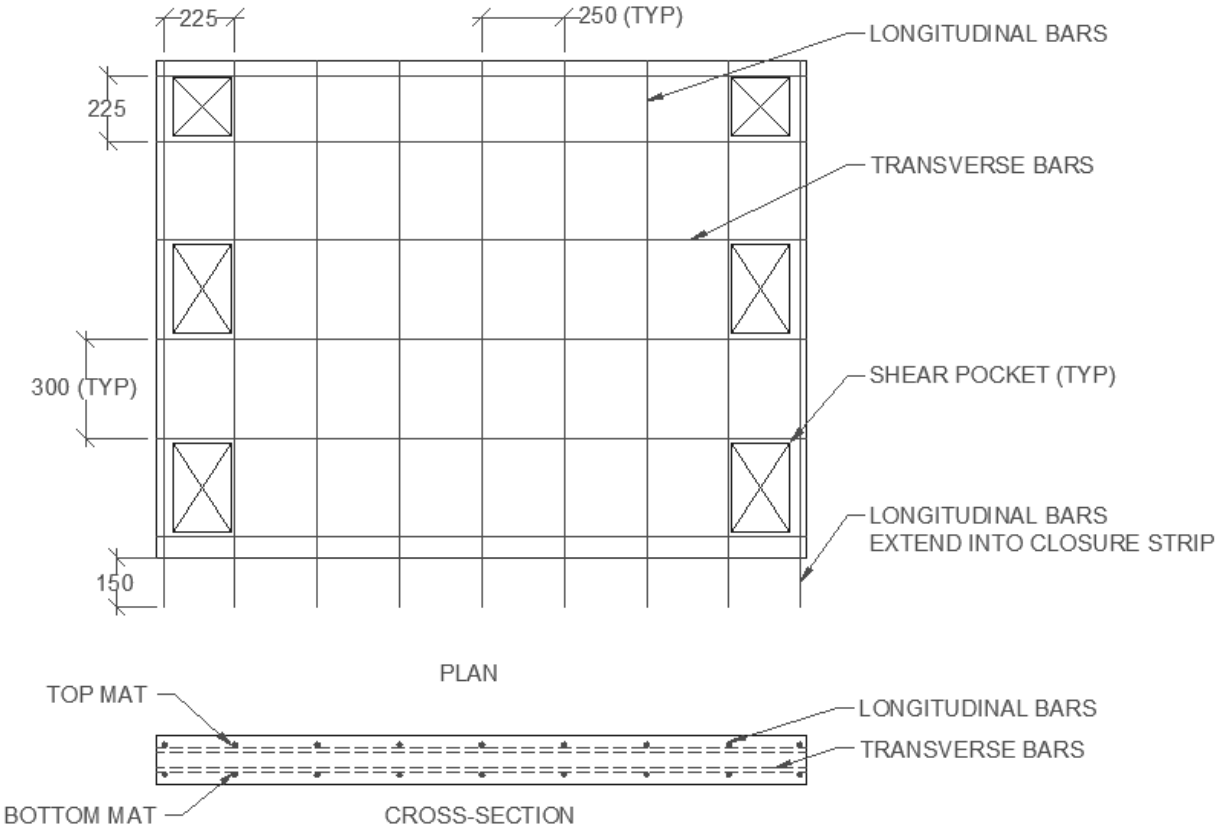

Figure 3-3. Reinforcement layout for panel (plan view and cross-section), mirrored top and bottom.

The top and bottom longitudinal bars extend beyond the edge of the concrete by 150 mm on the edge that would be used to create the transverse joint (closure strip). For Specimen SB-3, foam board was used to create pockets in which shear connections could be created whereas trash cans were used to form the pockets in the other specimens to provide a curved radius to reduce edge cracks and a sloped wall to prevent uplift. All of the larger pockets were 175 mm by 270 mm. The smaller end pockets were 175 mm by 175 mm. The pockets were spaced at 600 mm centre-to-centre. Figure 3-4 shows one slab prior to casting to illustrate the reinforcement layout, extension of bars beyond the face, and the shear pocket trash can forms.

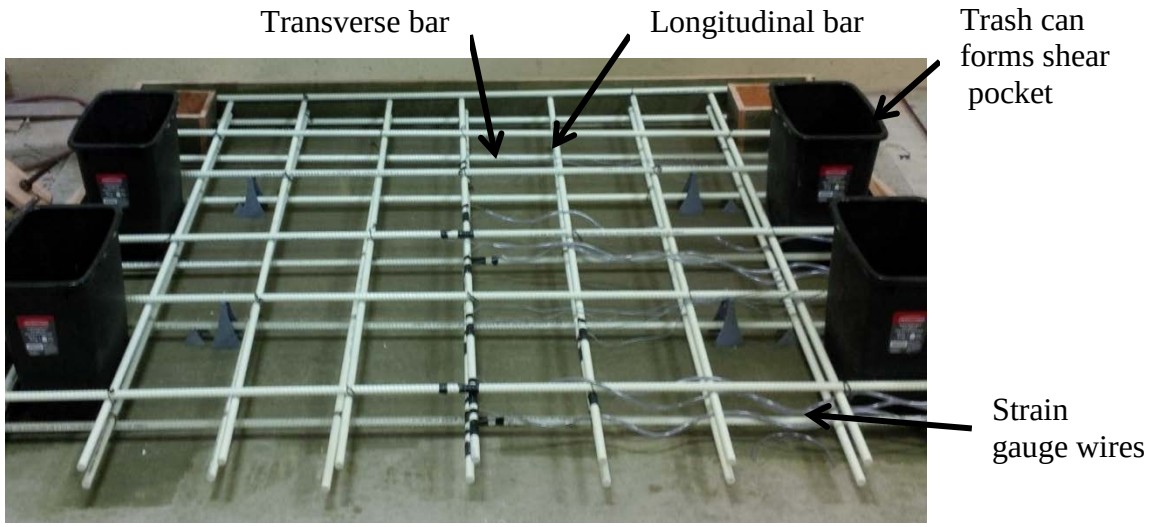

Figure 3-4. Reinforcement prior to concrete casting.

3.1.3 Transverse Joint (Closure Strip) Design

The closure strip was created by putting two precast slabs together so that the exposed GFRP bars had 100 mm of overlap. This created a gap of 200 mm total from the flat face of each slab with the top and bottom bars lapped. Forms were created below the open joint prior to pouring the UHPC. Figure 3-5 and Figure 3-6 shows the joint prior to UHPC being poured.

Figure 3-5. Closure strip with bars overlapped prior to UHPC casting.

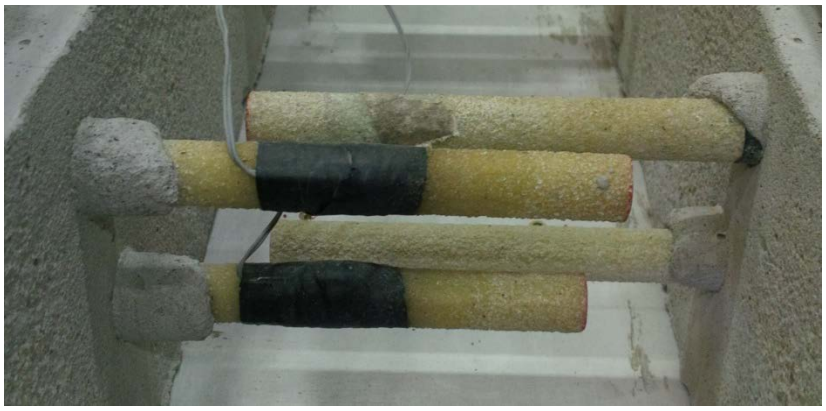

Figure 3-6. Close-up view of sand-coated bars overlapped within the closure strip.

The first sand-coated specimen (Specimen SB-3) was cast with a formed finish on the interior face of the slab (in the closure strip). In order to allow for bond to occur, this face was roughened by sandblasting. Based on input from the UHPC production partner, the remaining three slabs were cast with the interior face roughened by painting the formwork with BASF MasterFinish UC form retarder, which allowed for an exposed aggregate finish with a roughness height of six to ten millimetres. Upon removal of the formwork, the face was agitated with a wire brush to remove excess granular material and sprayed with a pressure washer to remove all loose particles. Figure 3-7 shows a comparison between the finish of the first sand-coated specimen (Specimen SB-3) and the exposed aggregate finish of the remaining three specimens.

Figure 3-7. Comparison of sand-blasted interface and exposed aggregate interface.

The UHPC was poured at one end of the closure strip and allowed to flow down to the other end. This prevents air pockets from forming along the length of the closure strip. Additionally, this

casting method causes the steel fibres to align with the direction of the pour (transverse). This is not ideal, since it can result in a reduced tensile strength in the direction transverse to the closure strip direction. However, until now, no practical solution to this problem has been found, that does not result in other negative impacts. Following the pour, the strip is covered in plastic to prevent a thin crust forming on top of the UHPC. Due to this air escaping and plastic top, the joint finish was rough and pitted with air pockets, for this reason the joint was cast approximately 5 mm higher than the adjacent precast panel faces. The UHPC closure strip was then ground down to provide a level loading area. A photo of the joint casting in progress is shown in Figure 3-8 with the completed joint shown in Figure 3-9.

Figure 3-8. Pouring of UHPC into the closure strip.

Figure 3-9. UHPC filled closure strip left covered during curing.

3.1.4 Shear Pocket Design

In order to correctly model the slab behaviour that would be expected in a real bridge deck with composite girders, shear connections were used to provide similar rotational and axial resistance in the slab. In order to be able to reuse the girders for each test without the need to grind welded studs off of the flange, it was decided that bolts should be used instead of welded studs. These bolts were placed in the stud pockets, which were subsequently grouted with UHPC. After each test was completed, the nuts below the flange were taken off and the slab and bolts were removed as one piece. New bolts were then place in the holes in the girder for the next test. Figure 3-10 shows the bolts in a shear pocket prior to UHPC being poured.

Figure 3-10. Shear bolts within pocket prior to being filled with UHPC.

In order to avoid excessive displacements and damaging the flange of the girder through bearing, the bolts were connected as slip critical connections using the friction force between the girder and the washer as the resisting horizontal force. This method was confirmed to be viable by the studies completed by Au et al (2011). Based on the expected failure load, the required stud pocket resistance was calculated. The friction coefficient associated with Class A coatings was assumed (slip coefficient of 0.33). The bolts were tightened to a torque such that the tensile stress in the bolts was greater than or equal to 70% of the ultimate tensile strength of the bolt (ultimate stress of 830 MPa, bolt stressed to 580 MPa) as specified by CSA S16-09. This information resulted in the use of six ASTM A325 bolts with washers being used in each pocket with the exception of the corner pockets (furthest from the deck joint), which only required four ASTM A325 bolts. Each bolt was designed to withstand a horizontal load of 67.4 kN. Figure 3-11 shows a diagram of the bolted connection.

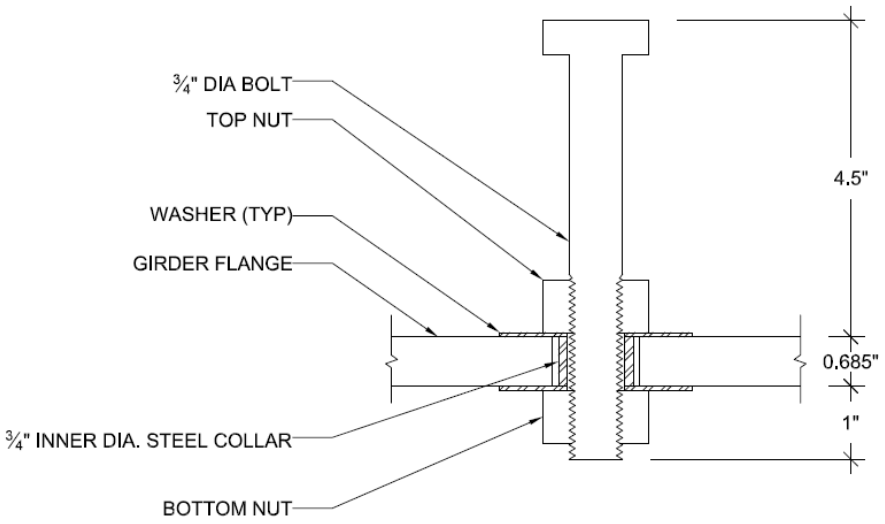

Figure 3-11. Diagram of bolted shear connection.

This connection utilizes a steel collar between the two washers which separates the bolt from the flange. The intent of this collar is to all for easy removal of the system. In the case where a bolt slips, the bolt threads would bite into the collar rather than the flange, allowing for removal to be accomplished without further damage to the cut hole. This requires larger holes to be cut into the flange, but provides security that the slab will be able to be removed from the existing girder without damaging the flange.

3.1.5 Support Design

The support girders were sized to be W530x101 sections in order to ensure that the slab would not be influenced significantly by the deflection or rotation of the girders. These girders were raised off the ground by support beams with a total height of 300 mm, which sat on steel plates attached to the strong floor in the structural testing laboratory. The girders had stiffeners installed at the support points to prevent rotation and the bottom flange was bolted to the support beam to restrict movement. The 300 mm support beam height was required to ensure that the girders could to be located above the base plates in the testing frame without interference.

The support beams were bolted to 19 mm thick central plates which were designed to be compatible with the existing lab anchor points. For each testing location these central plates were bolted into the anchor points to avoid movement. In addition the support beam was

supported below the girders with 250 mm x 300 mm x 19 mm steel plates to act as a direct load path to the strong floor. Figure 3-12 shows this support system including the plates anchored to the ground (strong floor) for the one of the fatigue loading locations.

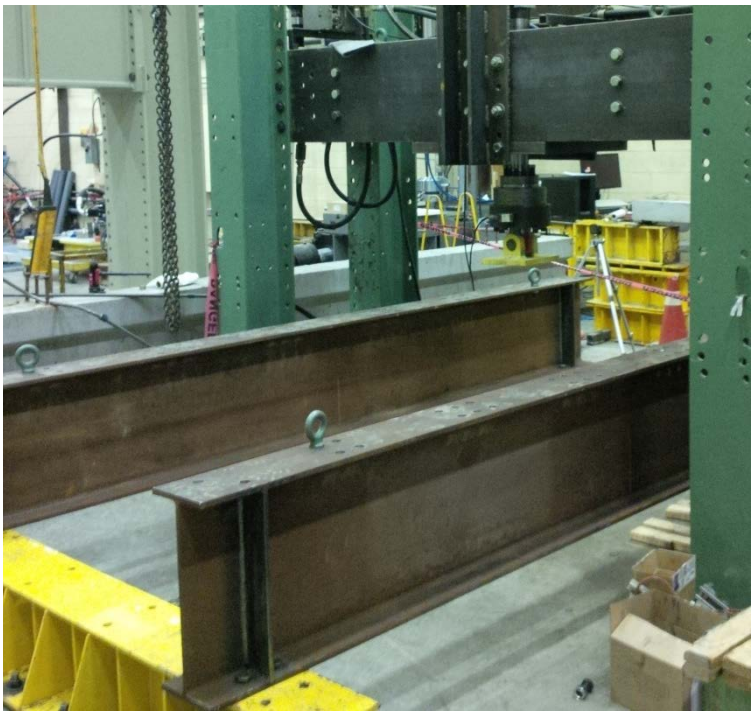

Figure 3-12. Support system prior to slab installation.

3.2 Fatigue Loading

This section describes the rationale for selecting the magnitude of the cyclic fatigue load and the dimensions of the bearing plate through which this loading was introduced.

In order to determine the load and loaded area to use in the tests that would best represent the behaviour of an actual bridge deck slab several models were created. The structural software SAP 2000 was utilized in order to predict the response of stresses in a real bridge deck and in the test specimen. The girders were modelled as frame elements with pinned supports in both cases. The deck was modelled using reinforced shell elements which have layered reinforcement at specified depths. The shear connectors were modelled as rigid links, which connect the slab shell elements to the girder elements.

3.2.1 Real Bridge Deck Model

The real bridge deck model was created based on the typical geometry of full sized bridges built using accelerated construction methods. The deck was assumed to be 225 mm thick, comprised of 40 MPa concrete, and reinforced with GFRP bars at the top and bottom of the slab. The GFRP bar properties used were those described in Section 3.1.1 for sand-coated bars. The bars were spaced at 300 mm centre-to-centre in both the lateral and longitudinal directions top and bottom. The lateral bars were placed closest to the top and bottom faces of the slab with a clear cover of 30 mm. The closure strip was assumed to have bars at the same spacing top and bottom in the longitudinal direction with no lateral bars. The strip was assumed to be 200 mm wide. WWF 1600x431 girders were modelled, with a spacing of 3.1 m centre-to-centre. The UHPC was given the properties provided by Lafarge for Ductal.

CAN/CSA S6 (CHBDC, 2013) specifies that a load of 87.5 kN acting on an area of 600 mm x 250 mm occurs under the wheels on Axle 4 of the CL-625-ONT truck. In addition to this load, the code stipulates that for joint design a dynamic load allowance (DLA) of 0.5 be added onto the initial wheel load. This results in a total load of 131.25 kN. This wheel load was applied to the model for two cases. The first case was for the scenario in which the wheel is centred on the joint and the second case was for the wheel directly adjacent to the joint. The self-weight of the deck was calculated by the program as an area load on the deck and added to the truck wheel load. Figure 3-13 and Figure 3-14 show the stress distribution for the bottom transverse bars and the top concrete section. Note that there are discontinuities away from the loaded area due to some mesh simplifications, but these areas do not represent the maximum stress locations. The maximum bar stress was found to be 6.3 MPa (Tension) while the maximum concrete stress was found to be 5.0 MPa (compression).

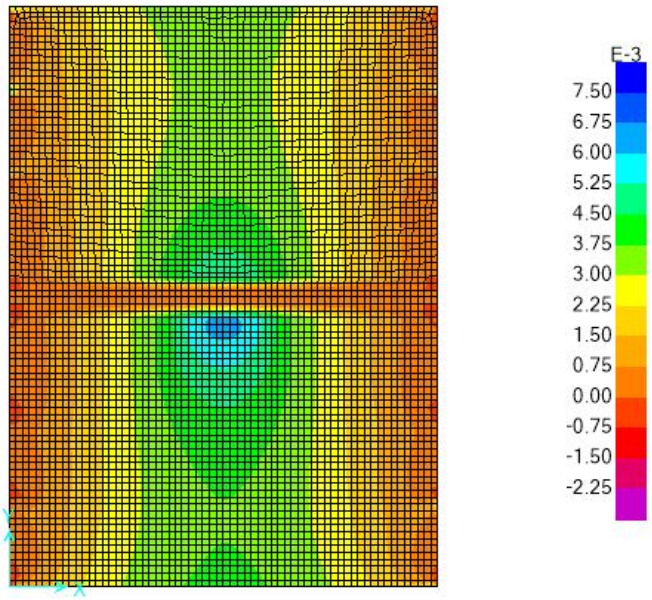

Figure 3-13. Bottom transverse bar stress (in MPa) from real bridge analysis.

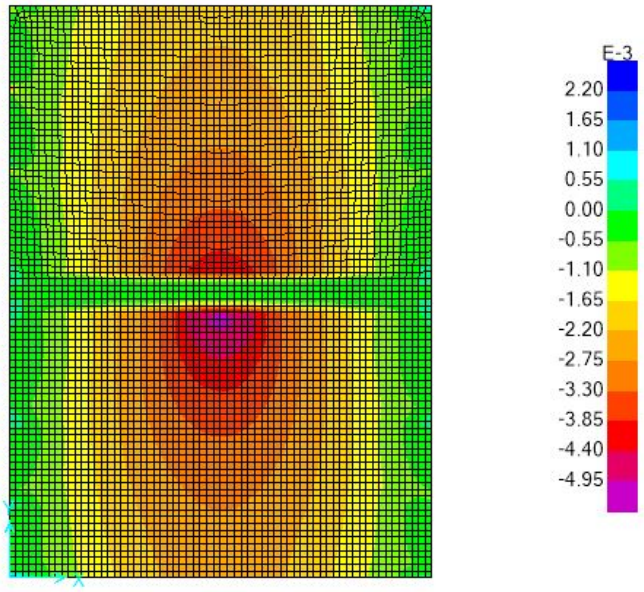

Figure 3-14. Top concrete stress (in MPa) from real bridge analysis.

3.2.2 Test Specimen Model

Using the test specimen dimensions, a model was generated in SAP 2000. In order to determine a fatigue loading that resulted in similar stresses to those observed in the real bridge model,

several loading magnitudes and bearing plate dimensions were investigated. Ultimately it was found that a load of 100 kN applied on a load area of 400 mm x 200 mm produced stresses similar to those experienced in the real bridge model. Figure 3-15 and Figure 3-16 show the stresses in bottom transverse bar and the top concrete surface, respectively. The maximum bar stress was found to be 7.2 MPa (Tension) while the maximum concrete stress was found to be 7.1 MPa (compression).

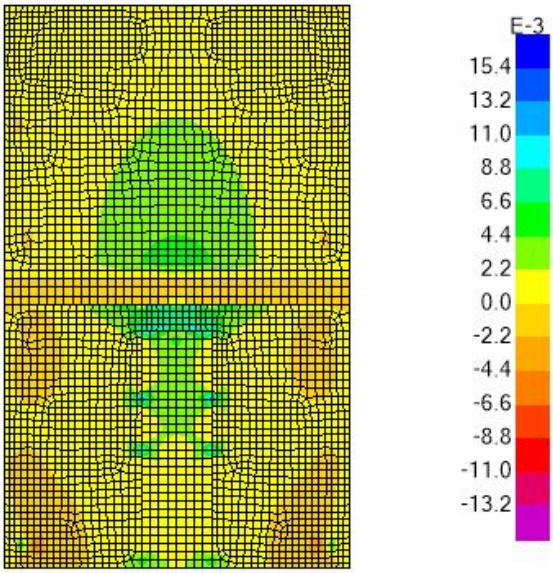

Figure 3-15. Bottom transverse bar (in MPa) from specimen analysis.

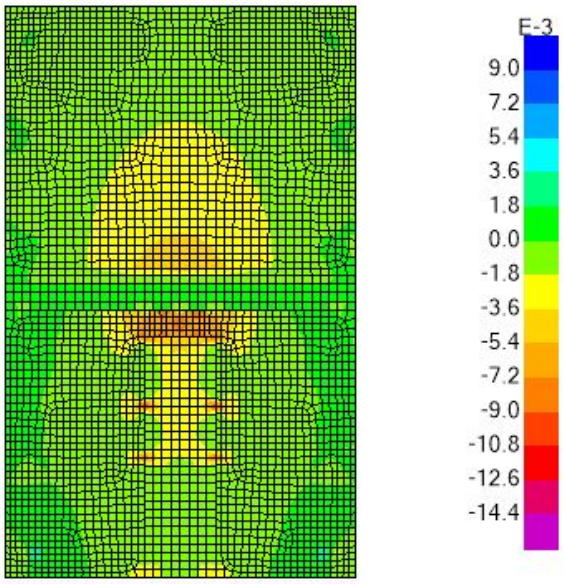

Figure 3-16. Top concrete stress in (in MPa) from specimen analysis.

Note that both models displayed discontinuity due to the preliminary nature of the model and the inability of SAP 2000 to accurately model the interaction between the UHPC closure strip and precast concrete deck. Due to the preliminary nature of the model, the stresses observed were cautiously accepted based on engineering judgement.

3.3 Slab Testing Procedure

Testing was complete using two different procedures. One specimen of each bar type was tested by fatiguing at three locations and the other two specimens (one of each bar type) was only fatigued at the location of maximum concern (adjacent to the closure strip). Loads were applied through a hydraulic actuator attached to a steel block to spread the load. The steel block was 100 mm high x 200 mm wide x 400 mm long. This load spreading block sat directly onto a steel bearing plate with the desired load bearing dimensions of 150 mm x 400 mm.

3.3.1 Fatigue Tests at Three Locations

The slabs were subjected to cyclic loading, with a loading range of ΔP = 100 kN and a load ratio ($R = P_{min} / P_{max}$) of 0.091 on a load area of 400 mm x 150 mm based on the previously-described analysis. Fatigue loading was applied at three locations for each specimen. 2,000,000 cycles of load were applied at each location. The goal of the fatigue testing was to test if the slab with the

closure strip would have similar or better fatigue strength than a continuous deck with no closure strip present. A secondary goal was to see how the fatigue damage and decrease in stiffness resulting from cyclic loading would impact the ultimate capacity of the deck slab. Figure 3-17 shows a diagram of the three locations at which fatigue testing commenced.

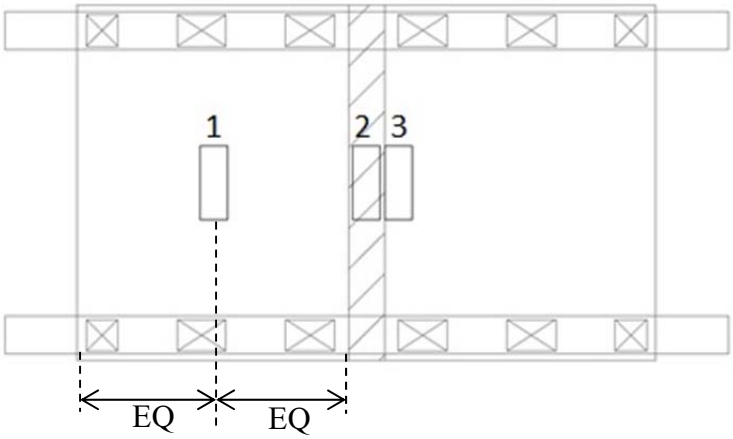

Figure 3-17. Three fatigue loading locations.

The first fatigue location was at the centre of one of the precast panels. This location was selected in order to provide a control location indicating the size of fatigue cracks and the behaviour of a slab with a uniform material. This location was chosen in order to understand how the slab would react to fatigue loading, with the goal in mind that this response could then be compared the observed response to fatigue loading closer to the UHPC joint.

The second location for fatigue loading was centred on the UHPC joint. This location was tested in order to show the fatigue response of the joint and how fatigue cracks impact the UHPC. These cracks and how they cross the interface between the UHPC and the precast panel can then be compared to the size and pattern of fatigue cracks from the other testing locations.

The third fatigue loading location was directly adjacent to the UHPC joint. This location was selected to provide a crack pattern that shows the influence of the UHPC interface on the fatigue response of the precast panel. This pattern will indicate if the interface acts as a barrier and few cracks will propagate into the UHPC or if the interface will be crossed and cracks will appear similar in size and shape to those generated by fatiguing the centre of the precast panel. Additionally, this location provided the maximum shear stress at the UHPC-precast concrete interface according to the SAP 2000 model.

3.3.2 Ultimate Load Tests

Following the fatigue testing, ultimate load (punching shear) tests were attempted at two locations in order to test the ultimate capacity of the slab near the closure strip and the capacity of the precast concrete panel away from the closure strip.

The first location chosen for ultimate load testing was directly adjacent to the UHPC joint. This location corresponds to Location 3 in the fatigue testing program. This location was selected since it generated the greatest stress in the bars in the UHPC joint and would indicate if bar pullout or bond failure within the joint would govern the failure mode after fatigue loading. This location would also show the affect that the UHPC interface has on the punching shear strength of the slab, particularly if the interface would decrease the punching perimeter and thus decrease the punching shear strength. This failure mode and strength could then be compared to the failure at the fatigued panel to show what similarities and differences exist.

The second location for ultimate load testing was the same Location 1 in the fatigue testing program, i.e. at the centre of the precast panel (see Figure 3-17). A failure at this location would indicate the failure type that could be expected from a fatigued deck with little influence from the UHPC joint. This failure point was selected to act as a control and comparison to the failure observed at the first ultimate loading location (Location 3 in Figure 3-17).

3.3.3 Fatigue Tests at One Location

Following the completion of testing for one specimen with each bar type, it was decided that the loading at the centre of the panel (Location 1) had a significant negative impact on the fatigue performance of the closure strip. Therefore, it was decided to eliminate the fatigue loading at Locations 1 and 2. Fatigue loading was only performed at Location 3 at the same load level used previously. During the fatigue loading of these specimens, static tests were performed to obtain load-deflection data periodically throughout fatigue testing to monitor stiffness changes. Following the fatigue loading, the slab was loaded to failure at Location 3.

3.4 Data Acquisition and Controller

In order to capture the changes in the specimen behaviour throughout testing, strain gauges were utilized to capture strains within the bars and on the concrete compressive surface. Additionally, displacement transducers were used to capture the deflections of the slab at various locations. The data acquisition hardware used to capture this data was a National Instruments NI SCXI-1000 with two NI SCXI-1317 cards for strain gauge data collection, one NI SCXI-1300 for displacement transducer data collection, and one NI SCXI-1600 card for collecting data from the controller. The controller utilized to control hydraulic flow, load level, frequency of fatigue loading and deflection during static tests was an MTS 407 Controller. This piece of equipment was used to generate a sine function cycling the load from 10 kN to 110 kN (ΔP = 100 kN) at a frequency of two Hertz (Hz). The minimum load 10 kN was selected to ensure that uplift would not occur, eliminating the potential for the load to be fully removed from the slab. If the load plate separated from the slab, then the sudden impact upon reloading may have caused damage from impact rather than fatigue. During static tests, the load was applied through displacement control at a rate of 2 mm per minute. This mode of loading was selected to avoid sudden actuator movement when the slab failed and the load level dropped.

3.4.1 Strain Gauges

Two types of gauges were used to collect strain data during tests: 60 mm PL-60-11-5L concrete strain gauges and 5 mm FLA-5-11-5L gauges for bar strain. Both strain gauge types had 5 mm wires and a resistance of 120 ohms (Ω). Strain gauges were attached to the GFRP bars by smoothing the area and using epoxy glue. These bar gauges were distributed throughout the slab to capture strains at locations of interest. Locations on the top and bottom mats were mirrored. Figure 3-18 and Figure 3-19 show diagrams of the strain gauge locations.

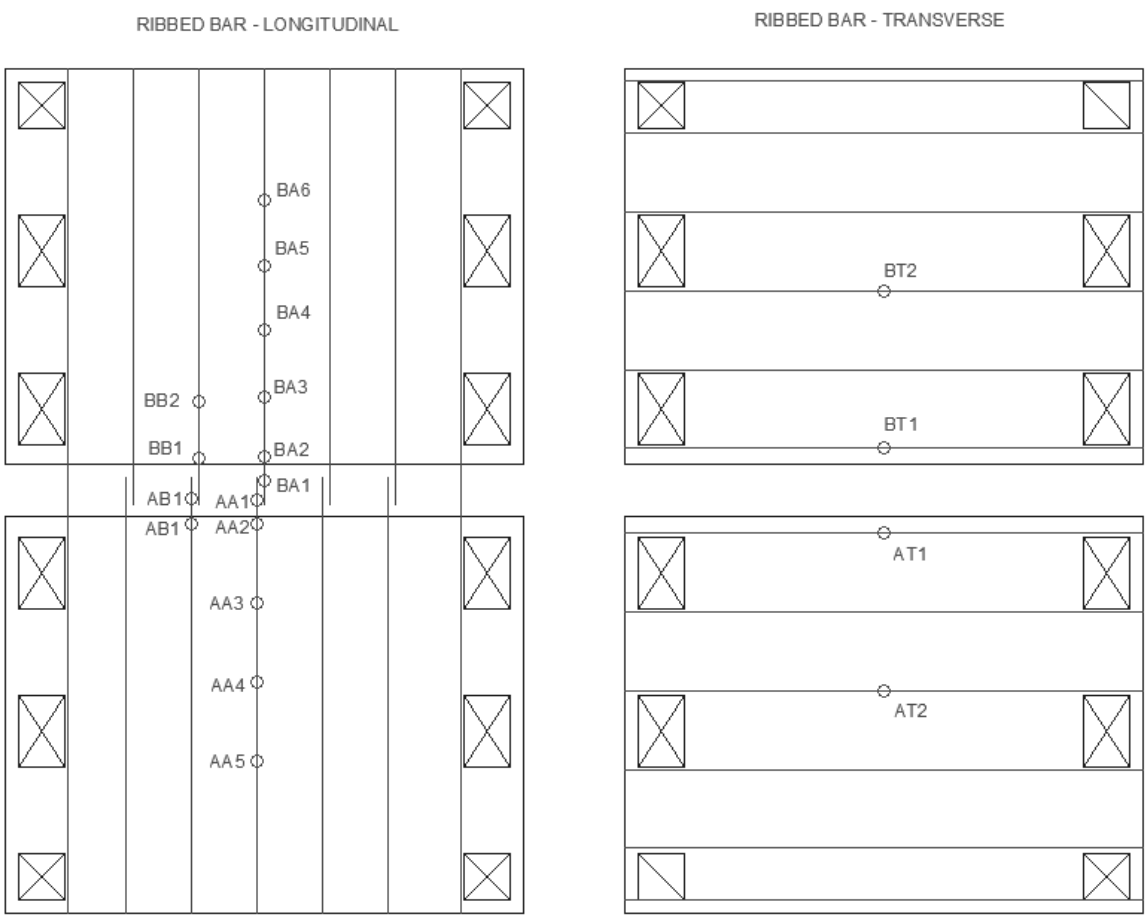

Figure 3-18. Strain gauge layout for specimens with ribbed reinforcing bars.

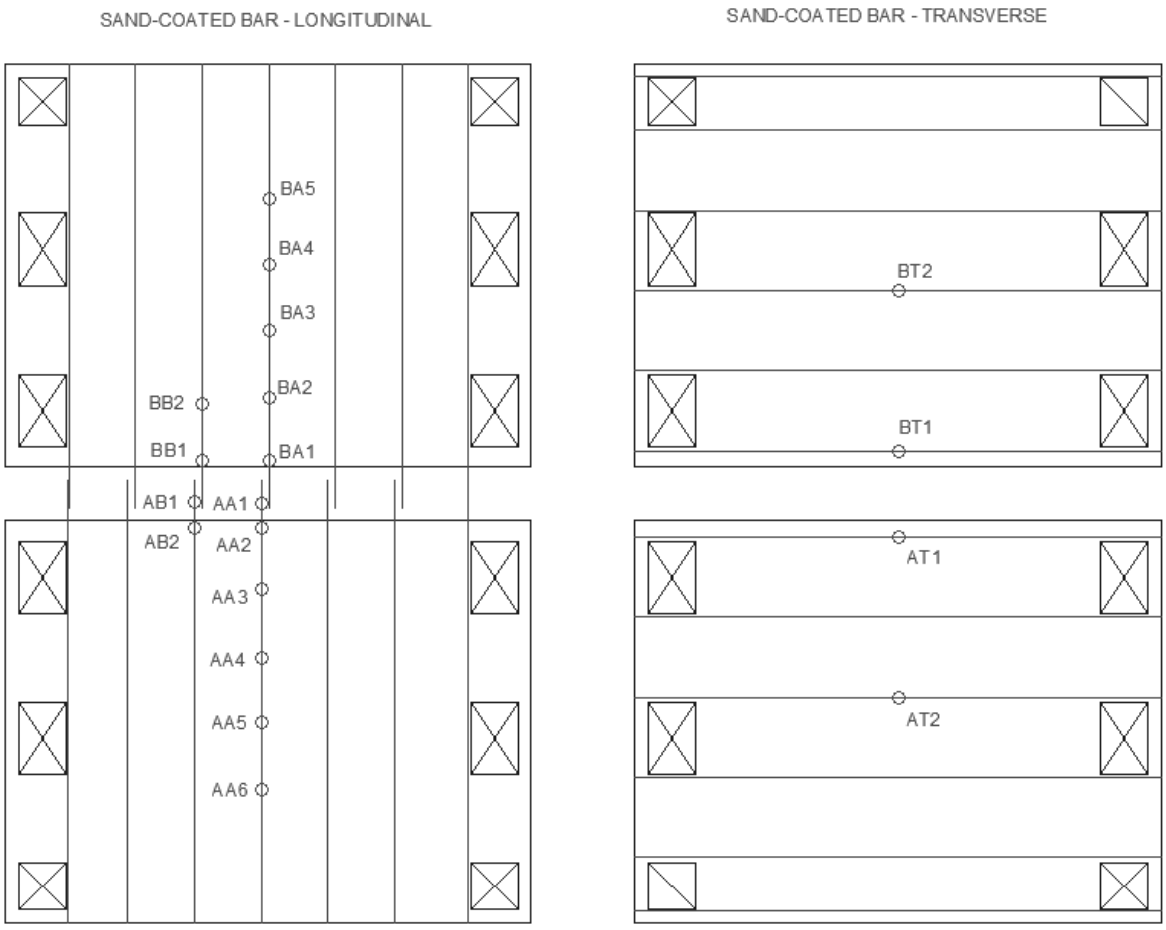

Figure 3-19. Strain gauge layout for specimens with sand-coated reinforcing bars.

Similarly, concrete strain gauges were attached to the surface of the concrete slab using epoxy glue near the load locations. The concrete strain gauges were placed 50 mm from the edge of the load to minimize local distortion from the applied load impacting the strain measurement. Figure 3-20 shows the locations of the concrete strain gauges.

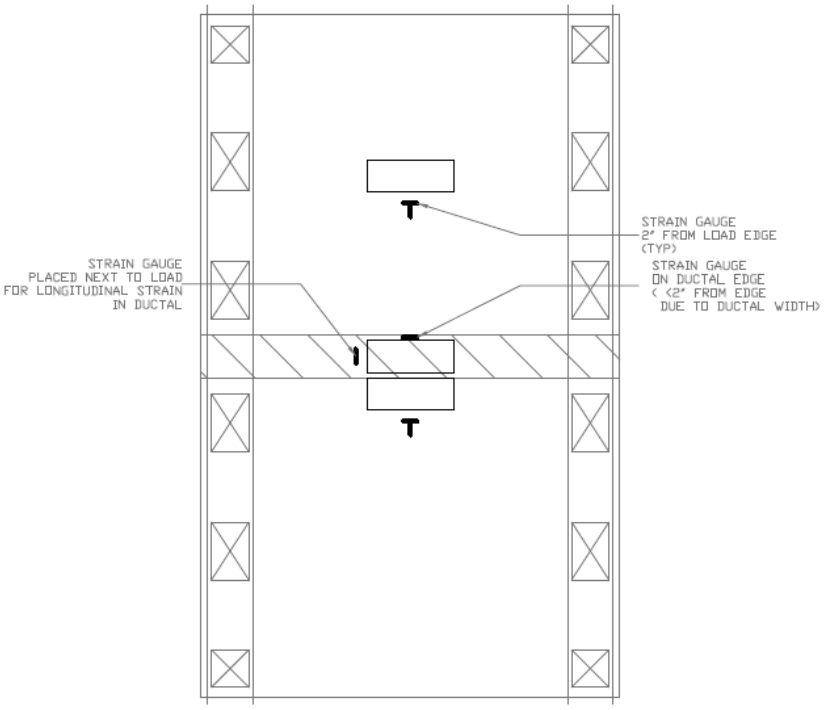

Figure 3-20. Concrete strain gauge locations.

3.4.2 Displacement Transducers

Displacements were recorded using direct current transducers of various lengths. Five displacement transducers were used to capture deflections at significant locations, including: the centreline of the support beam, the centre of each precast concrete panel, the centre of the UHPC closure strip, and directly below the centre of the load applied adjacent to the closure strip (Location 3). Figure 3-21 shows these locations on a diagram of the specimen.

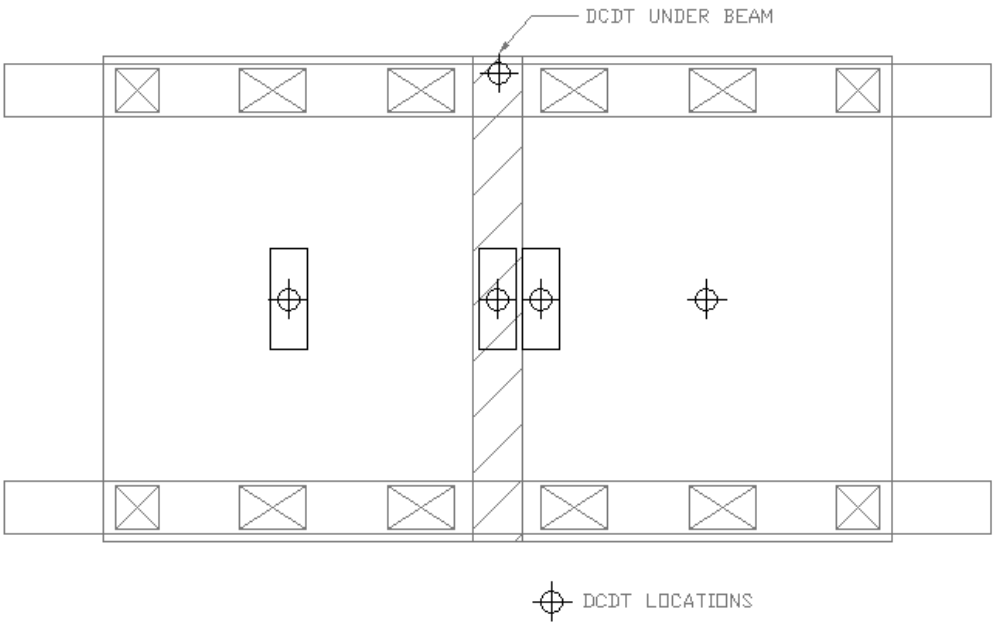

Figure 3-21. Location of displacement transducers.

3.4.3 Data Acquisition Programming

Data recording was performed using NI LabVIEW 2013 with two programs utilized to capture data during testing. The first program was used during fatigue cycling and recorded all data at the valley (10 kN) and peak (110 kN) for each load cycle. This data included all values for strain gauges, displacement transducers, cycle count, time of recording, actuator displacement, and load. The second program similarly recorded all of this information, but was used for static tests and recorded data at set time intervals, rather than certain load levels.

3.5 Ancillary Testing

In addition to the full-scale deck tests, several tests were completed to ascertain the concrete material properties of both the precast concrete and the UHPC.

3.5.1 Compressive Strength

The compressive strengths of both the precast concrete and UHPC were assessed using 100 mm diameter by 200 mm high concrete cylinders which were tested accordance with ASTM C39 (ASTM, 2015). The only difference in testing was that the cylinders for the precast concrete

were loaded at a rate of 0.2 to 0.3 MPa/s as specified by ASTM C39, while the UHPC cylinders were loaded at a rate of 1.0 MPa/s. This increased load rate was suggested by Lafarge due to the high compressive strengths of the UHPC. Figure 3-22 shows a cylinder during loading in the cylinder compression frame.

Figure 3-22. Compressive cylinder test setup.

3.5.2 Splitting Tensile Test

The tensile strength of the precast concrete was determined using a splitting cylinder test. The splitting cylinder test was performed in accordance with ASTM C496 (ASTM, 2011). The load was applied at a rate of 0.7 to 1.4 MPa/min of tensile stress. Figure 3-23 shows a cylinder in the apparatus used for applying load to induce splitting tensile stresses.

Figure 3-23. Split cylinder test setup.

3.5.3 Flexural Tests

Two types of flexural tests were performed on UHPC specimens. The first test was the standard ASTM C1609 (ASTM, 2013) test for the flexural performance of fibre-reinforced concrete prisms. This test utilized third-point loading to ascertain the flexural performance of a concrete prism by applying a constant displacement to the two loaded areas of 0.15 mm/min. This test was used to determine the toughness of the UHPC based on the area under the load-deflection curve. Figure 3-24 shows a specimen in the apparatus used for this test.

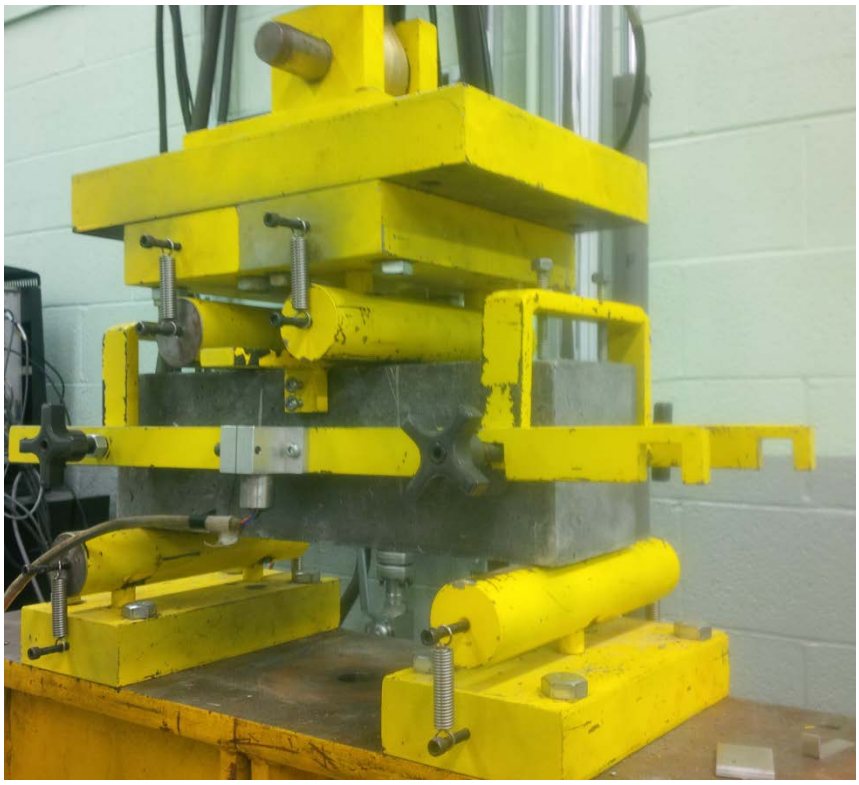

Figure 3-24. ASTM C1609 test setup.

The other test performed on the UHPC prisms was used as an additional measurement of the flexural tensile strength, as well as providing an indication of the fracture energy of the UHPC. The procedure for this test is reported by Butler (2012) based on a similar test procedure, RILEM TC 50-FMC (1985). This test involved using a single point load at the centre of the prism span with a 25 mm deep notch cut into the bottom face directly below the load point. The test was performed using a specified rate of crack opening of 0.15 mm/min based on an externally mounted crack extensometer. The saw cut notch controls the crack location and ensures that the crack occurs directly in the centre with a known fracture area. This allowed for the fracture energy of the concrete to be calculated. Figure 3-25 shows a photo of this test setup.

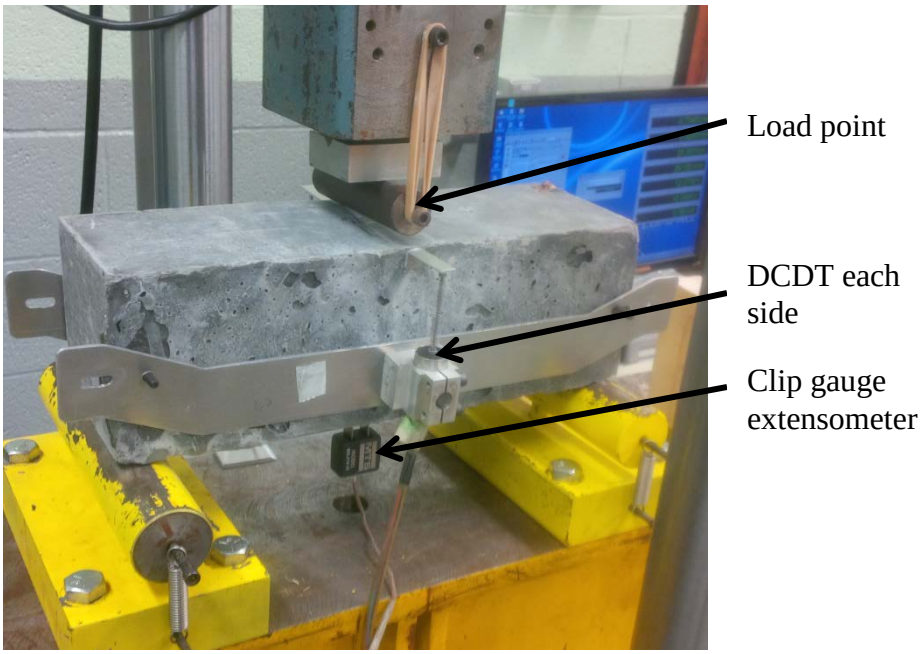

Figure 3-25. Test setup for notched prism test with single point load and crack extensometer below for control.

4 Experimental Results

This chapter presents material testing results as well as the data collected during the testing of the four large-scale precast slab specimens. This includes the slab deflections and strains collected by the data acquisition system.

4.1 Concrete Material Properties

Compressive cylinder tests were performed in accordance with ASTM C39 and the splitting tensile cylinder test was performed in accordance with ASTM C496. Table 4-1 displays the mechanical properties of the concrete.

Table 4-1. Summary of concrete material results.

Specimen	Age at Start of Test (Days)	Average Compressive Strength (MPa)	Average Tensile Strength (MPa)
SB-3	~540	46.5	3.82
RB-3	56		
SB-1	117	41.8	3.70
RB-1	158		

The first casting of Ductal was performed with assistance from a Lafarge technician in order to understand the unique casting procedure for the UHPC. This includes the correct mixing ratios, mixing times, flowability characteristics and pouring procedure. Figure 4-1 shows the UHPC compressive strength gain over time curve for the first specimen.. Table 4-2 shows the compressive properties for the UHPC as tested at both 7 and 28 days after casting.

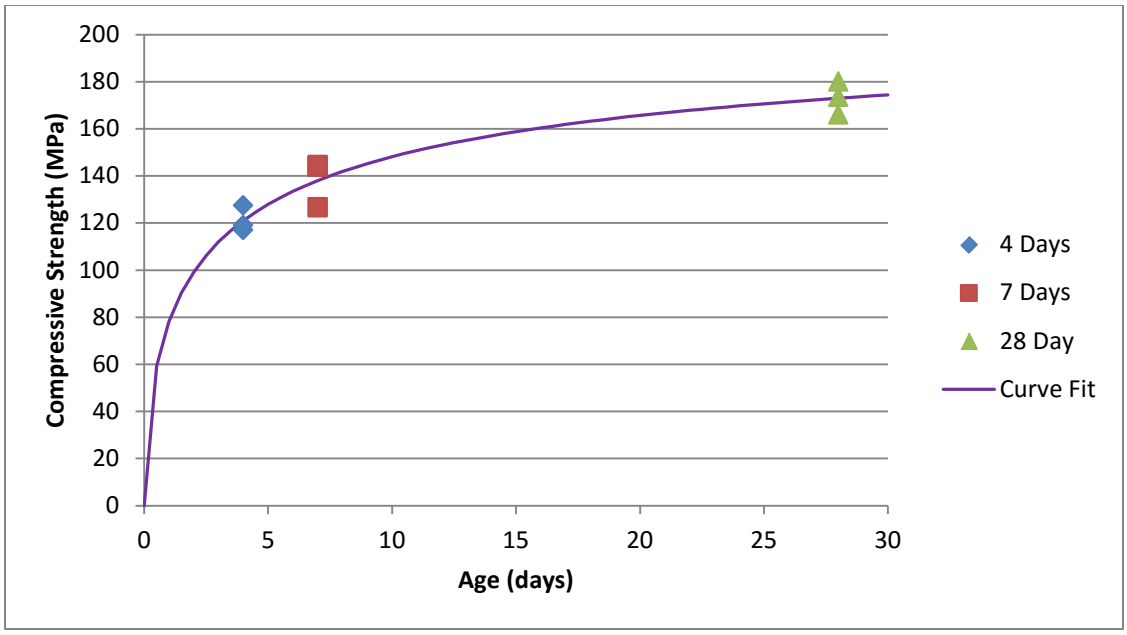

Figure 4-1. Diagram of experimentally determined compressive strength over time for UHPC.

Table 4-2. Summary of UHPC compressive strengths for each specimen

Specimen	7-day Compressive Strength (MPa)	28-day Compressive Strength (MPa)
SB-3	139	173
RB-3	118	170
SB-1	N/A	159
RB-1	121	171

When the cylinders were tested to determine the compressive strength of the UHPC, it was found that they did not break apart like typical concrete cylinders due to the fibres of the UHPC maintaining sufficient integrity to keep the cylinder together. Figure 4-2 shows a broken cylinder that did not break apart as well as half a cylinder that was broken by hitting a failed specimen with a sledge hammer.

Figure 4-2. Broken UHPC cylinders following compressive cylinder tests. (Left: After failure, Right: After failure and sledge hammer)

In addition to the compressive cylinder results, UHPC prisms were tested in order to determine the flexural performance of the UHPC using two slightly different tests. The first test was in accordance with ASTM C1609M.

During this test the load applied was measured using a load cell and the net deflection was measured using two displacement transducers located on each side of the prism. It was found that the average maximum load was 59.1 kN. The corresponding flexural strength was calculated using Equation (14):

$$f = \frac{PL}{bd^2} \tag{14}$$

In this equation, f is the flexural strength (MPa), P is the load (N), L is the span length (mm), b is the width at the point of failure (mm), and d is the depth at the location of failure (mm). Figure 4-3 shows the load versus displacement results for the three specimens tested using this method. One specimen was tested from each batch of UHPC In addition to the flexural strength, the toughness of the UHPC was calculated by calculating the area below the load versus displacement response between zero deformation and L/150, where L is the span length. For the span used of 300 mm, the area calculated for toughness was between 0 mm and 2 mm of

deflection. Table 4-3 show the measured maximum load, approximate area at the location of failure, the flexural strength, and toughness of each of the three specimens tested following these procedures. It was found that the average flexural strength was 15.5 MPa and the average toughness was 83300 N-mm.

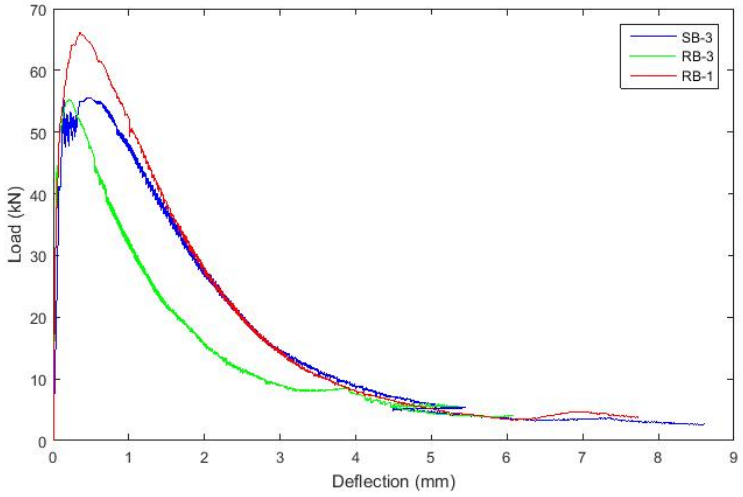

Figure 4-3. Load-deflection response for C1609 prisms. One prism for each batch of UHPC casts.

Table 4-3. Summary of C1609 loads, dimensions, and flexural stress.

Specimen	Max Load, P (N)	Width, b (mm)	Height, d (mm)	Flexural Stress, f (MPa)	Toughness, T^{D}_{150} (N-mm)
P1-SB3	55600	102.8	102.7	15.4	86700
P1-RB3	55400	106.0	105.5	14.1	66500
P1-RB1	66100	105.0	105.5	17.0	96700
			Average:	15.5	83300

The test was stopped after each prism was holding a load of approximately 3 to 4 MPa since it was clear that the steel fibres would continue to hold the two halves together. Figure 4-4 shows a photo of a failed specimen and the irregular failure crack with fibres still crossing the crack.

Figure 4-4. Cracked specimen following C1609 prism test.

The second flexural test used to find the flexural tensile strength of the Ductal was a method reported by Butler (2012). This method utilized a saw-cut notch to control the crack location to accurately find the area of the crack to calculate the fracture energy of the UHPC. The data collected from this test were the applied load and the midspan deflection from two displacement transducers on each side of the prism. These values were plotted in order to obtain the area under the load-displacement curve to determine fracture area. Due to the limit of the crack-opening extensometer used to control the load rate, the prisms did not fail completely. For this reason the final section of the curve was assumed to be an extension of the regression line from the last 1.0 mm of displacement extensometer data prior to reaching its limit. This was determined to be conservative due to the non-linear data that were observed at the end of the C1609 tests. The tails of the C1609 tests indicated that the prisms would continue to withstand load for a greater deflection than the assumed linear decrease. The plots utilized to calculate the area under the load versus deflection curve are shown in Figure 4-5, Figure 4-6, and Figure 4-7.

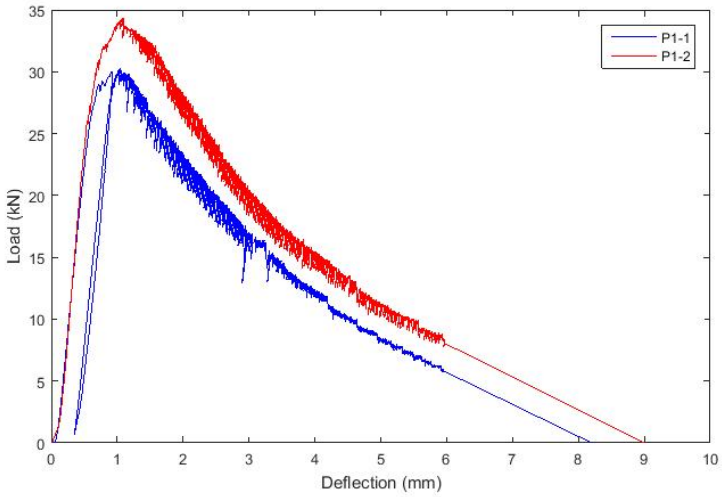

Figure 4-5. Load-deflection curve for notched prism test with single point load using UHPC from Specimen SB-3.

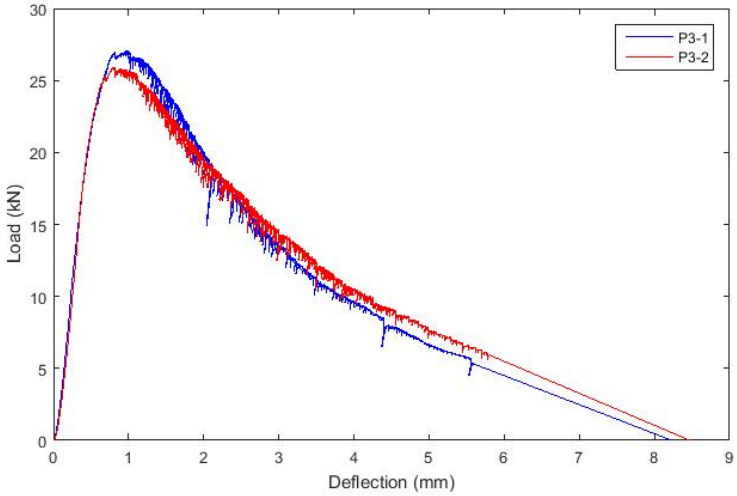

Figure 4-6. Load-deflection curve for notched prism test with single point load using UHPC from Specimen SB-1.

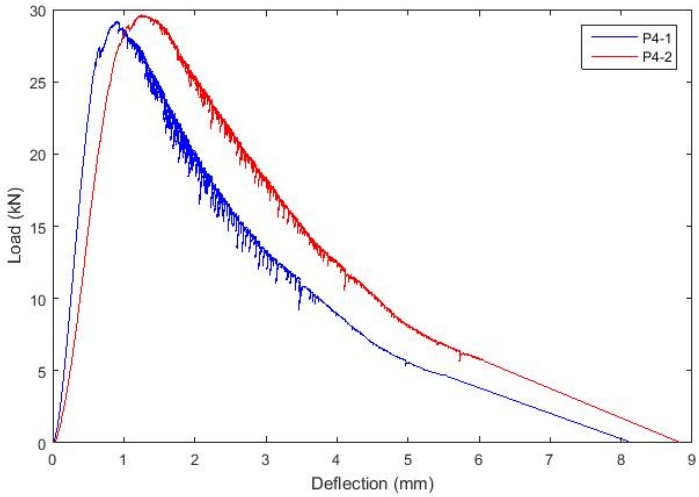

Figure 4-7. Load-deflection curve for notched prism test with single point load using UHPC from Specimen RB-1.

By utilizing trapezoids between data collection points, the areas under the curves were calculated. Additionally, the width and height of the cracked area were measured using a caliper and used to calculate fracture energy using Equation (15).

$$G_f = \frac{W_o}{A_{fracture}} \tag{15}$$

In this equation, G_f is the fracture energy (N/mm), W_o is the area under the load-deflection curve (N-mm), and $A_{fracture}$ is the area of the fracture plane (mm^2). Using this equation, it was found that the average fracture energy was 12802 N/mm. Table 4-4 summarises the values from the six notched prism tests.

Table 4-4. Summary of notched UHPC tests.

Specimen	Area Under Curve (N-mm)	Width (mm)	Height (mm)	Fracture Energy, W_o (N/mm)
P1-1 (SB-3)	101.2 x 10^6	74	102	13400
P1-2 (SB-3)	125.3 x 10^6	75.5	103.5	16000
P3-1 (SB-1)	89.3 x 10^6	75	105	11300
P3-2 (SB-1)	90.4 x 10^6	75	103	11700
P4-1 (RB-1)	85.2 x 10^6	75	102	11100
P4-2 (RB-1)	107.4 x 10^6	79	103	13200
			Average:	12800

The notch was able to control the crack location extending from the interior of the notch straight upwards to the load point. The prism did not break apart completely due to the steel fibres in the UHPC maintaining some continuity. Figure 4-8 shows one of the prisms following testing.

Figure 4-8. Failed notched prism test following loading.

4.2 Precast Slab Specimen Test - Sand-coated GFRP Specimens

As described previously, two precast concrete slab specimens were constructed using the sand-coated GFRP reinforcement. The first specimen was tested under fatigue loading at three locations, while the second specimen was only fatigued adjacent to the closure strip. Both specimens were tested to failure under static loading following the fatigue loading regimen.

4.2.1 Precast Slab Specimen with Sand-coated GFRP Fatigued at Three Locations (Specimen SB-3)

This precast slab specimen was fatigued to 2,000,000 cycles at three locations: the centre of one precast panel, adjacent to the closure strip and centred on the closure strip. The load locations were performed in that order. Following completion of fatigue loading, the slab was loaded to failure at two locations, first adjacent to the closure strip and second on the centre of the fatigued panel.

4.2.1.1 Fatigue Location 1 – Centre of Panel

The first fatigue loading location was in the centre of one of the precast concrete panels. Initially, the frequency of fatigue loading was set to 0.75 Hz as limited by the flow capacity of

the servo-valve in the testing frame. However, after approximately 50,000 cycles, the test was stopped and the servo-valve was replaced to allow for increased load frequency. From this point forward, all fatigue tests were performed at 2 Hz.

Deflections were recorded throughout the fatigue testing at both the valley (10 kN) and peak (110 kN) of the sinusoidal wave loading pattern. Figure 4-9 shows the deflection versus cycle curves for the valley and valley of the loading applied on the centre of the panel. Figure 4-10 shows the deflection range versus cycle for fatigue loading at the centre of panel. Note that gaps or breaks in the plotted data occurred due to displacement transducer errors that occurred during the test.

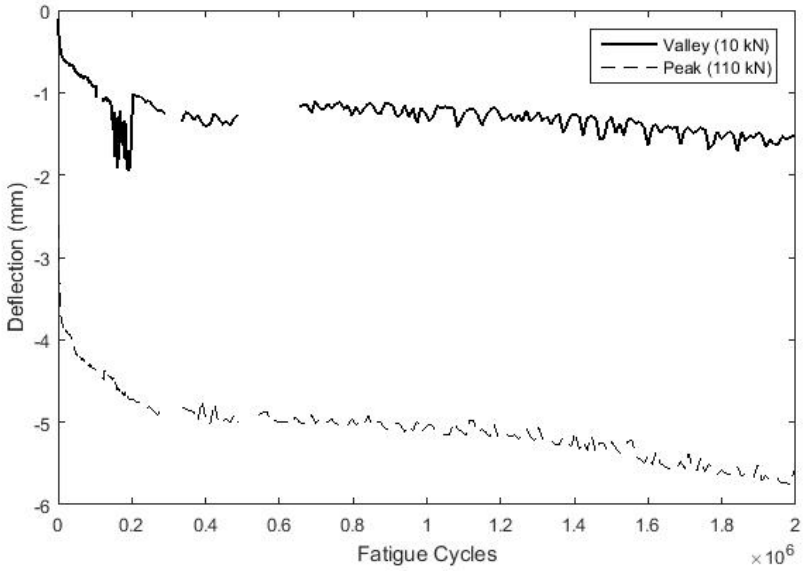

Figure 4-9. Specimen SB-3: Variation of peak and valley deflection response over time for centre of panel load location (deflection measured at load location).

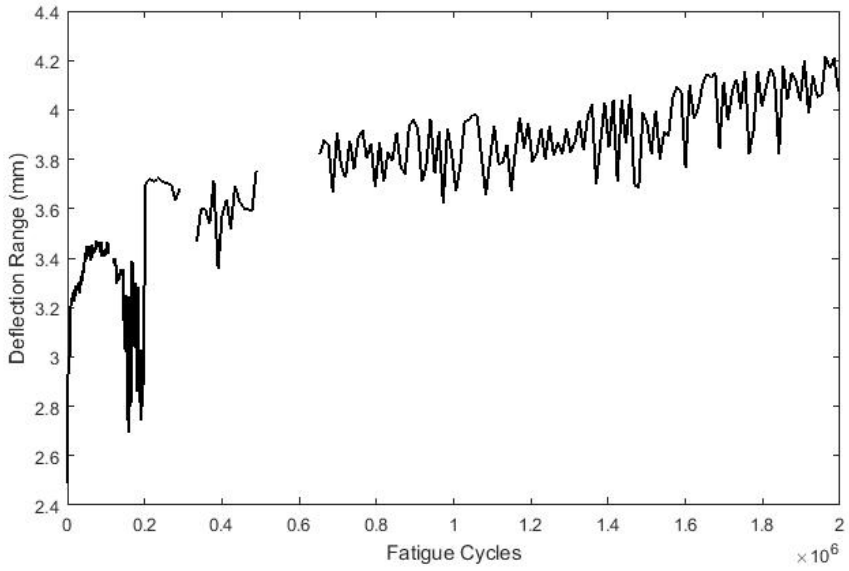

Figure 4-10. Specimen SB-3: Variation of deflection range (peak minus valley) over time for centre of panel load location.

As fatigue testing continued, the peak deflection increased approximately 49% between the cycle 1 and cycle 20,000 followed by an approximately linear increase in deflection for remainder of the test with a peak deflection increase of 46% between cycle 20,000 and the end of the fatigue test. During fatigue the range between the maximum deflection (peak) and the minimum deflection (valley) displayed a greater increase during the initial cracking phase when deflections were increasing quickly followed by an approximately linear increase for the remainder of the fatigue loading. The sawtooth patterns in the data are believed to be caused by background noise due to the voltage being slightly non-uniform. This is especially noticeable in the range plot due to the difference of two data sets which each have variance from background noise.

In order to evaluate the bar strain at various points during the fatigue loading, several plots depicting microstrain versus cycle count were created. Note that several sets of strain gauge data were unavailable either from the start of testing or became non-functional during fatigue loading due to gauge failures. The gauge names and locations are located in Chapter 3, Figure 3-19. Figure 4-11 shows the strain in the bottom longitudinal bars, Figure 4-12 shows the strain in the

top longitudinal bars, Figure 4-13 shows the strain in the transverse bars and Figure 4-14 shows the concrete strains.

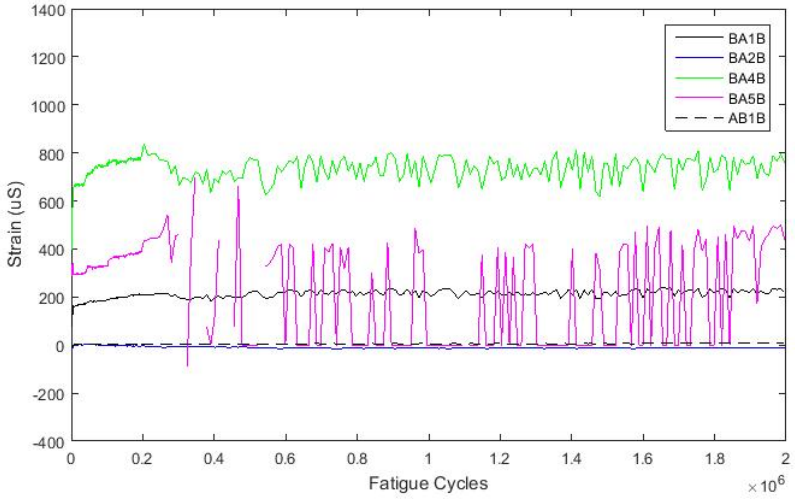

Figure 4-11. SB-3: Variation of strain range for bottom longitudinal bars with load on centre of panel.

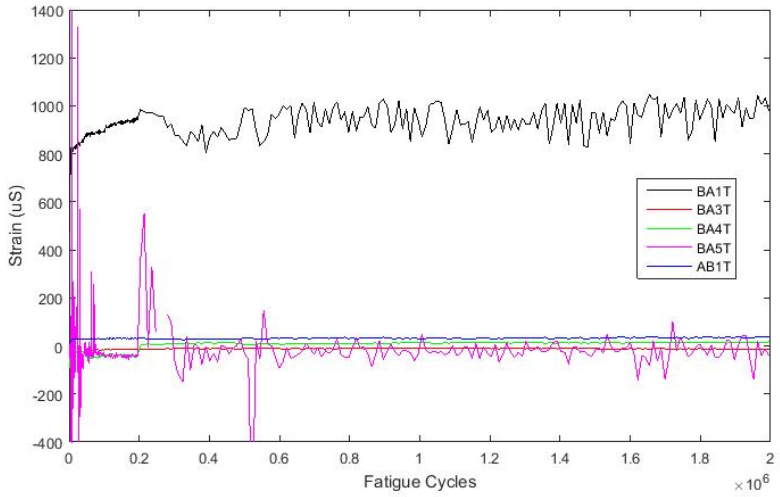

Figure 4-12. SB-3: Variation of strain range for top longitudinal bars with load on centre of panel.

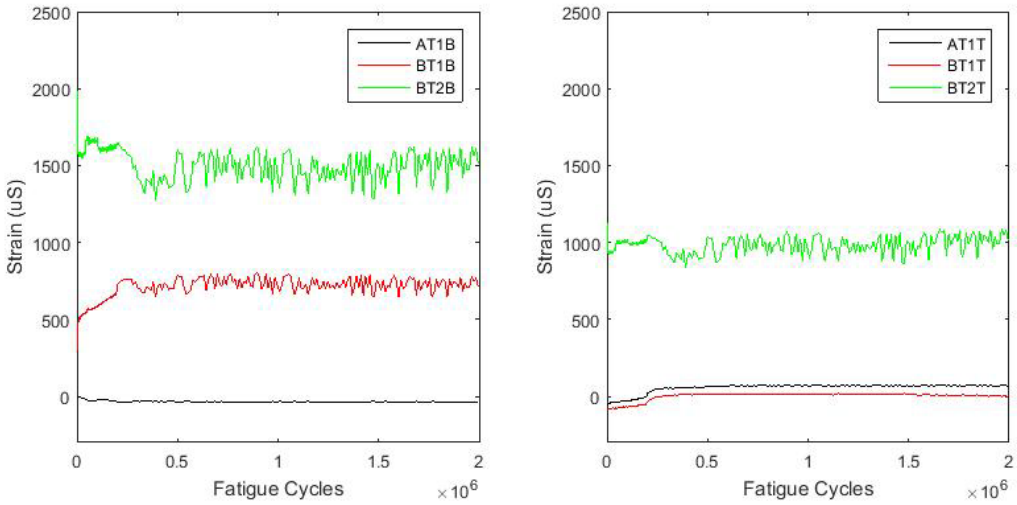

Figure 4-13. SB-3: Variation of strain range for transverse bars with load on centre of panel.

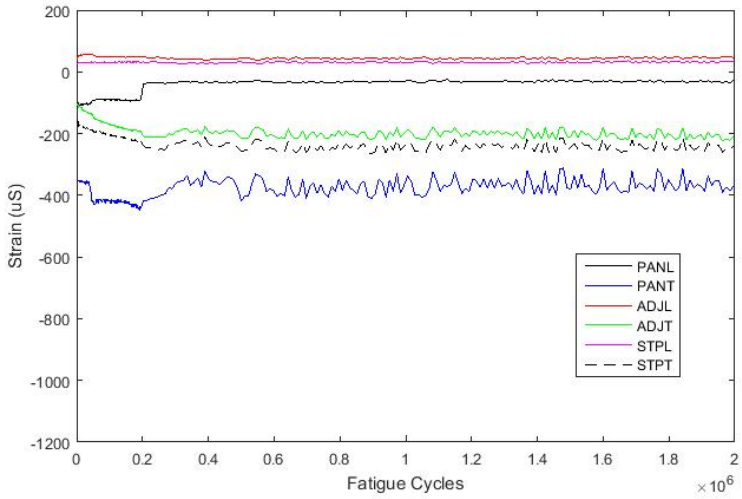

Figure 4-14. SB-3: Variation of strain range for top concrete fibre with load on centre of panel.

Based on these plots it is clear that the greatest strains were experienced in the bottom transverse reinforcement directly below the load point. Unfortunately, a significant number of gauges were not available during testing for a variety of reasons, leading to a lack of data at several points on the reinforcing bars.

4.2.1.2 Fatigue Location 2 – Adjacent to Closure Strip

Following loading on the centre of the precast panel, the specimen was loaded adjacent to the closure strip on the slab which was not loaded on the centre of the panel. Figure 4-15 and Figure 4-16 show the deflection and deflection range for this specimen during fatigue testing, respectively.

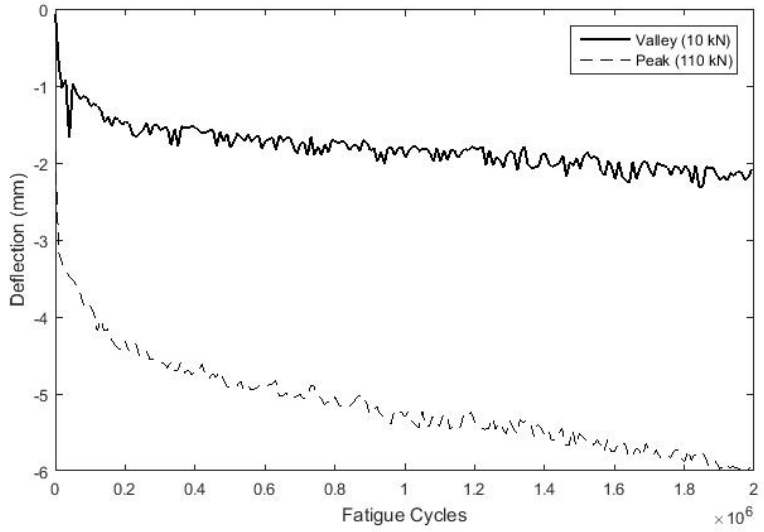

Figure 4-15. SB-3: Variation of peak and valley deflection response over time for adjacent to the closure strip load location (deflection measured at load location).

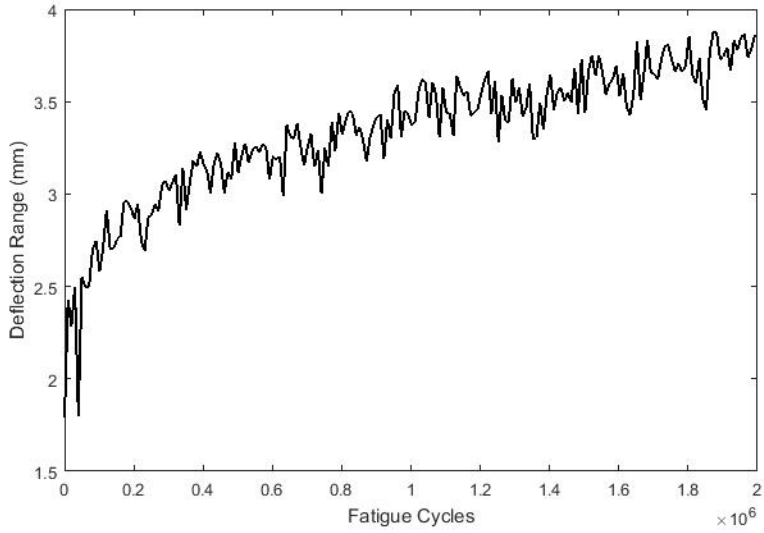

Figure 4-16. SB-3: Variation of deflection range (peak minus valley) over time for adjacent to the closure strip load location.

Similar to the behaviour observed for loading in the centre of one of the precast panels, deflections increased significantly, 71%, for the 20,000 cycles of loading adjacent to the closure strip. Again, this significant increase coincided with cracks forming and propagating throughout the specimen.. This was followed by an approximately linear increase in deflection for the remainder of the fatigue testing with an 88% increase in peak deflection from cycle 20,000 to the final cycle. Similarly, the deflection range increased approximately linearly during the fatigue testing.

Figure 4-17 shows the strain in the bottom longitudinal bars, Figure 4-18 shows the strain in the top longitudinal bars, Figure 4-19 shows the strain in the transverse bars and Figure 4-20 shows the concrete strains over the duration of the fatigue testing adjacent to the closure strip. The gauge names and locations are located in Chapter 3, Figure 3-19.

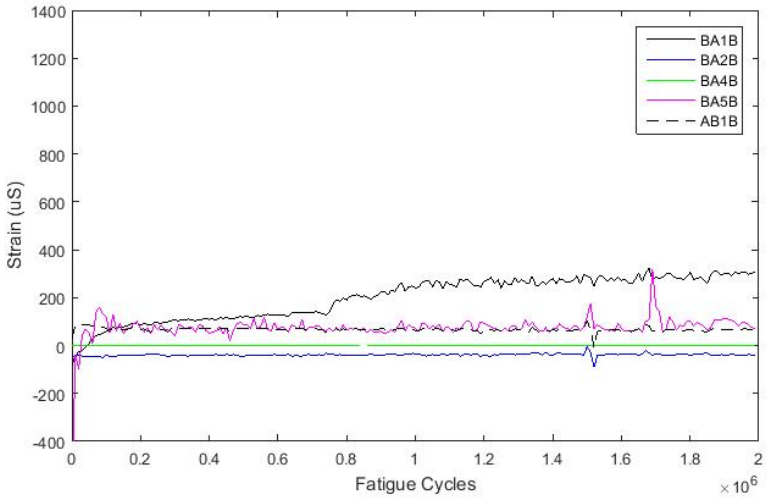

Figure 4-17. SB-3: Variation of strain range for bottom longitudinal bars with load adjacent to closure strip.

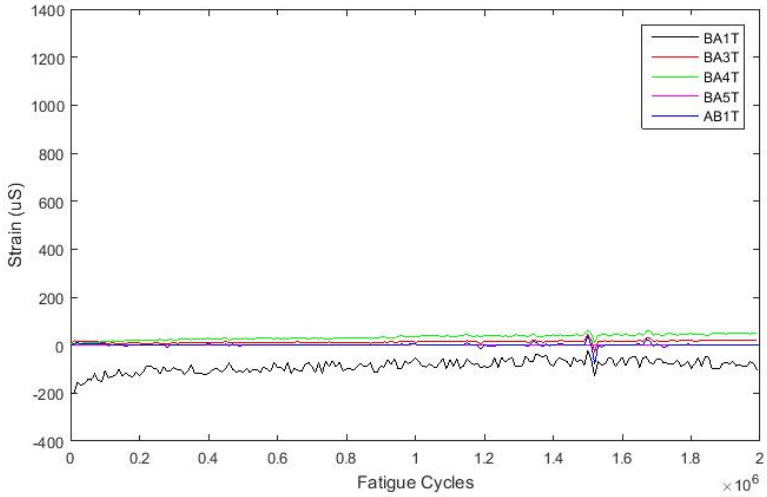

Figure 4-18. SB-3: Variation of strain range for top longitudinal bars with load adjacent to closure strip.

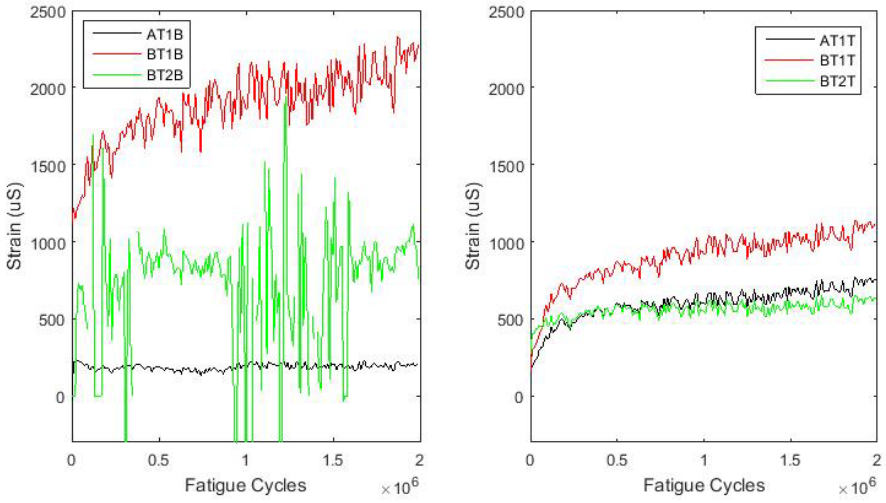

Figure 4-19. SB-3: Variation of strain range for transverse bars with load adjacent to closure strip.

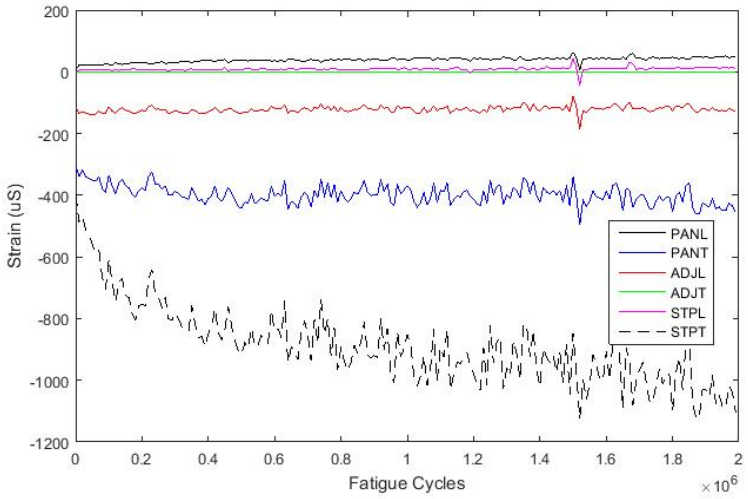

Figure 4-20. SB-3: Variation of strain range for top fibre of concrete with load adjacent to closure strip.

Based on these plots it is clear that the greatest strains were experienced in the bottom transverse reinforcement. Unfortunately, the gauge on the bottom transverse bar directly below the load point was not available. The largest measured strains were experienced in the bottom transverse bar in the non-loaded slab adjacent to the closure strip. Unfortunately, a significant number of gauges were not available during testing for a variety of reasons, leading to a lack of data at several points on the reinforcing bars.

4.2.1.3 Fatigue Location 3 – Centre of Closure Strip

Following fatigue loads applied on the centre of the panel and adjacent to the closure strip, the specimen was fatigued on the closure strip. Figure 4-21 and Figure 4-22 show the deflection and deflection range for this specimen during fatigue testing, respectively.

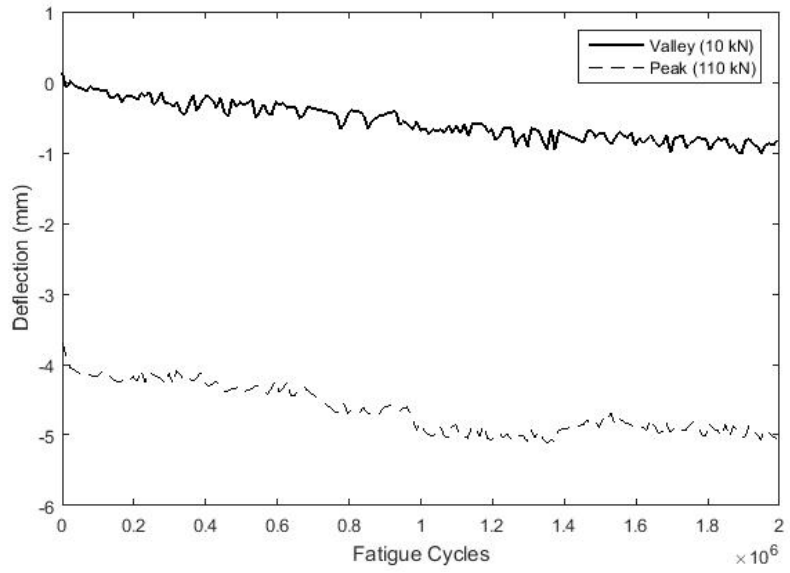

Figure 4-21. SB-3: Variation of peak and valley deflection response over time for centre of closure strip load location (deflection measured at load location).centre

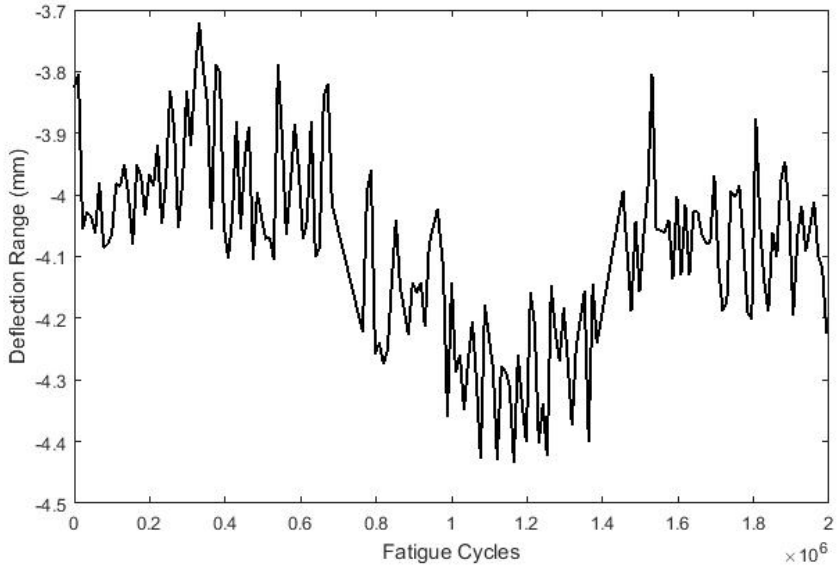

Figure 4-22. SB-3: Variation of deflection range (peak minus valley) over time for centre of closure strip load location.

Unlike the fatigue loading at the previous two locations, the deflection increased approximately linearly for the entire 2,000,000 cycles when loading on the closure strip. This is primarily due to the pre-existing cracks caused by fatigue loading at the other locations. For this reason, there was no initial crack propagation, resulting in much larger deflections from the start of fatigue

loading. The deflection increase was approximately linear throughout fatigue cycles with a peak deflection increase of approximately 25% over 2,000,000 fatigue cycles. The deflection range was relatively stable throughout the fatigue testing.

Figure 4-23 shows the strain in the bottom longitudinal bars, Figure 4-24 shows the strain in the top longitudinal bars, Figure 4-25 shows the strain in the transverse bars and Figure 4-26 shows the concrete strains. The gauge names and locations are located in Chapter 3, Figure 3-19.

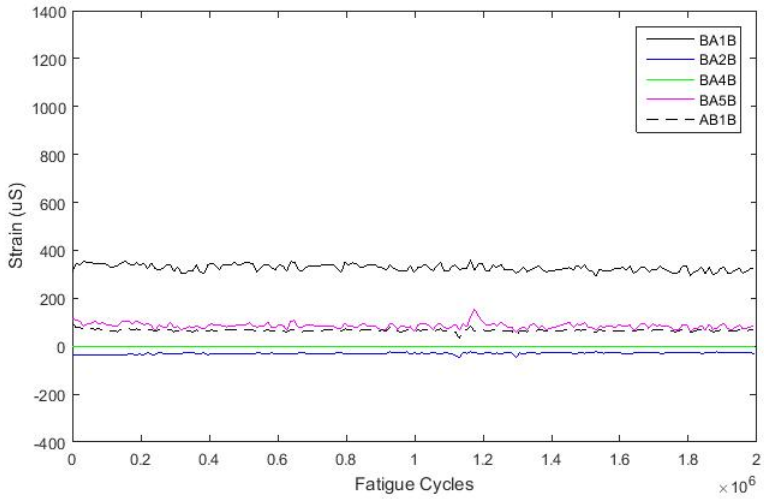

Figure 4-23. SB-3: Variation of strain range for bottom longitudinal bars with load on the centre of the closure strip.

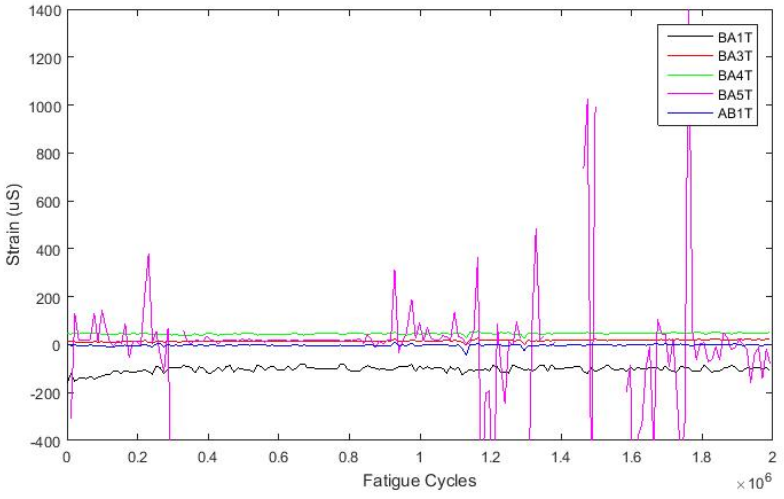

Figure 4-24. SB-3: Variation of strain range for top longitudinal bars with load on the centre of the closure strip.

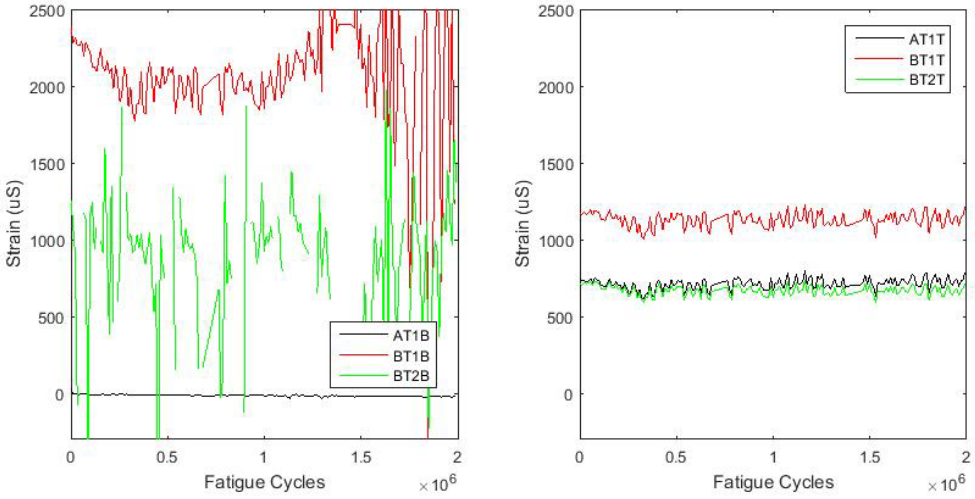

Figure 4-25. SB-3: Variation of strain range for transverse bars with load on the centre of the closure strip.

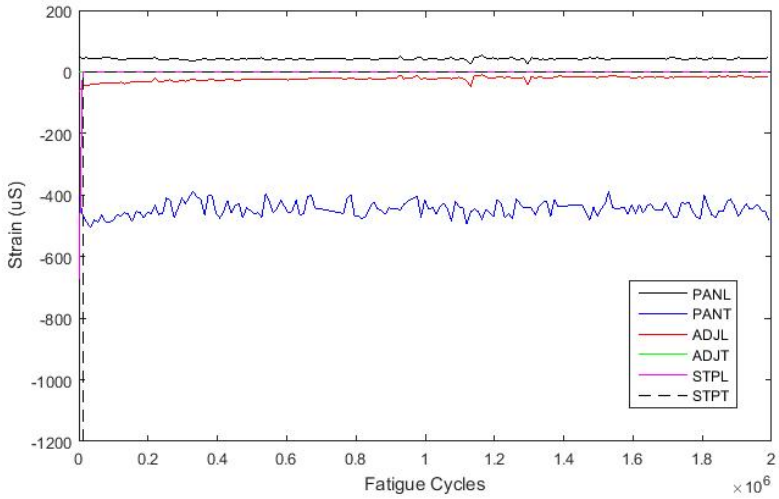

Figure 4-26. SB-3: Variation of strain range for top fibre of concrete with load on the centre of the closure strip.

Based on these plots it is clear that the greatest strains were experienced in the bottom transverse reinforcement adjacent to the closure strip near the load point. Unfortunately, a significant number of gauges were not available during testing for a variety of reasons, leading to a lack of data at several points on the reinforcing bars.

4.2.1.4 Comparison of Fatigue Behaviour for the Three Load Locations

In order to compare the response of the slab to fatigue loading at the three locations, the deflection response (peak and valley) for loading at each location is plotted in Figure 4-27. In this figure, the deflection at the start of each location was reset to zero for comparison purposes. That is, the permanent deflections caused by fatigue loading at previous load locations are not included in the deflection data in this plot.

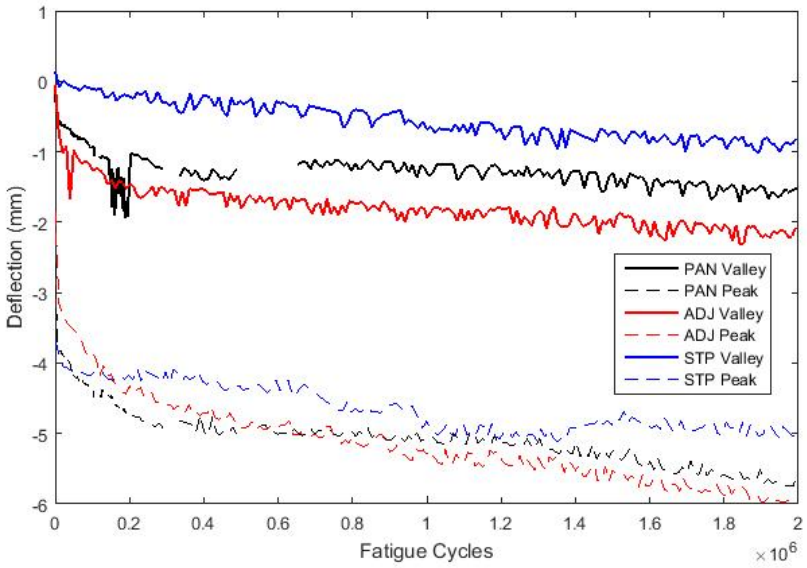

Figure 4-27. SB-3: Variation of peak and valley deflection response over time for various fatigue load location (deflection measured at load location).

It is clear that the largest deflection increase is when the load was adjacent to the closure strip (second load location) and that the loading at the centre of the closure strip (third load location) produced the smallest deflection increase. This is likely due to the pre-existing cracks at the time of fatiguing on the closure strip. Additionally, the deflection at this location behaves in two-way action compared to the centre of the panel, which is relatively close to a free edge resulting in behaviour that is partially one-way bending causing additional deflection.

Similarly, the deflection range for each loading location was plotted in Figure 4-28. This figure shows that loading on the closure strip had the least increase in deflection range compared to the other locations with an overall range change of only 0.2 mm compared to a 1.6 mm increase in deflection range when loaded on the centre of the panel and 1.25 mm increase in range when

loading adjacent to the panel. The reason for these differences is likely due to the existing cracks at the time of loading on the closure strip. The other two load locations had significant changes in deflection range due to the initial crack propagation which was not experienced during the fatigue loading on the closure strip.

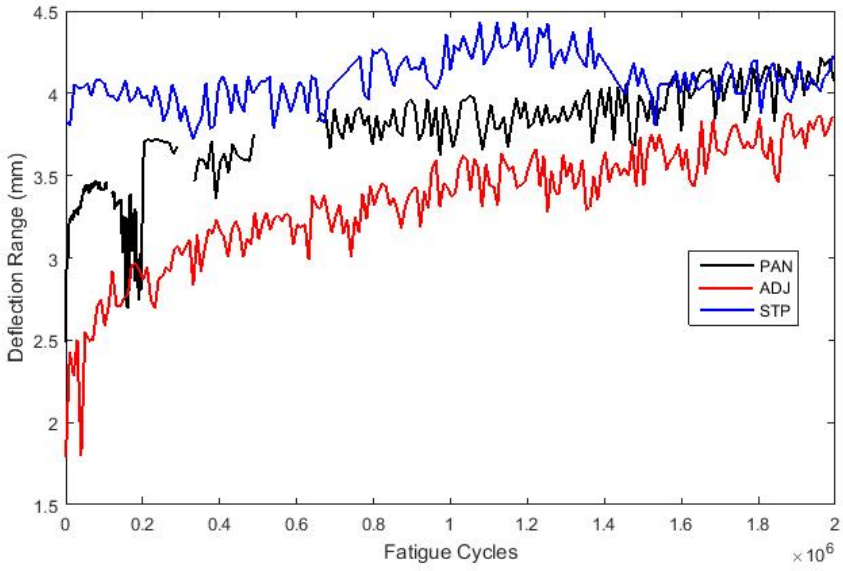

Figure 4-28. SB-3: Variation of deflection range (peak minus valley) over time for various fatigue load locations.

4.2.1.5 Failure Loads Under Static Loading

Following fatigue loading at the three locations, the slab was loaded to failure under static loading adjacent to the closure strip and in the centre of the precast panel. Loading was applied in displacement control at a rate of 2 mm/min. The first location to be loaded to failure was adjacent to the closure strip. The slab experienced a punching shear failure mode at this location, however the typical or expected failure cone was truncated by the UHPC closure strip. Figure 4-29 shows the condition of the underside of the slab after failure and indicates the load location as well as the extents of the punching cone.

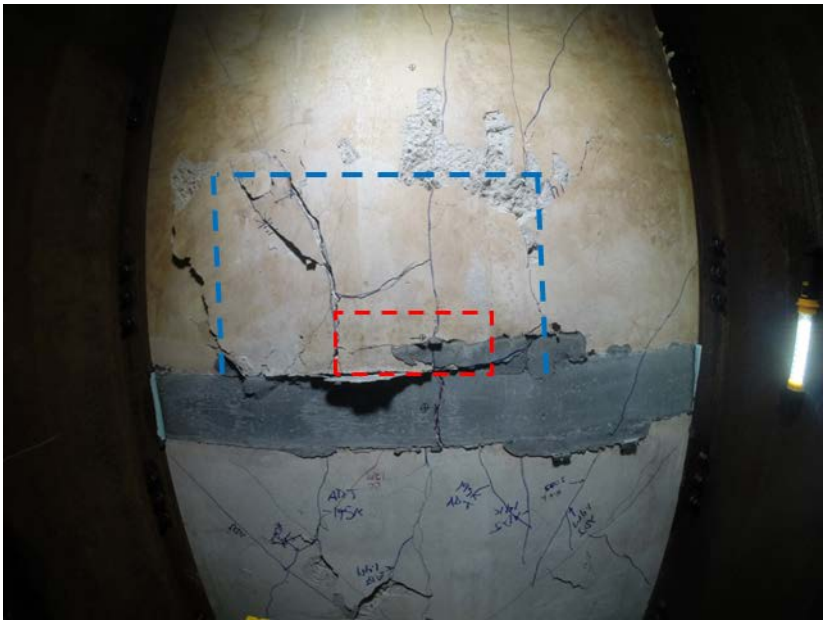

Figure 4-29. SB-3: Underside of slab after punching failure adjacent to the closure strip. (Red line is load location, blue line is punch cone edge)

During loading at this location, the deflection interlock limits set on the controller for safety purposes were triggered several times resulting in the loss of load. The punching failure occurred at a load of approximately 285 kN. Figure 4-30 shows the load versus displacement plot of loading to failure at this location.

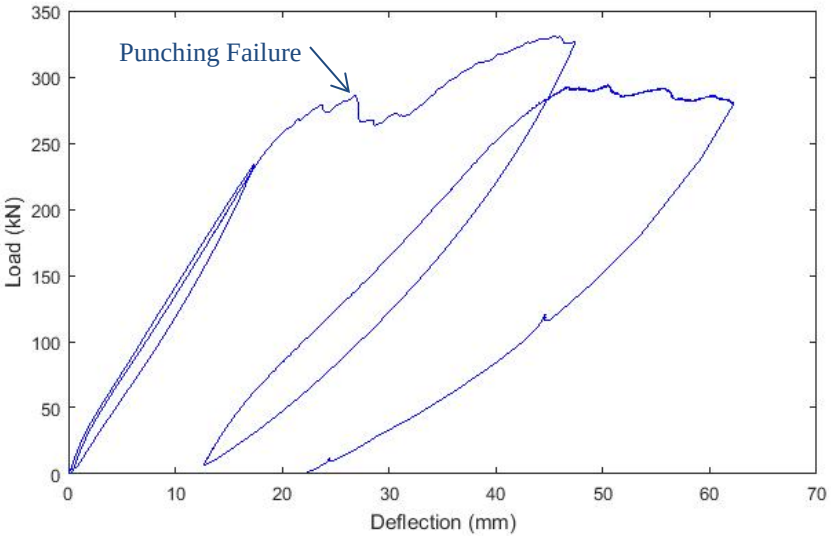

Figure 4-30. SB-3: Load-displacement response for the failure loading adjacent to the closure strip.

Following initial failure, loading was continued and the load-resisting capacity of the slab increased, likely caused by the development of arch action with the primary compression node being the steel load block.

Following the static punching shear failure adjacent to the closure strip, the slab specimen was moved in the testing frame and loaded to static failure in the centre of the panel (first fatigue loading location). Similar to the failure adjacent to the closure strip, the panel failed in punching shear. However, the loaded area of the slab was already significantly damaged due to previous fatigue loading and the preceding static punching failure test adjacent to the closure strip. Large cracks (greater than 5 mm width) were observed on the panel loaded on the centre following punching failure adjacent to the closure strip. This existing damage may have affected the slab response for static testing at this location. Figure 4-31 shows the underside of the slab at the centre of the loaded panel with the load location shown. The punching cone is not shown since it was not a well-defined area due to excessive cracking and concrete spalling.

Figure 4-31. SB-3: Underside of slab following failure in centre of precast concrete panel. (Red line indicates load location)

The static punching shear failure at this load location occurred at approximately 205 kN, which is significantly less than the punching shear failure load adjacent to the closure strip. The reduced failure load was likely due to damage from previous loading and the undefined punch cone. The severity of the existing damage is also evident in that the punching load was less than adjacent to the closure strip despite the failure occurring on four sides of the load, compared to the truncated punch experienced adjacent to the closure strip. Figure 4-32 shows the load versus defection plot for the static loading test to failure at the centre of the panel.

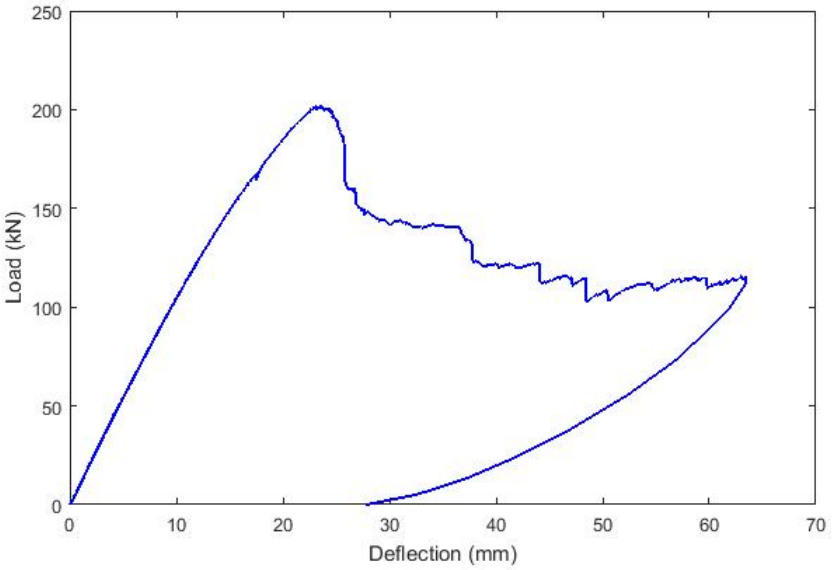

Figure 4-32. SB-3: Load-displacement response for failure loading on centre of precast concrete panel.

4.2.2 Precast Slab Specimen with Sand-coated GFRP Fatigued at One Location (Specimen SB-1)

The second precast slab specimen with sand-coated GFRP bars was only subjected to fatigue loading adjacent to the closure strip. The reason for only loading at this location was that this was determined to be the critical load location. Therefore, only this location was fatigued to eliminate any influence of loading at other locations might have on the fatigue behaviour or the failure mode of the specimen. Prior to fatigue loading, the specimen was loaded statically up to the service load of 110 kN at the three load locations in order to establish initial stiffness and deflections of the slab at the load locations. These results will be used to compare the analysis

performed in ABAQUS for service loads to the experimental response. Each location was loaded twice: the first cycle was to form any initial cracks that may occur and to "settle" the specimen in the test frame, and then a second time to obtain a representative load-deflection response (without crack formation).

4.2.2.1 Initial Static Tests to Characterize Slab Behaviour

The first location loaded statically was adjacent to the closure strip. Figure 4-33 shows the load deflection curve for the first two curves. Note that the displacement measurements were zeroed after the first cycle for plotting purposes. It is clear that the first test resulted more plastic deformation than the second load, however no cracks were noted during either of these load cycles. It is possible that some settlement occurred at the supports which contributed to the permanent deformation shown.

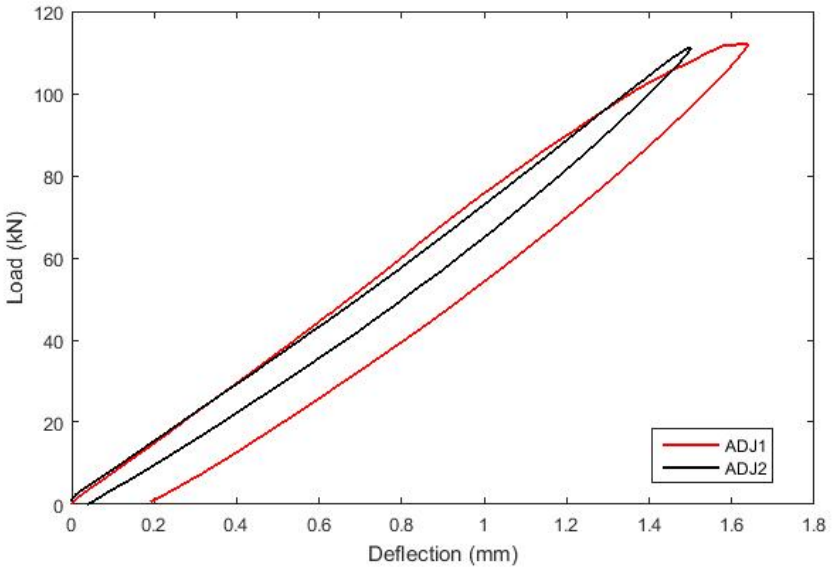

Figure 4-33. SB-1: Load-deflection responses for first two static tests at service loads adjacent to closure strip.

The second location to undergo static tests was the centre of the closure strip. Similar to the previous load location, no cracks were noted following either load cycle. The load-deflection behaviour at this load location was essentially linear up to approximately 100 kN during both cycles, although the first cycle showed a non-linear component at around 20 kN of load. This irregularity is likely due to support settlement or loading on a surface with a poor finish that

caused a slight rough patch to be crushed. Figure 4-34 shows the load deflection curves for these two static tests. Note that the displacement measurements were zeroed after the first cycle for plotting purposes.

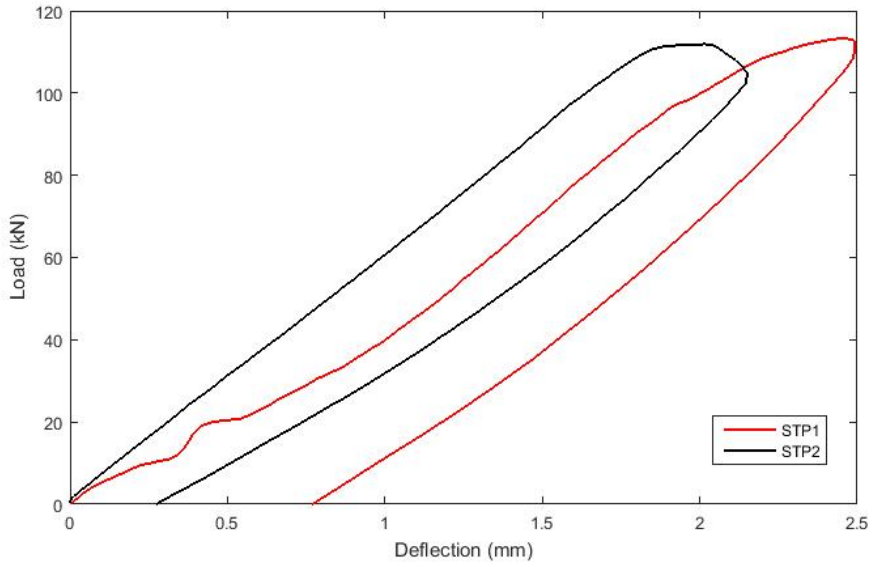

Figure 4-34. SB-1: Load-deflection responses for first two static tests at service loads centred on the closure strip.

The final location to undergo static tests was the centre of one of the precast concrete panels. Unlike the previous static tests, loading at this location resulted in significant crack formation on the underside of the loaded panel. The first static load cycle showed an approximately bi-linear load-deflection response with a significant change in stiffness occurring due to cracking at a load of approximately 90 kN. The initial or uncracked stiffness from the first load cycle was notably greater than the stiffness observed during the second load cycle at this location. The first test had significant plastic deflections due to crack formation. Consequently, the second test was then less stiff initially, but resulted in very little plastic or permanent deformation. Figure 4-35 shows the load deflection curves for these two static tests. Note that the displacement measurements were zeroed after the first cycle for plotting purposes. Figure 4-36 shows a photo of the underside of the loaded slab panel, with the cracks from prior static loading shown.

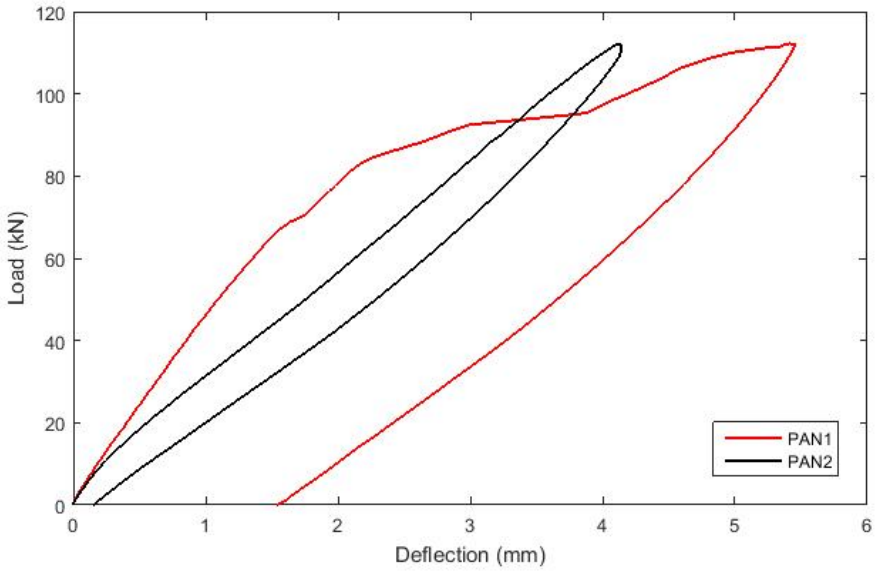

Figure 4-35. SB-1: Load-deflection responses for first two static tests at service loads on centre of panel.

Figure 4-36. SB-1: Crack pattern on precast panel after initial static loads.

Comparing the static tests at the three locations, it was clear that the slab response for the load location at the centre of the precast panel had significantly less stiffness compared to the response for loading adjacent to the closure strip or loading directly on the closure strip. The

primary reason for this difference in stiffness is due to the relatively close free edge when loading on the centre of the panel. The other two locations would act as two-way slabs, whereas the load on the centre of the panel is a combination of one-way and two-way bending. Figure 4-37 and Figure 4-38 show a comparison of the first and second static cycles for the three load locations. These plots show the curves for loading adjacent to the panel (ADJ), on the centre of the panel (PAN), and on the closure strip (STP).

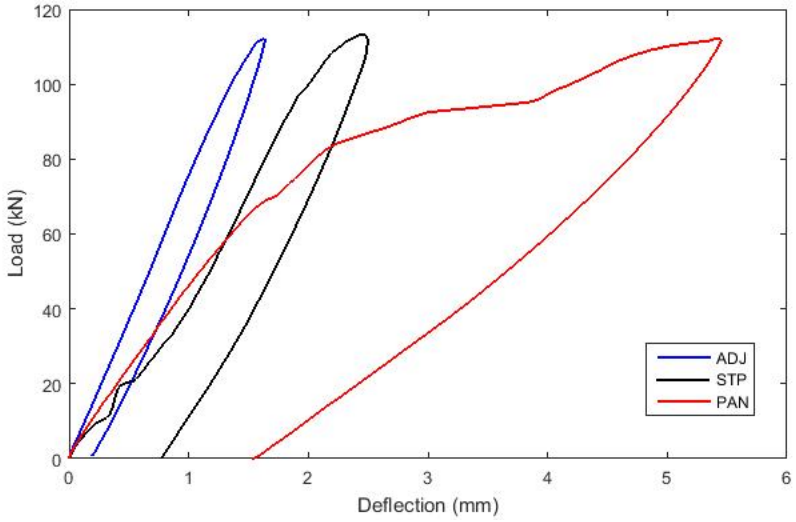

Figure 4-37. SB-1: Comparison of static load-deflection response at three locations for the initial cycle.

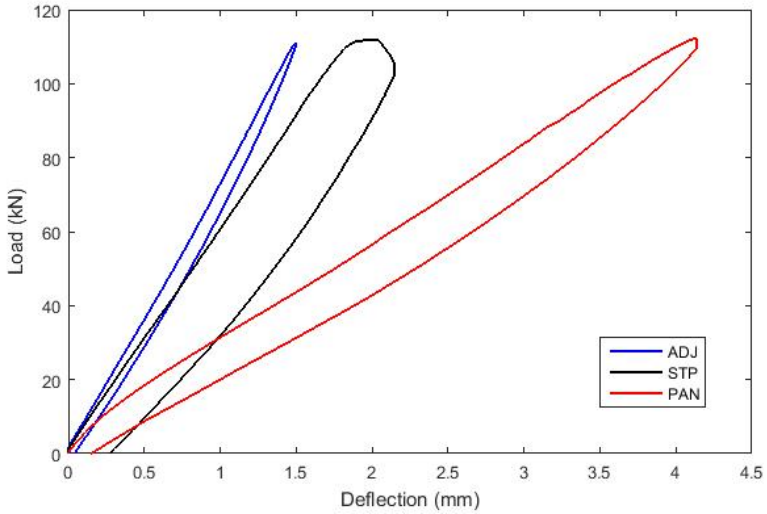

Figure 4-38. Comparison of static load-deflection responses at three locations for the second load cycle.

4.2.2.2 Fatigue Loading Adjacent to Closure Strip

As mentioned previously, this precast slab specimen was only subjected to fatigue loading adjacent to the closure strip, as this was deemed to be the critical loading location for this slab system. Figure 4-39 shows the deflection versus cycle curves for the peak and valley of the loading applied on the centre of the panel. Figure 4-40 shows the deflection range versus cycle for fatigue loading adjacent to the closure strip.

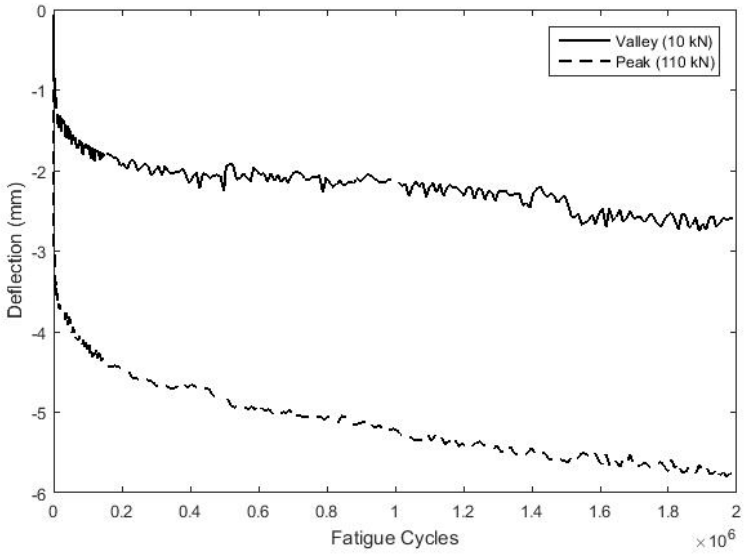

Figure 4-39. SB-1: Variation of peak and valley deflection response over time for adjacent to the closure strip load location (deflection measured at load location).

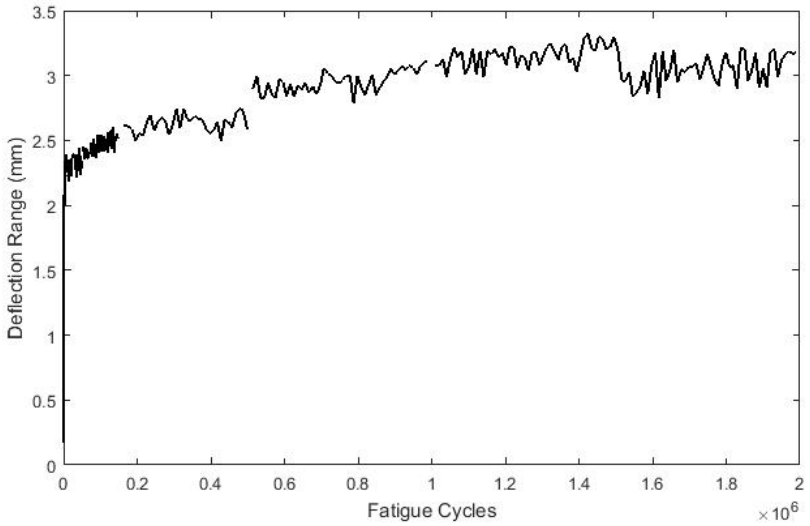

Figure 4-40. SB-1: Variation of deflection range (peak minus valley) over time for adjacent to the closure strip load location.

During fatigue testing, the deflection increased 63% between the initial cycle and cycle 20,000 followed by an approximately linear increase in deflection of 57% from cycle 20,000 to the end of the test. The deflection range displayed a greater increase during the initial cracking phase when deflections were increasing quickly followed by an approximately linear increase for the remainder of the fatigue loading.

In order to more completely understand the overall deflection behaviour of the slab, the deflection profile measured at four locations along the centreline of the slab is plotted in Figure 4-41.

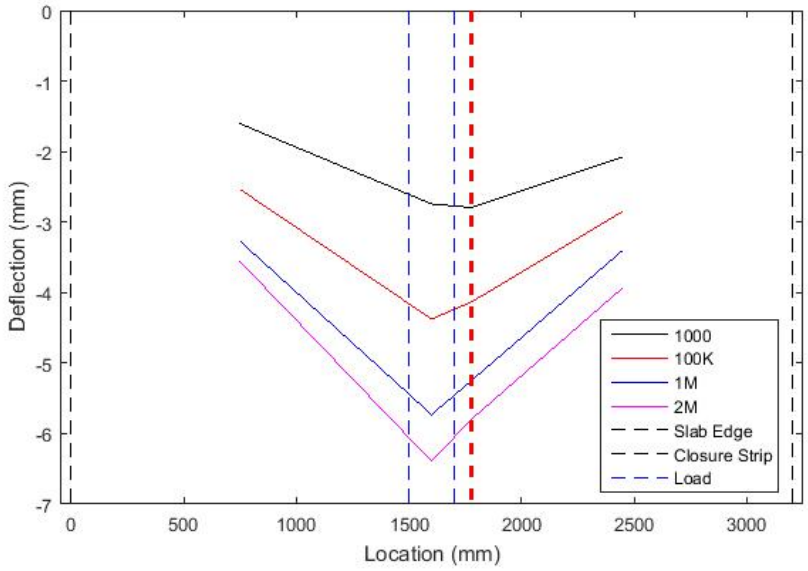

Figure 4-41. SB-1: Slab deflection profile at peak load over various fatigue cycles.

Another point of interest is that the maximum deflection in the profile was initially centred under the loaded area adjacent to the closure strip. However, after the initial 1000 cycles, the location of the maximum deflection in the profile shifted to the centre of the closure strip rather than directly below the loaded area. This shift in the deflection profile may have occurred due to the formation and propagation of a crack extending across the width of the closure strip that eventually widened enough to break the steel fibres across the crack. Once the steel fibres were broken, the stiffness of the strip was reduced, causing the deflection at this location to increase due to a lack of reinforcing bars perpendicular to the crack (within the closure strip). Figure 4-42 shows a picture of the crack after fatigue loading with a width of approximately 1.5 mm.

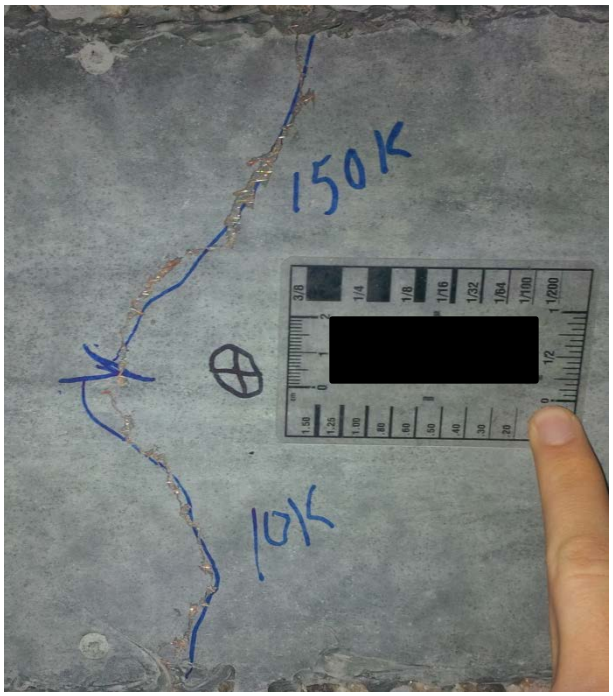

Figure 4-42. SB-1: Crack through UHPC at midspan.

In addition to the load-deflection response measured continuously during fatigue testing, the fatigue loading was stopped at regular intervals to allow static load cycles to understand how the stiffness of the slab was changing throughout the test. Figure 4-43 shows a plot of the static load versus deflection response measured at various intervals over the duration of the fatigue loading. The deflection data for each static test were zeroed for the purposes of comparing the change in stiffness throughout the fatigue loading. It can clearly be seen that there is significant stiffness change during the static load cycles at low cycle counts, with the stiffness changing more gradually between static load cycles recorded at higher cycle counts.

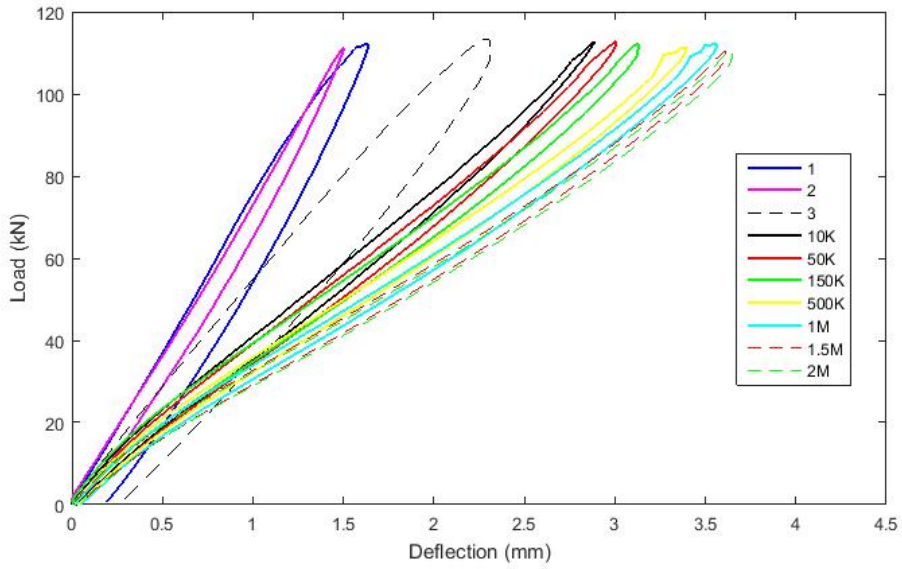

Figure 4-43. SB-1: Load-deflection responses at various cycles with initial deflection for each cycle set to zero.

In order to show how the absolute (not zeroed) static load-deflection response changed over the course of the fatigue loading, Figure 4-44 shows a similar plot with each static load cycle starting at the permanent deflection recorded at the start of the static load cycle.

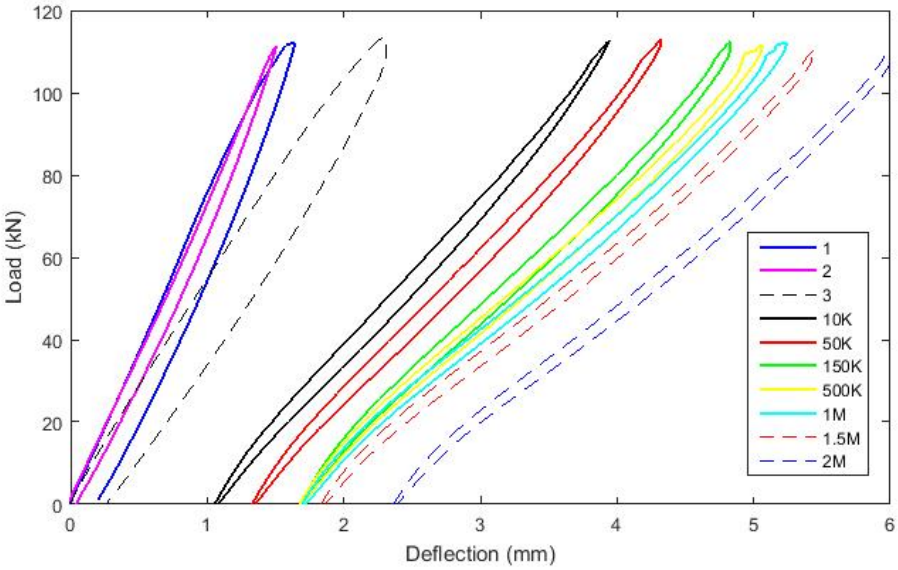

Figure 4-44. SB-1: Load-deflection responses at various load cycles with the initial deflection adjusted for plastic deformation during fatigue.

This behaviour clearly shows that the permanent deflection is greater during the initial load cycles when the slab is relatively stiff and that at higher cycle counts, when the stiffness is reduced, the permanent deflection is similarly reduced. The reason for this behaviour is due to the crack propagation noted during fatigue. During the initial cycles, as the cracks propagate, the specimen will undergo more permanent deflection due to the increased cracking. However, at higher cycle counts when there is limited crack propagation, the permanent deflection increase is less severe.

In order to evaluate the bar strain at various points during the fatigue loading, several plots depicting microstrain versus cycle count were created. Several sets of strain gauge data were unavailable either from the start of testing or became non-functional during fatigue loading. Figure 4-45 shows the strain in the bottom longitudinal bars, Figure 4-46 shows the strain in the top longitudinal bars, Figure 4-47 shows the strain in the transverse bars and Figure 4-48 shows the concrete strains. The gauge names and locations are located in Chapter 3, Figure 3-19.

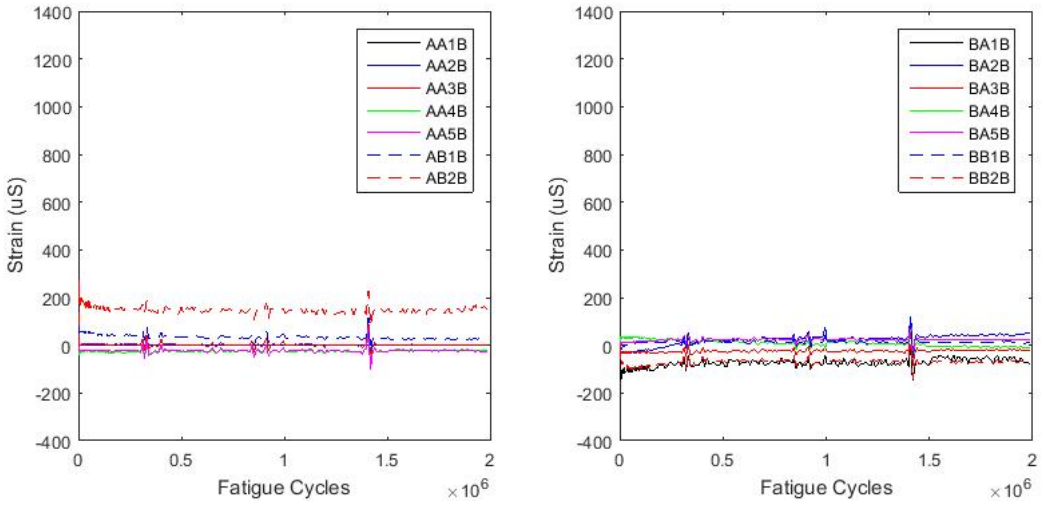

Figure 4-45. SB-1: Strain range for bottom longitudinal bars with load adjacent to the closure strip.

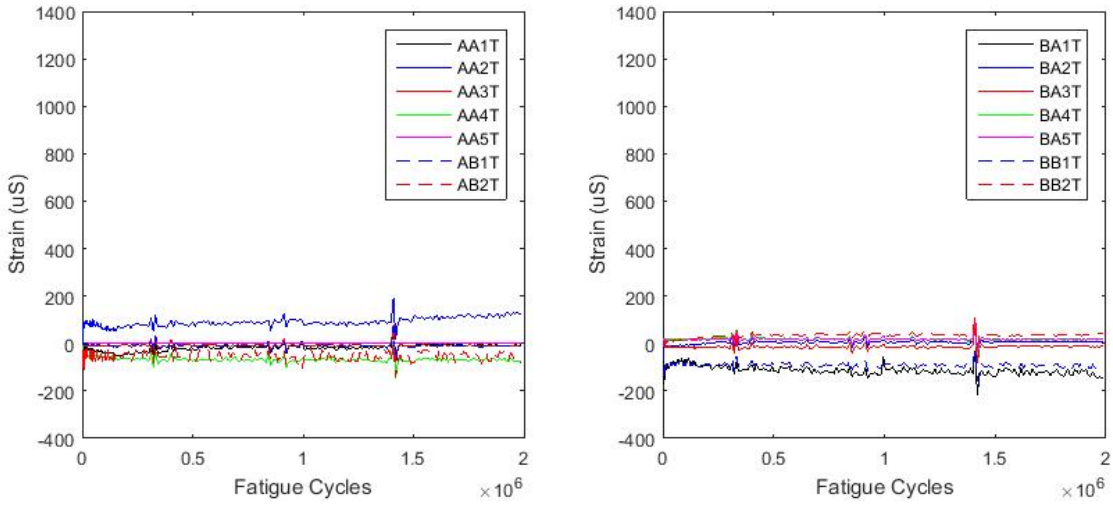

Figure 4-46. SB-1: Strain range for top longitudinal bars with load adjacent to the closure strip.

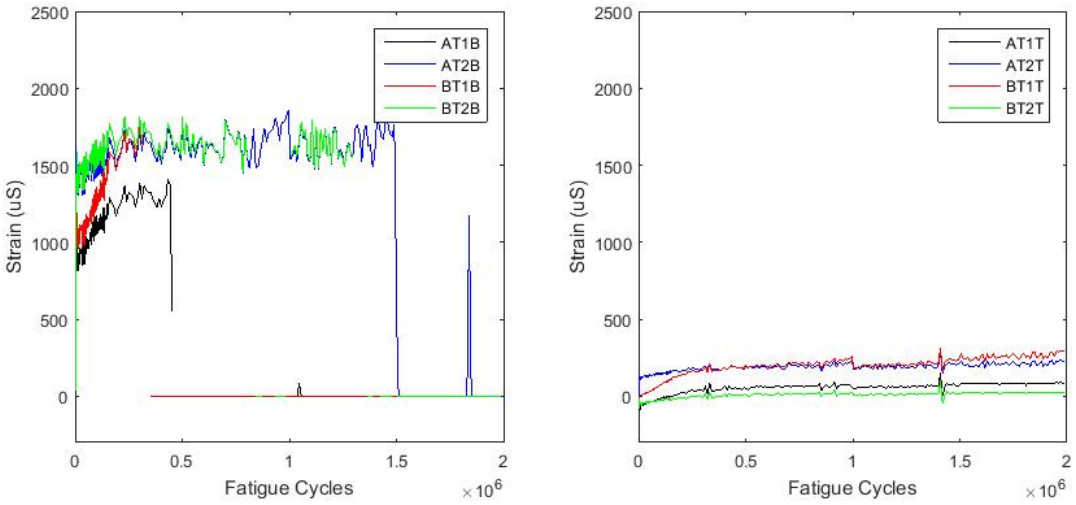

Figure 4-47. SB-1: Strain range for transverse bars with load adjacent to the closure strip.

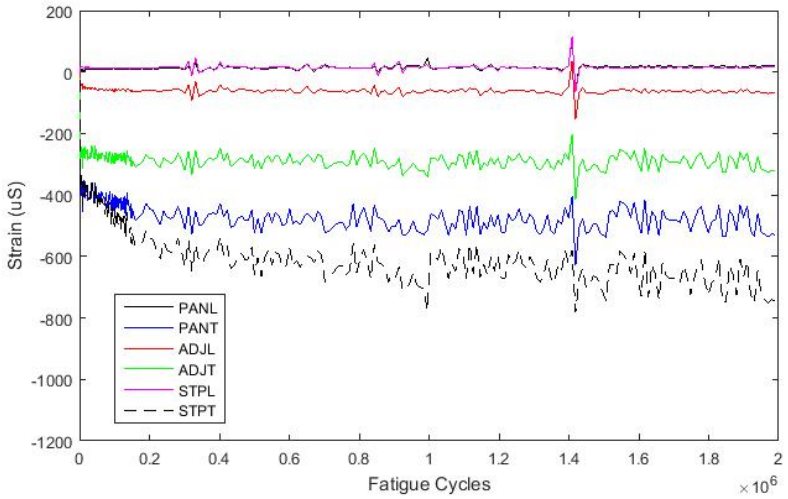

Figure 4-48. SB-1: Strain range for top fibre of concrete with load adjacent to the closure strip.

The measured strain data suggest that the largest strains were experienced in the bottom transverse reinforcement. The other interesting note was sudden, significant change in all measured strains at approximately 1.4 million cycles. This strain change may have been caused by a sudden change in ambient temperature that altered the measured strain values, since there were no other indications that these differential strains resulted from actual behaviour.

Following completion of the fatigue loading, photos of the underside of the slab were taken to capture the overall crack pattern created during fatigue. Figure 4-49 shows these photos of the underside of slab at three locations: centred under the panel that was loaded adjacent to the strip, at the centre of the strip and centred under the panel that was loaded statically initially, but never directly fatigued.

Figure 4-49. SB-1: Underside of slab after fatigue loading. (Top left: slab loaded adjacent to panel, Top Right: closure strip, Bottom: panel loaded in centre)

4.2.2.3 Failure Loads Under Static Loading

Following fatigue load at the three locations the slab was loaded to failure adjacent to the closure strip and in the centre of the precast panel. Loading was applied in displacement control at a rate of 2 mm/min. The first location to be loaded to failure was adjacent to the closure strip. Similar to specimen SB-3, specimen SB-1 experienced a punching shear failure mode with the failure cone truncated by the UHPC closure strip. Figure 4-50 shows the underside of the slab after failure and indicates the load location as well as the extents of the punching cone.

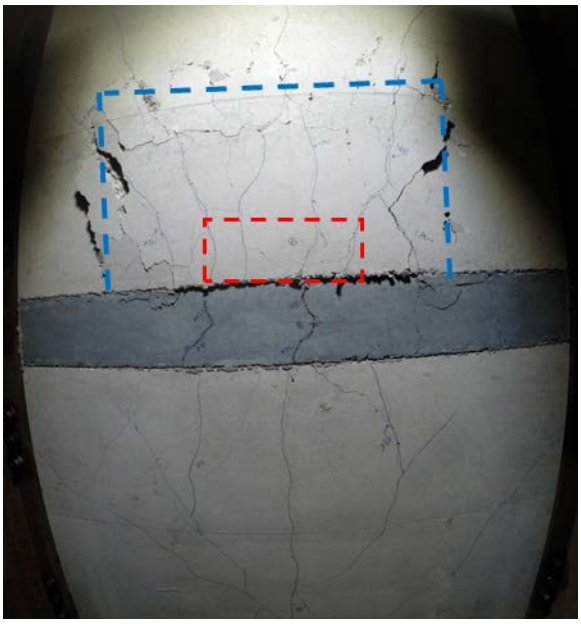

Figure 4-50. SB-1: Underside of slab following failure loading adjacent to closure strip. (Red indicates load location and blue is exterior edge of punch cone)

Figure 4-51 shows the load versus displacement plot up to failure at this location. The punching failure occurred at a load of approximately 345 kN. The initial load-deflection response was approximately linear until approximately 150 kN. Several sudden decreases in load occurred prior to punching failure when significant cracks formed at the corner shear pockets.

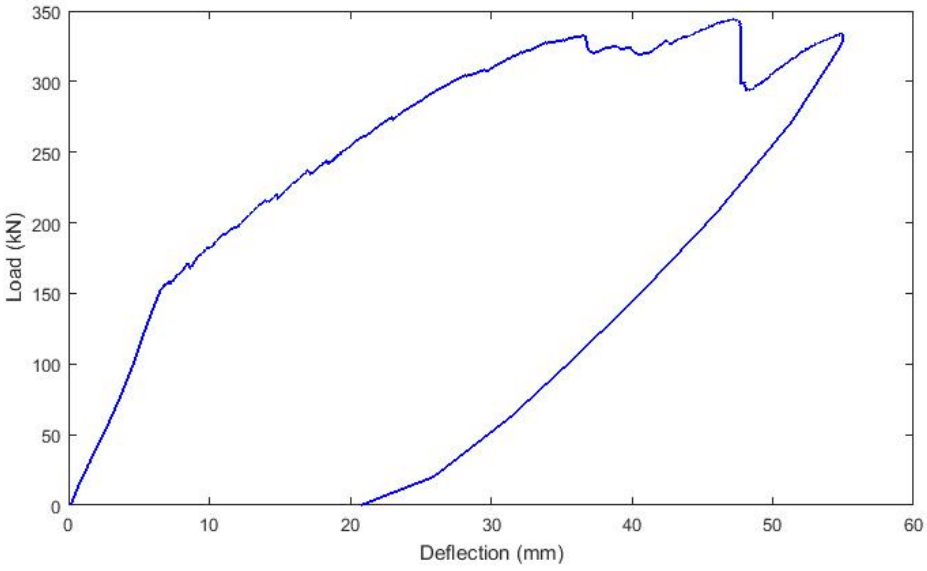

Figure 4-51. SB-1: Load-displacement curve for failure adjacent to closure strip.

Figure 4-52 shows a sample of cracking at the edge shear pockets. Similar to the behaviour observed for specimen SB-3, the slab continued to carry increasing load after occurrence of the punching failure due to the existence of arch action with the primary compression node being the steel load block.

Figure 4-52. SB-1: Corner cracking occurred during failure loading adjacent to closure strip.

The slab was also loaded to failure at the centre of panel to compare the ultimate load an unfatigued uniform concrete panel could sustain. However, there was significant existing damage caused by the punching failure adjacent to the closure strip. This resulted in a decreased failure load of 245 kN for loading at this location, however the punch cone was still noticeable, albeit much larger and non-uniform than would be anticipated. Both CSA A23.3 and CSA S6 define a punching shear failure for this case as a four sided failure, approximately rectangular in shape. Figure 4-53 shows a picture of the underside of the panel following failure and Figure 4-54 shows the load deflection curve for the loading.

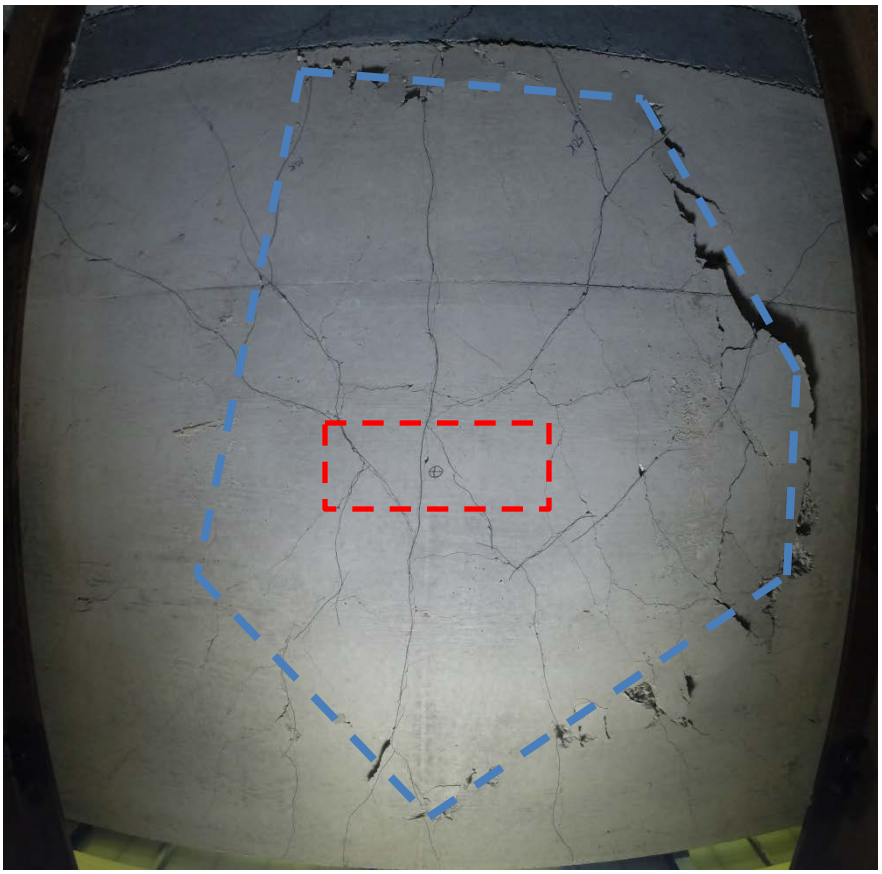

Figure 4-53. SB-1: Underside of slab following failure loading on centre of panel. (Red indicates load location and blue is exterior edge of punch cone)

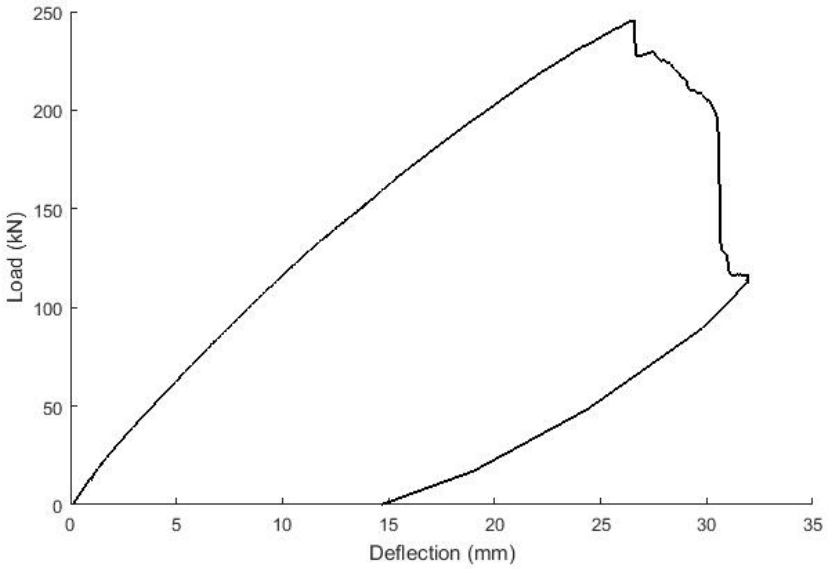

Figure 4-54. SB-1: Load-displacement curve for loading on centre of panel.

4.3 Precast Slab Specimen Tests: Ribbed GFRP Specimens

As described previously, two precast concrete slab specimens were constructed using the ribbed GFRP reinforcement. The first specimen was tested under fatigue loading at three locations, while the second specimen was only fatigued adjacent to the closure strip. Both specimens were tested to failure under static loading following the fatigue loading regimen.

4.3.1 Precast Slab Specimen with Ribbed GFRP Fatigued at Three Locations (Specimen RB-3)

This specimen was intended to undergo fatigue loading for 2,000,000 cycles at three locations: the centre of the panel, adjacent to the closure strip and centred on the closure strip with the loading was performed in that order. Following completion of fatigue loading, the slab was to be loaded to static failure at two locations, first adjacent to the closure strip and second on the centre of the fatigued panel. However, the full testing program for this specimen could not be completed due to premature bar failures during fatigue cycles.

4.3.1.1 Fatigue Location 1 – Centre of Panel

The first location to undergo fatigue loading was the centre of one of the precast panels. The measured specimen response at this location showed significantly increased deflections compared to the slabs reinforced with sand-coated bars. Deflections increased rapidly during initial cycles followed by an approximately linear increase, however the linear increase in deflection was much more pronounced than that experienced by the sand-coated bar reinforced slabs. The maximum deflection recorded after 2,000,000 cycles was nearly 11 mm compared to just 5.7 mm for the precast slab specimens with sand-coated bars. Figure 4-55 shows the variation of measured slab deflection at the peak and valley loads over the course of the fatigue loading to 2,000,000 cycles.

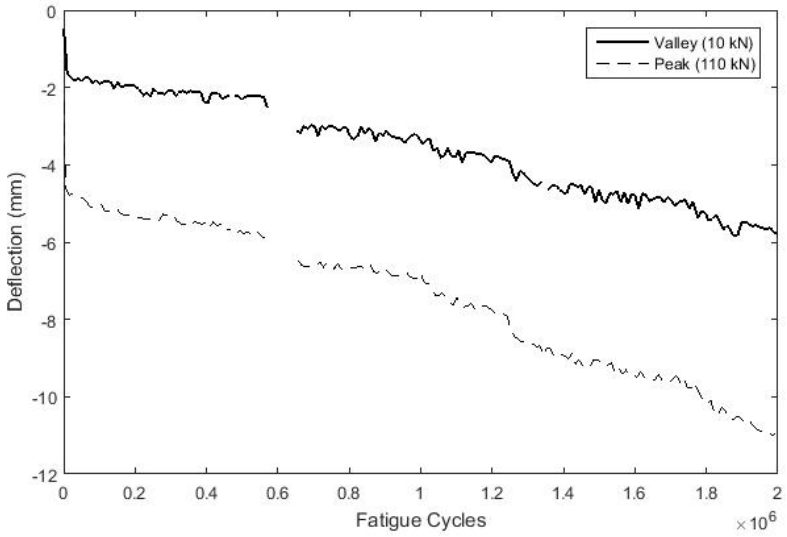

Figure 4-55. RB-3: Variation of peak and valley deflection response over time for centre of panel load location (deflection measured at load location).centre

The deflection range increased slightly over the first 1,000,000 cycles, but then increased at a greater rate for the second 1,000,000 cycles. Figure 4-56 shows the variation of deflection range (peak minus valley) versus cycle count.

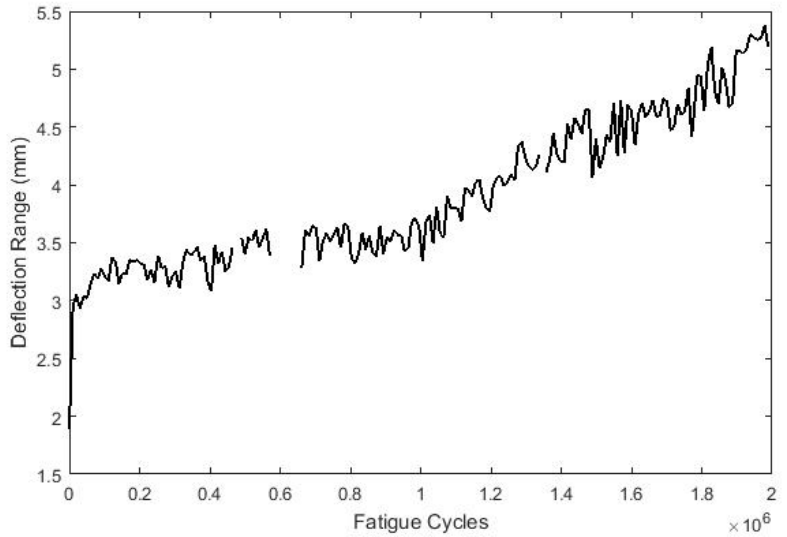

Figure 4-56. RB-3: Variation of deflection range (peak minus valley) over time for centre of panel load location.

The deflection range experienced during this fatigue testing increased throughout the fatigue loading. The marked difference between the rate of increase in deflection range at approximately 1,000,000 cycles coincided with noticeable crack formation and expansion (existing cracks growing wider) during testing.

The cracking behaviour of this specimen was notably different from the previously tested precast slab specimens with sand-coated GFRP bars. Specifically, the formation of a large crack extending longitudinally over the specimen length was noted at approximately 1,350,000 cycles. This crack was approximately aligned with the longitudinal bar adjacent to the centre longitudinal bar. The crack propagated through the UHPC closure strip and through the length of the non-loaded panel. As fatiguing continued, this crack continued to grow in size to the point where small chunks of concrete were falling from the crack. Figure 4-57 shows the underside of the slab following fatigue loading at the centre of panel location.

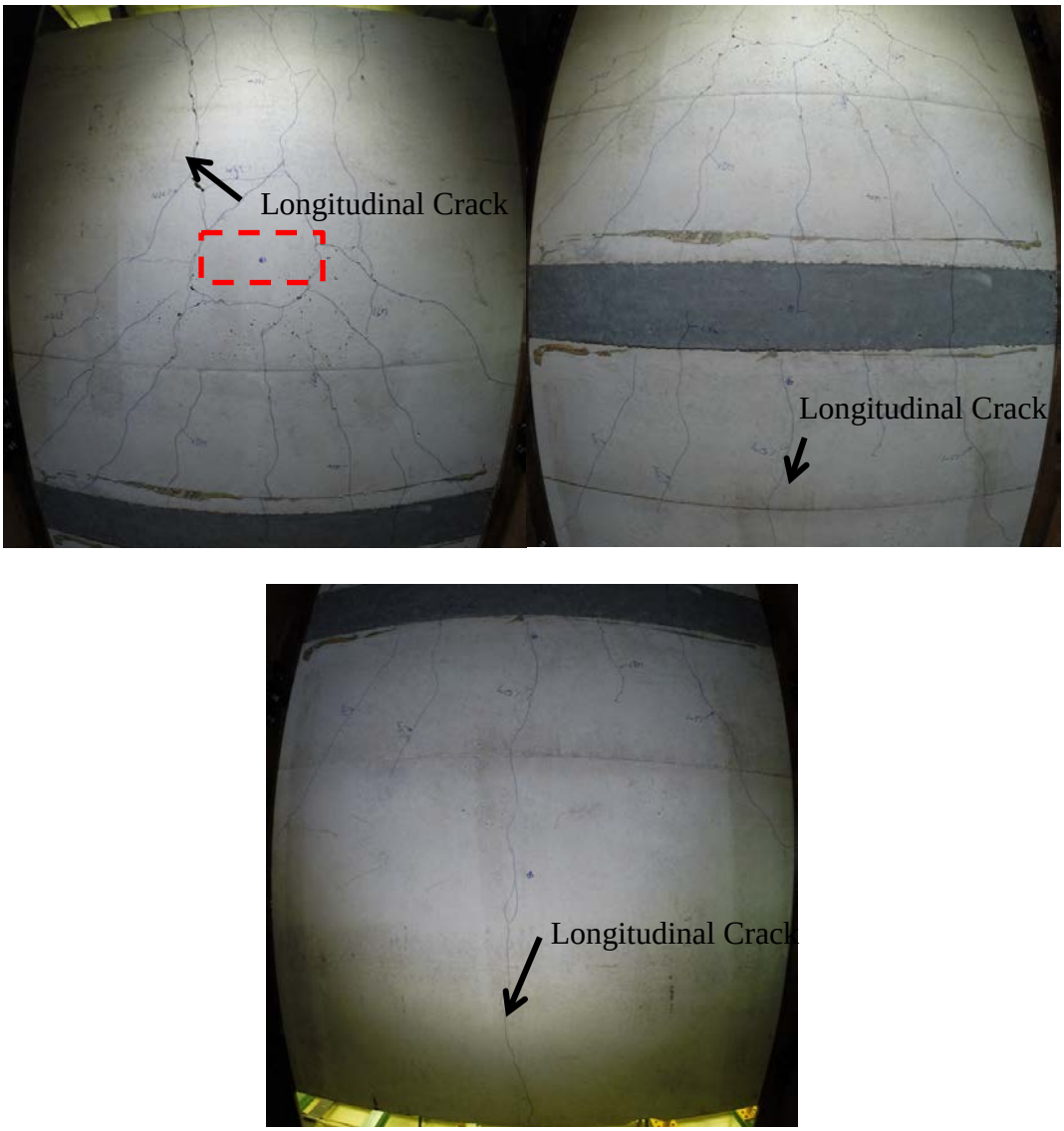

Figure 4-57. RB-3: Underside of slab after fatigue loading. (Top left: slab loaded adjacent to panel, Top Right: closure strip, Bottom: panel loaded in centre)

In order to evaluate the bar strain at various points during the fatigue loading, several plots depicting microstrain versus cycle count were created. Several sets of strain gauge data were unavailable either from the start of testing or became non-functional during fatigue loading. Figure 4-58 shows the strain in the bottom longitudinal bars, Figure 4-59 shows the strain in the top longitudinal bars, Figure 4-60 shows the strain in the transverse bars and Figure 4-61 shows the concrete strains. The gauge names and locations are located in Chapter 3, Figure 3-18.

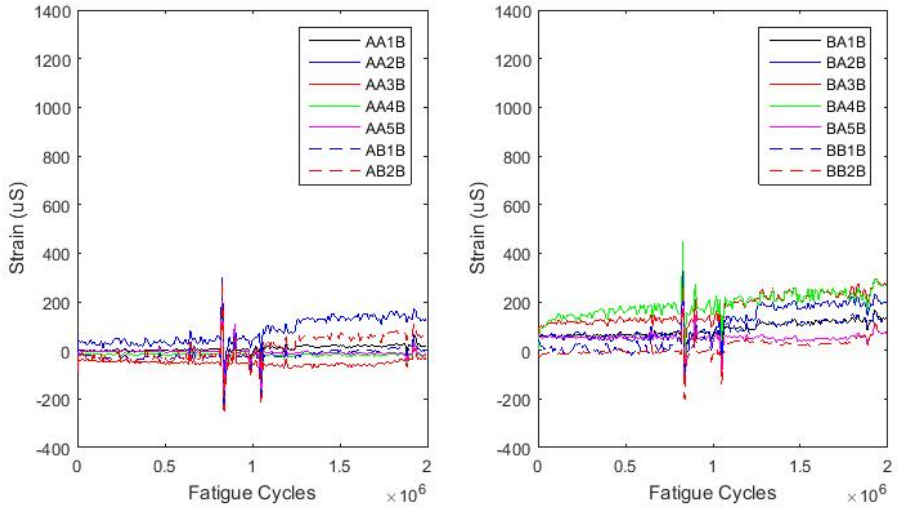

Figure 4-58. RB-3: Strain range for bottom longitudinal bars with load on centre of panel.

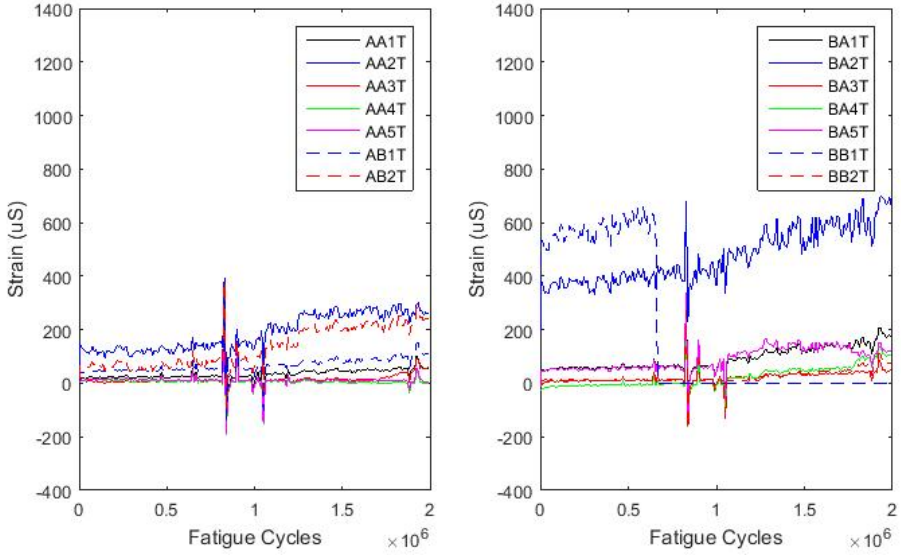

Figure 4-59. RB-3: Strain range for top longitudinal bars with load on centre of panel.

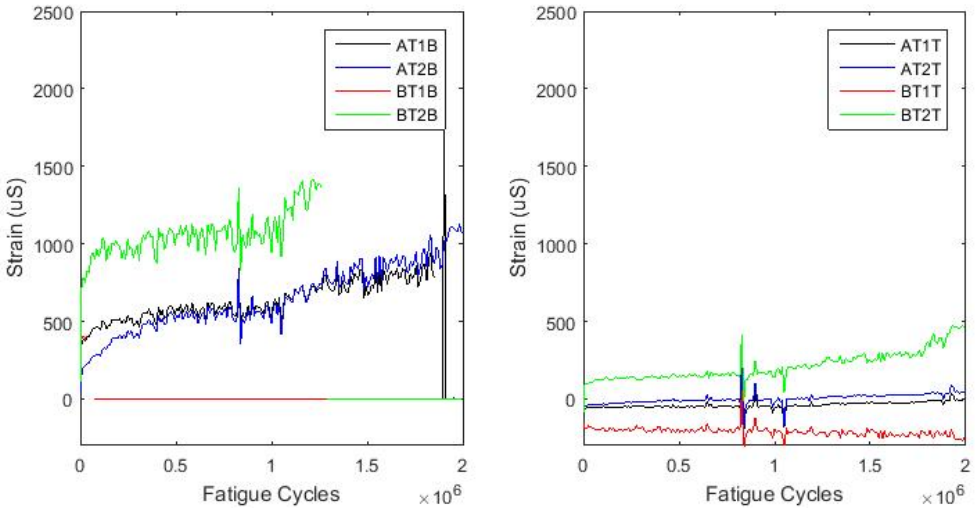

Figure 4-60. RB-3: Strain range for transverse bars with load on centre of panel.

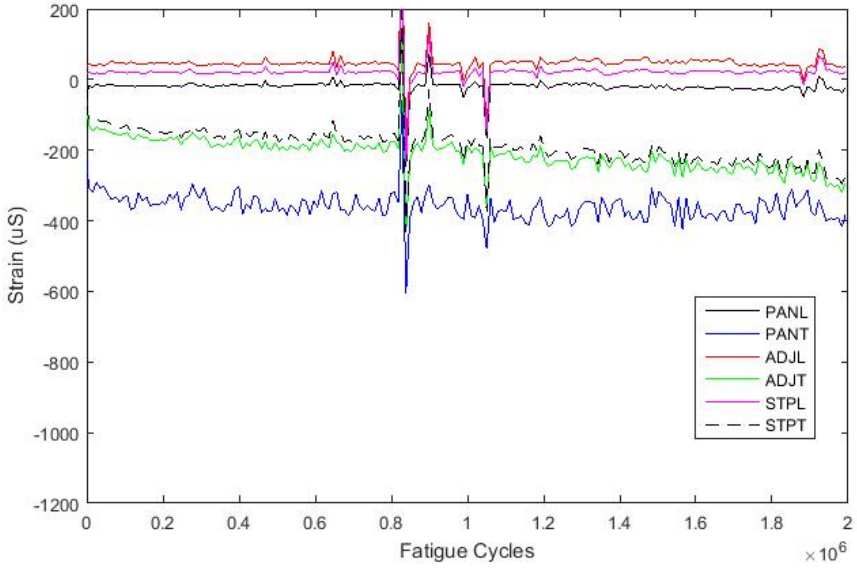

Figure 4-61. RB-3: Strain range for top fibre of concrete with load on centre of panel.

Based on these plots it is clear that the greatest strains were experienced in the bottom transverse reinforcement directly below the load point before it stopped recording data. Similar to the sudden change noted in Specimen SB-1, there is a discontinuity in all gauge readings at approximately 850,000 cycles. This is likely due to a sudden temperature change experienced by the specimen at this point in time. These strain plots also clearly show the redistribution of strain as the specimen continues to crack. All transverse and longitudinal bars clearly show an

increased rate of strain change after approximately 1,000,000 cycles as cracks were noticed to grow both longer and wider. In particular, the large crack that appear around 1,350,000 cycles noted above coincides with the failure of the gauge on the transverse bar below the load point. Unfortunately, a significant number of gauges were not available during testing for a variety of reasons, leading to a lack of data at several points on the reinforcing bars.

4.3.1.2 Fatigue Location 2 – Adjacent to Closure Strip

Following fatigue loading in the centre of the panel, fatigue loads were applied adjacent to the closure strip. Similar to the loading at the first location, the deflections increased quickly throughout fatigue loading. During loading, new cracks formed and the existing cracks widened. Of particular interest is the large crack noted from the previous load location. This crack continued to grow wider in both slabs as well as through the UHPC closure strip. Beginning around 1,100,000 cycles, a loud crunching or rubbing sound could be heard during the unloading portion of the fatigue load cycles. This sound occurred intermittently during the remainder of the test. At 1,400,000 cycles, the bottom transverse bar at the free edge of the panel that was loaded for the first fatigue load location was observed to be broken and moving independently from each other. Figure 4-62 shows the bar in question, including the visible partial-depth fracture of the bar.

Figure 4-62. RB-3: Broken transverse bar at edge of slab. Arrow indicates fracture location.

Shortly after this bar fracture was noticed, the deflection under fatigue loading began to increase rapidly. Just prior to reaching 1,500,000 cycles, the deflection increased by approximately 5 mm over a period of less than 10,000 cycles, suggesting that the fatigue damage was excessive and that the slab had failed in serviceability and the fatigue test was stopped. Upon further inspection the longitudinal crack over the length of the precast slab specimen had widened to approximately 3 mm in some locations. Figure 4-63 shows the variation of peak and valley slab deflections over the course of the fatigue loading.

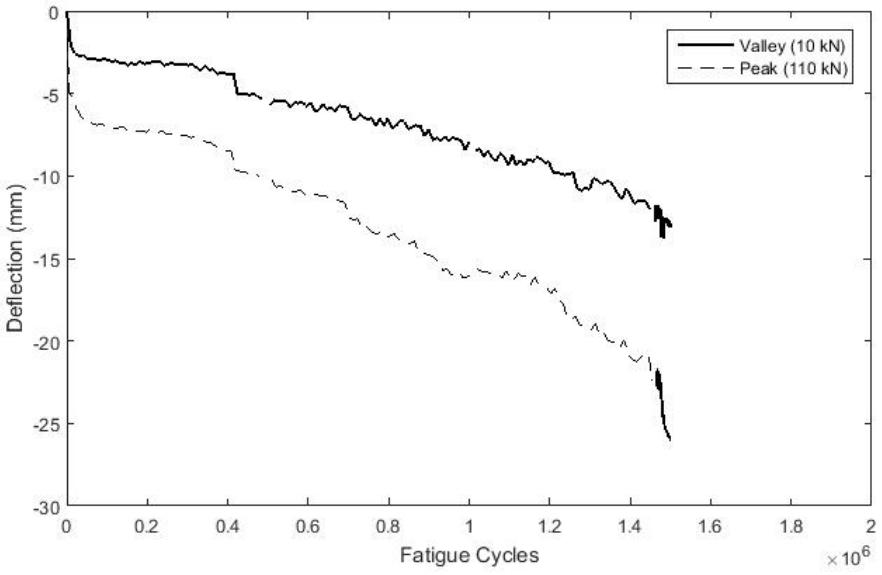

Figure 4-63. RB-3: Variation of peak and valley deflection response over time for centre of panel load location (deflection measured at load location).

The deflection range (peak minus valley) is plotted in Figure 4-64. This figure clearly shows an increase in the deflection range over time culminating in a significant increase at the same time the overall slab deflections were increasing rapidly. This final dramatic increase in deflection range reinforces the theory of the bottom transverse reinforcement being broken since the top bars were able to sustain the 'valley' load of 10 kN without excessive deflections, but at peak load of 110 kN, the top bars alone were unable prevent severe deflections from occurring.

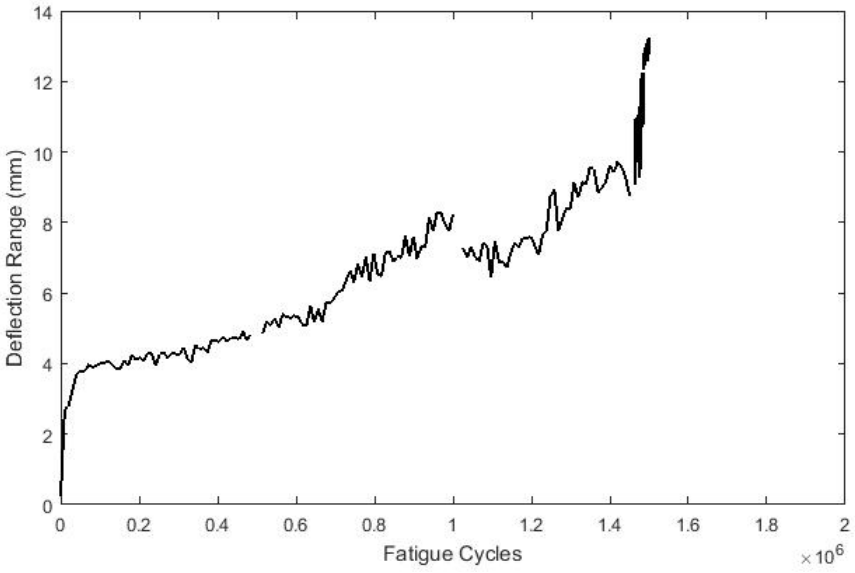

Figure 4-64. RB-3: Variation of deflection range (peak minus valley) over time for centre of panel load location.

Following this premature fatigue failure of the slab, photos of the underside of the slab were taken as shown in Figure 4-65. These photos clearly show a crack that extends for the entire length of the slab and crosses all transverse bars. Based on the excessive width of the crack it was expected that all transverse bars (perpendicular to the crack) were likely broken. This conclusion was reinforced through watching the motion of the slab the crack opening and closing with one edge of the crack deflecting downward several millimeters more than the opposite crack edge.

Figure 4-65. RB-3: Underside of slab after fatigue loading. (Top left: slab loaded adjacent to panel, Top Right: closure strip, Bottom: panel loaded in centre)

Figure 4-66 shows the strain in the bottom longitudinal bars, Figure 4-67 shows the strain in the top longitudinal bars, Figure 4-68 shows the strain in the transverse bars and Figure 4-69 shows the concrete strains. During loading at this location, none of the strain gauges on the bottom transverse reinforcement were operational. Additionally, several other gauges were not available during testing for a variety of reasons, leading to a lack of data at several points on the reinforcing bars. The gauge names and locations are located in Chapter 3, Figure 3-18.

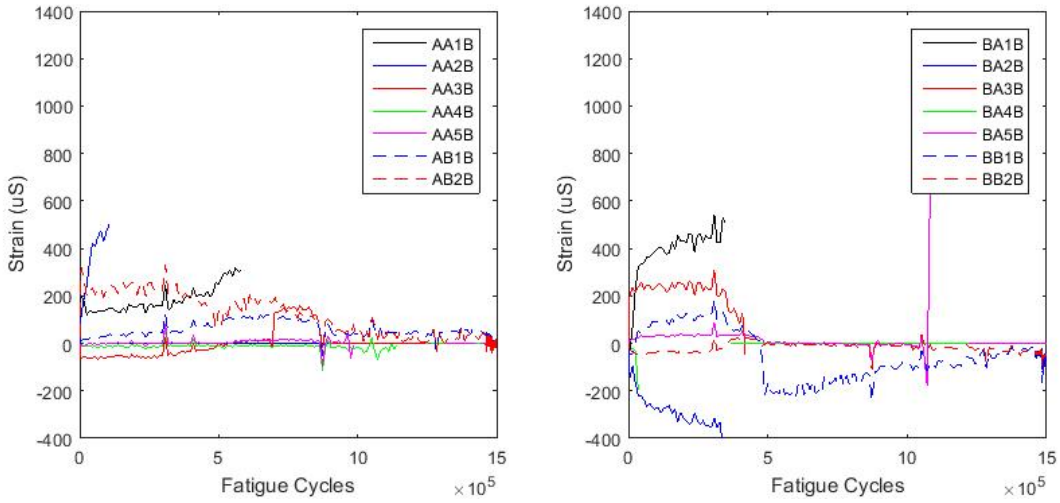

Figure 4-66. RB-3: Strain range for bottom longitudinal bars with load adjacent to closure strip.

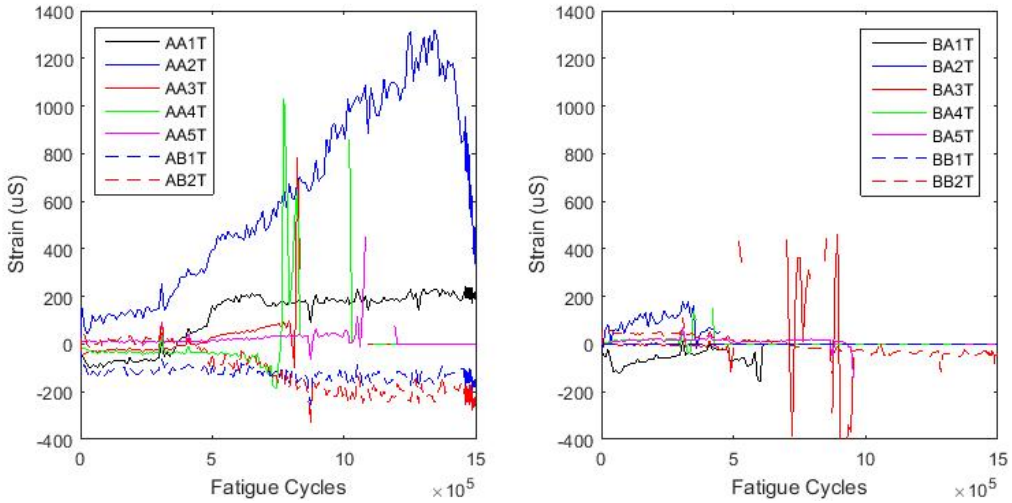

Figure 4-67. RB-3: Strain range for top longitudinal bars with load adjacent to closure strip.

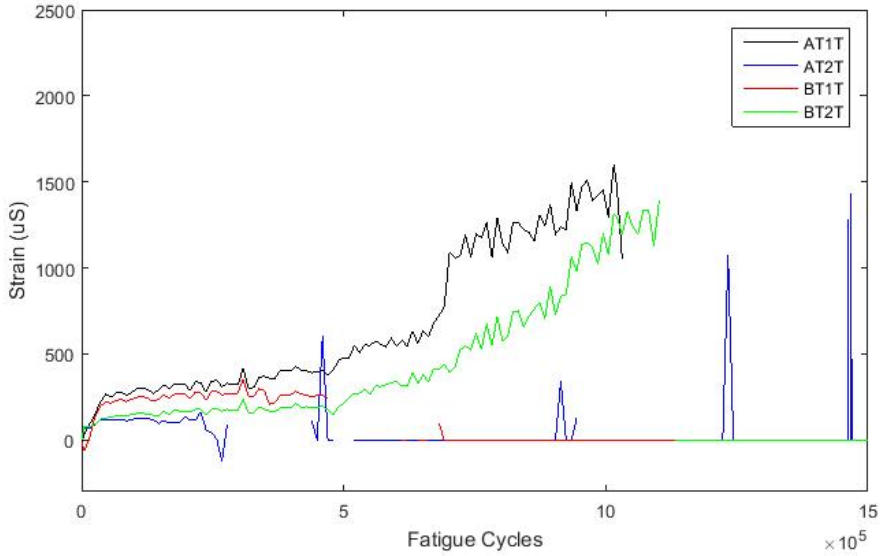

Figure 4-68. RB-3: Strain range for top transverse bars with load adjacent to closure strip.

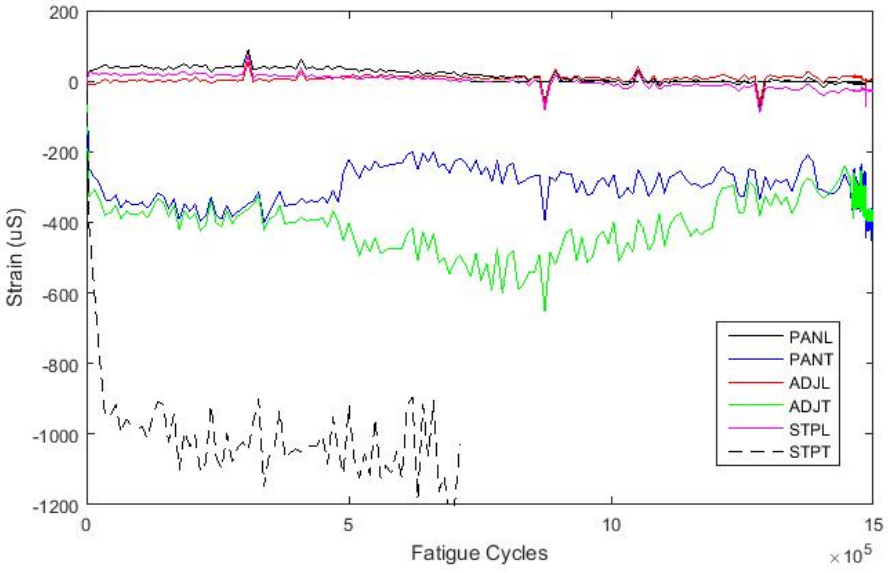

Figure 4-69. RB-3: Strain range for top fibre of concrete with load adjacent to closure strip.

The plots shown above similarly assist in demonstrating the redistribution of strain as the bottom transverse bars fractured. Figure 4-68 clearly shows a significant increase in strain range for the two operational gauges on top transverse reinforcement. This significant increase in strain range indicates a failure of the bottom reinforcement resulting in increased strain experienced by the top reinforcement. The two gauges in this case are the top transverse bar below the first and

second load location, which indicates that redistribution of strain was occurring across the entirety of the specimen. Similarly, the increase in the strain ranges experienced in the longitudinal reinforcement shows the redistribution of strains as transverse stiffness is lost as bottom transverse reinforcement fractures and forces are redistributed longitudinally to regions of relatively high stiffness (where the bottom transverse reinforcement was still intact).

4.3.1.3 Failure Loads Under Static Loading

Following fatigue load at the two locations, the slab was subjected to static loading to failure adjacent to the closure strip. Loading was applied in displacement control at a rate of 2 mm/min. Unlike the slabs reinforced with sand-coated bars, the slab did not fail in punching shear, but rather experienced a concrete crushing failure on the top surface of the slab along the length of the concrete slab. Figure 4-70 shows a photo of the top of the slab after failure. Figure 4-71 shows the load versus displacement plot of loading up to failure with an ultimate load at failure of approximately 200 kN. Figure 4-72 shows three photos of the underside of the slab after failure and indicates the load location.

Figure 4-70. RB-3: Concrete crushing failure on top of slab.

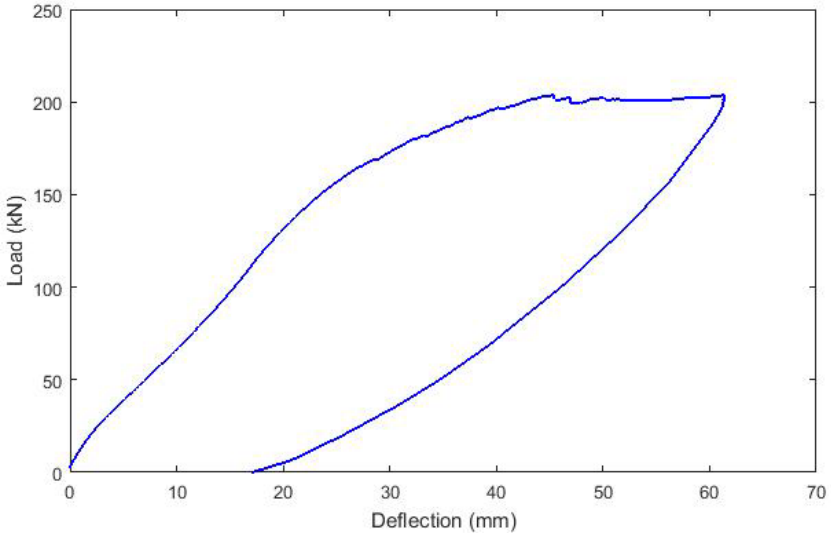

Figure 4-71. RB-3: Load-deflection curve for failure adjacent to the closure strip.

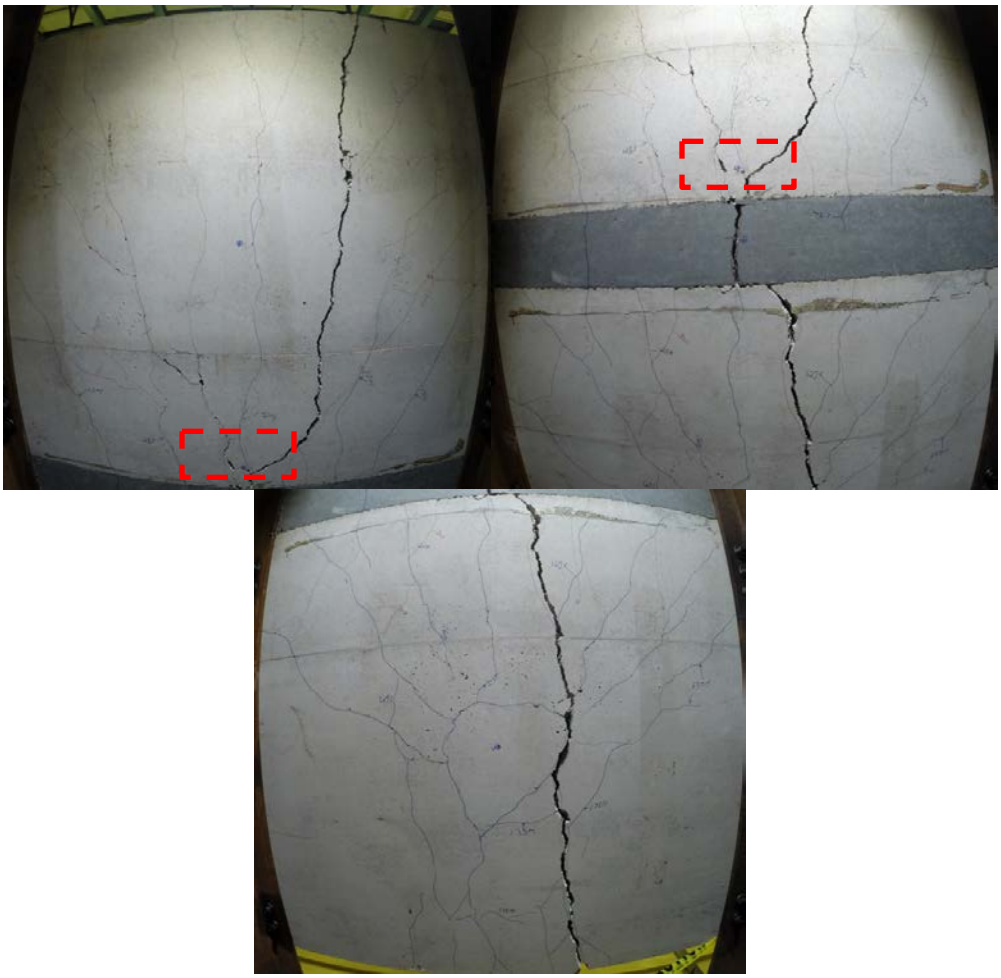

Figure 4-72. RB-3: Underside of slab after fatigue loading. (Top left: slab loaded adjacent to panel, Top Right: closure strip, Bottom: panel loaded in centre)

During static loading at this location, the slab underwent significant curvature in the transverse direction for the entire length of the slab due to significantly decreased stiffness caused by the fractured bars. The reduced stiffness in the transverse direction prevented the slab entering two-way bending, which would have resulted in a punching shear failure. The one-way action resulting from the reduced stiffness resulted in the concrete crushing due to excessive top concrete strain in the top fibre of the slab in the transverse direction. Figure 4-73 shows a diagram of the transverse concrete strain near the load point during static loading. It can be seen that it nearly reaches the failure strain of 0.0035 (3500 microstrain).

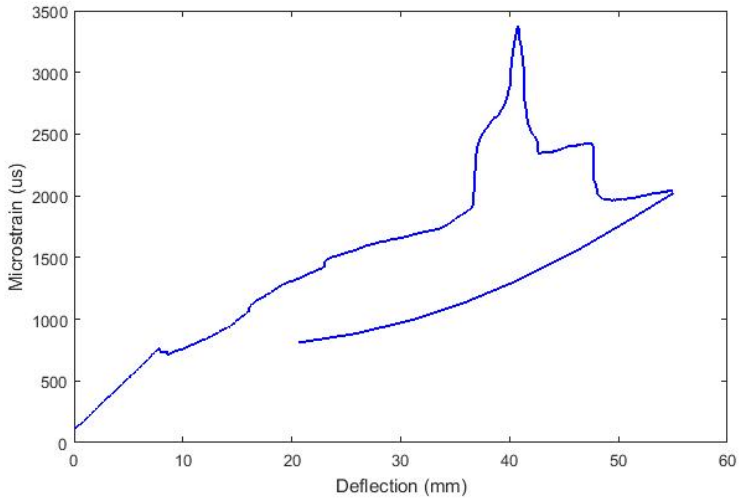

Figure 4-73. RB:3: Transverse top fibre concrete strain near load point during static failure loading.

In addition, the precast concrete surrounding the corner shear pockets cracked resulting the slab slipping and creating an approximately 3 mm gap between the UHPC shear pocket and the precast concrete panel. Figure 4-74 shows typical cracking at the edge shear pockets.

Figure 4-74. RB-3: Cracking and slip of slab near corner shear pocket.

4.3.2 Precast Slab Specimen with Ribbed GFRP Fatigued at One Location (Specimen RB-1)

The second precast slab specimen with ribbed GFRP bars was only subjected to fatigue loading adjacent to the closure strip. Prior to fatigue loading, the specimen was loaded statically up to the peak fatigue load of 110 kN at the three load locations (centre of panel, adjacent to closure strip and centre of closure strip) in order to establish initial stiffness and deflections of the slab at the load locations.

4.3.2.1 Initial Static Tests to Characterize Slab Behaviour

The first static load location was adjacent to the closure strip. Figure 4-75 shows the load-deflection response for the two static load cycles at this location. Note that the displacement measurements were zeroed after the first cycle for plotting purposes.

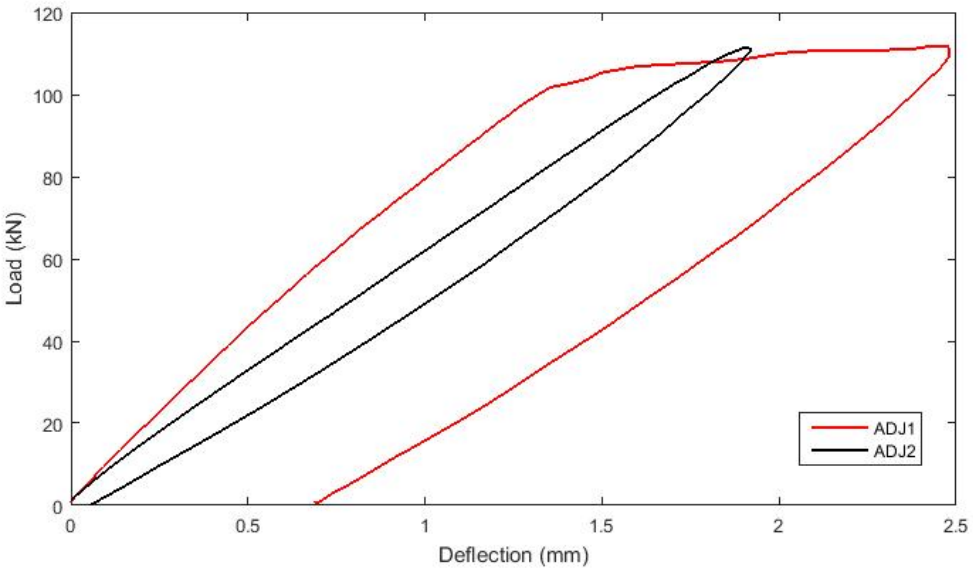

Figure 4-75. RB-1: Load-deflection responses for first two static cycle at service loads adjacent to closure strip.

The first load cycle showed a bi-linear load-deflection response with concrete cracks forming at around 100 kN leading to a pronounced decrease in stiffness and increase in deflection between 100 kN and 110 kN. The maximum deflection at peak load was approximately 2.5 mm. A plastic or permanent deflection of 0.7 mm remained after unloading. The second load cycle showed an approximately linear load-deflection response up to 110 kN since the slab was already cracked. The stiffness of the slab was reduced in comparison to the initial stiffness of the first load cycle.

The second location to undergo static tests was the centre of the closure strip. Figure 4-76 shows the load deflection curves for these two static load cycles. Note that the displacement measurements were zeroed after the first cycle for plotting purposes.

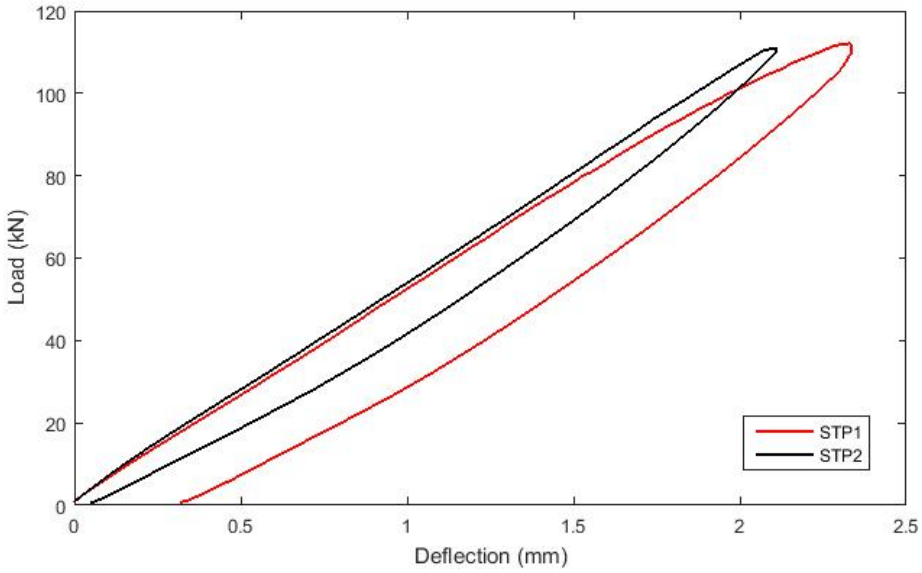

Figure 4-76. RB-1: Load-deflection curves for first two static tests at service loads on the closure strip.

The load-displacement response for the load on the closure strip shows a linear behaviour for both the first and second cycles with approximately 0.3 mm of plastic deformation for the first load and almost perfectly elastic for the second load cycle with minimal permanent deflection. Additionally, since cracking had already occurred during static service loads adjacent to the closure strip the stiffness was almost exactly the same for the first and second load cycle. The peak deflection for the first cycle was slightly greater than for the second cycle with a total deflection of 2.3 mm for the first cycle and 2.0 mm for the second cycle. This slight difference is likely due to minor cracking, or cracks extending during the first load cycle. This deflection difference is also the same as the difference between the plastic deformations of the two cycles.

The final location to undergo static loading was the centre of one of the precast concrete panels. This loading resulted in the formation of significant cracking in both the longitudinal and transverse directions on the underside of the panel. Figure 4-77 shows the load-deflection curves for these two static load cycles. Note that the displacement measurements were zeroed after the first cycle for plotting purposes.

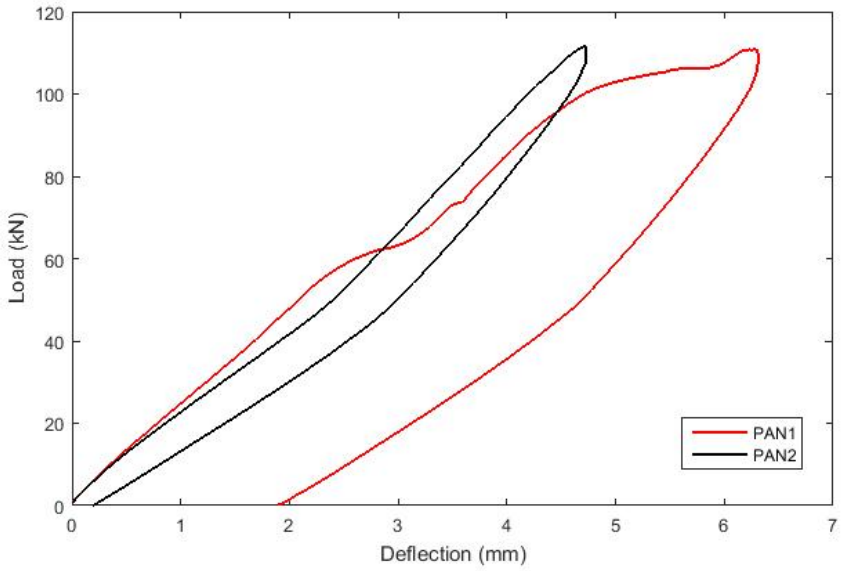

Figure 4-77. RB-1: Load-deflection curves for first two static tests at service loads on the centre of the panel.

The first static load cycle had a slightly greater initial stiffness compared to the second load cycle, but at approximately 60 kN the stiffness was reduced and deflections significantly increased. Similarly, at approximately 100 kN, deflections increased significantly. These deflection increases are due to crack formation, resulting in a non-uniform load-deflection curve with a total deflection of 6.3 mm at peak load. The load-deflection response during the second static load cycle was less stiff initially, but resulted in very little plastic or permanent deformation. The second load cycle is bi-linear and appears to grow more stiff at approximately 50 kN, possibly due to the boundary conditions at this location causing strain redistributions due to the free edge near the load behaving in one-way bending and the closure strip side behaving in two-way bending.

The underside of the slab was photographed to capture the crack patterns following the initial static loads at the three locations. Figure 4-78 shows the underside of the slab after the static loads at the three locations. The cracks from the static loads are marked to be more visible.

Figure 4-78. RB-1: Underside of slab after initial static loading. (Top left: slab loaded adjacent to panel, Top Right: closure strip, Bottom: panel loaded in centre)

The crack from the initial load location adjacent to the strip extended along the midspan centreline of the two precast panels, but did not extend through the UHPC closure strip. The second load location, on the closure strip, resulted in cracks in the transverse direction of the strip (parallel to precast panel-UHPC interface). Cracks propagating in this direction were not viewed in any other specimen at any point during their testing. The load at the third location, at the centre of one of the panels resulted in cracks in the longitudinal direction as well as cracks extending from the load point to the support girders near the closure strip.

Comparing the static tests at the three locations, it was clear that the slab specimen had a significantly lower stiffness when subjected to loading at the centre of the panel compared to the response for loading adjacent to the closure strip or directly on the closure strip. Figure 4-79 and Figure 4-80 shows a comparison of the first and second static cycles for the three load locations.

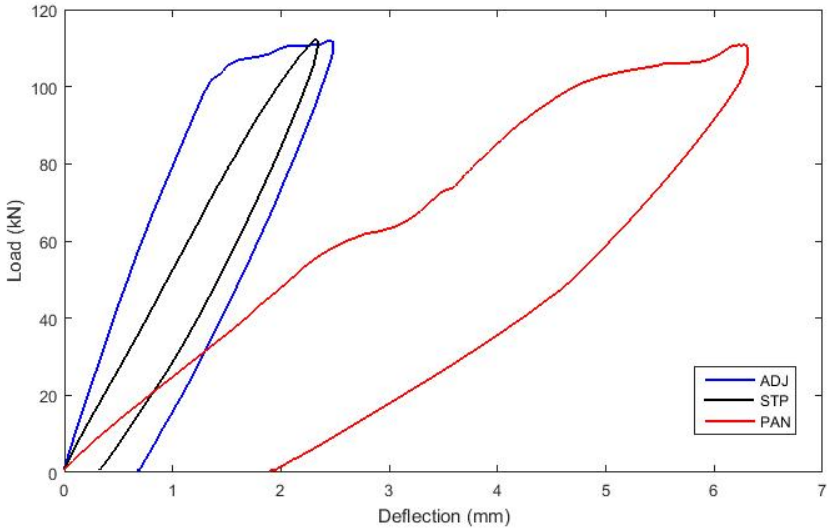

Figure 4-79. RB-1: Comparison of load deflection responses at three locations for first static service load cycle.

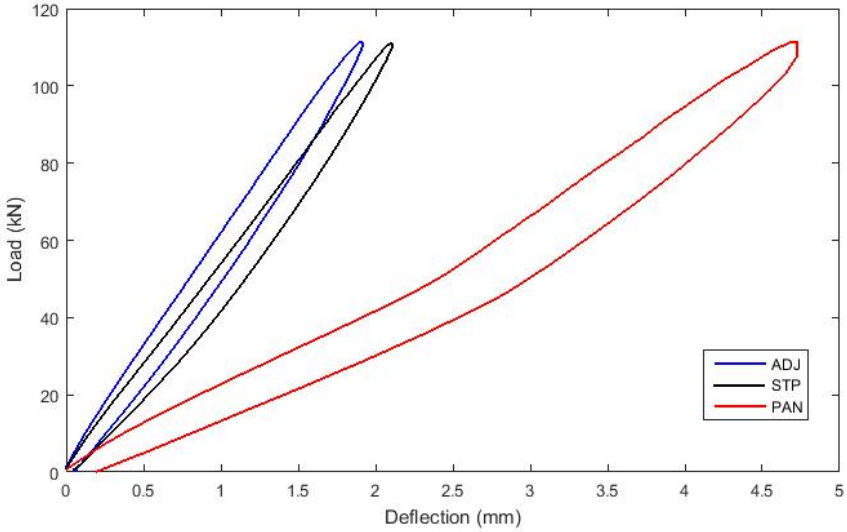

Figure 4-80. RB-1: Comparison of load deflection curves responses at three locations for second static service load cycle.

Similar to Specimen SB-1, the specimen is more stiff for loading adjacent to the closure strip and on the closure strip compared to loading on the centre of one of the panels. This is due to the nature of the boundary conditions with the two load points near the centre of the specimen behaving with two-way bending. The load on the centre of one of the panels behaves in a combination of one-way and two-way bending due to the free edge on one side and the UHPC closure strip on the other side. This stiffness difference is also noticed through the numerous cracks that propagated when the centre of the panel was loaded compared to the relatively few cracks that propagated when loading near the closure strip.

4.3.2.2 Fatigue Loading Adjacent to the Closure Strip

As mentioned previously, this precast slab specimen was only subjected to fatigue loading adjacent to the closure strip, as this was deemed to be the critical loading location for this slab system. Figure 4-81 shows the measured peak and valley deflection response over the course of fatigue loading at the centre of the panel.

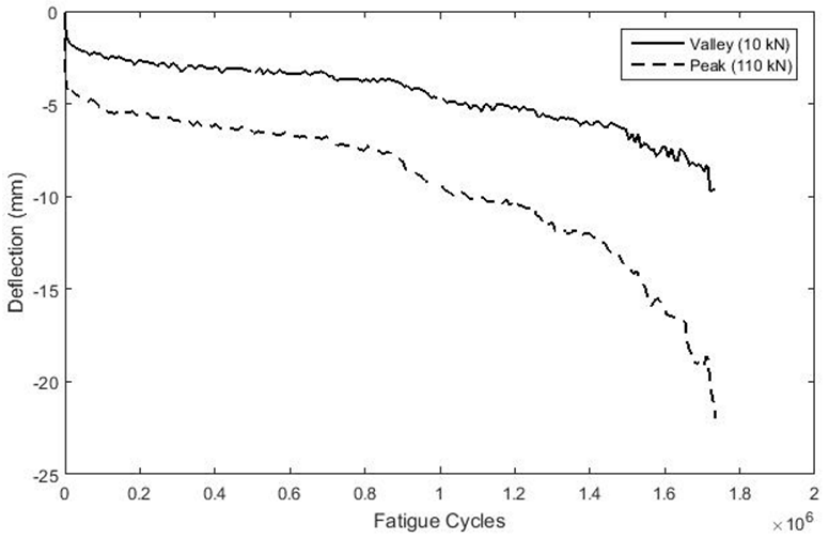

Figure 4-81. RB-1: Variation of peak and valley deflection response over time for adjacent to the closure strip load location (deflection measured at load location).

During fatigue testing, the deflection increased significantly during the first several thousand cycles followed by an approximately linear increase in deflection until approximately 800,000 cycles. After this point, the deflection increased somewhat sporadically until the test reached

1,500,000 cycles, after which slab deflections increased significantly. Eventually, the peak deflections approached 20mm and it was suspected that the bottom transverse bars had fractured, and the test was stopped due to safety concerns after 1,735,000 cycles.

Figure 4-82 shows the deflection range (peak minus valley) variation with cycle count. Similar to the trend in peak and valley defections, it can be seen that after the initial deflection range increase during the first several thousand cycles, it remained fairly constant until 800,000 cycles. After this point the deflection range increased almost exponentially until the test was stopped.

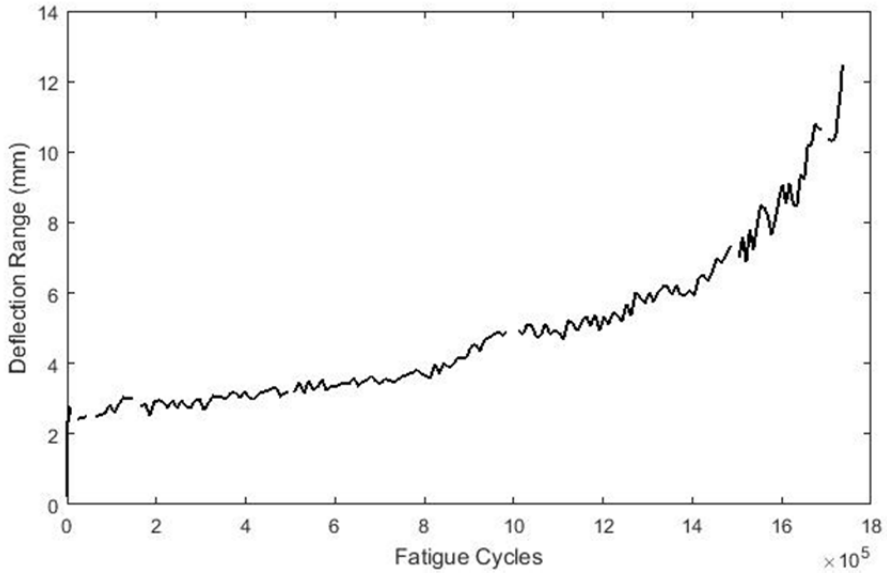

Figure 4-82. RB-1: Variation of deflection range (peak minus valley) over time for adjacent to the closure strip load location.

In addition to the load-deflection response measured continuously during fatigue testing, the fatigue loading was stopped at regular intervals to allow static load cycles to understand how the stiffness of the slab was changing throughout the test. Figure 4-83 shows static load-deflection cycles measured at various cycle counts throughout testing with each test beginning at zero deflection in order to show how stiffness changed throughout the test. It can clearly be seen that there is drastic reduction in measured stiffness near the end of the test, while the stiffness during the first several hundred cycles remained relatively consistent.

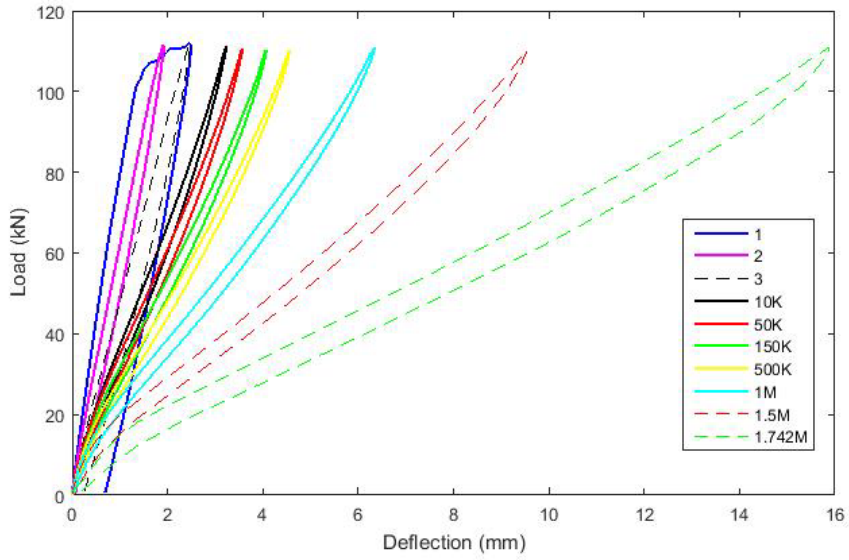

Figure 4-83. RB-1: Load-deflection curves at various cycles with initial deflection for each cycle set to zero.

In order to show the accumulation of permanent deflection throughout the test, Figure 4-84 shows a similar plot of static load-deflection cycles with each cycle starting at the permanent deflection recorded for the specimen at the time of the static test. This figure clearly shows the initial increases in permanent deflection are much less than the increases recorded at high cycle counts. It also shows that as the stiffness of the slab decreased, the overall permanent deformation increased.

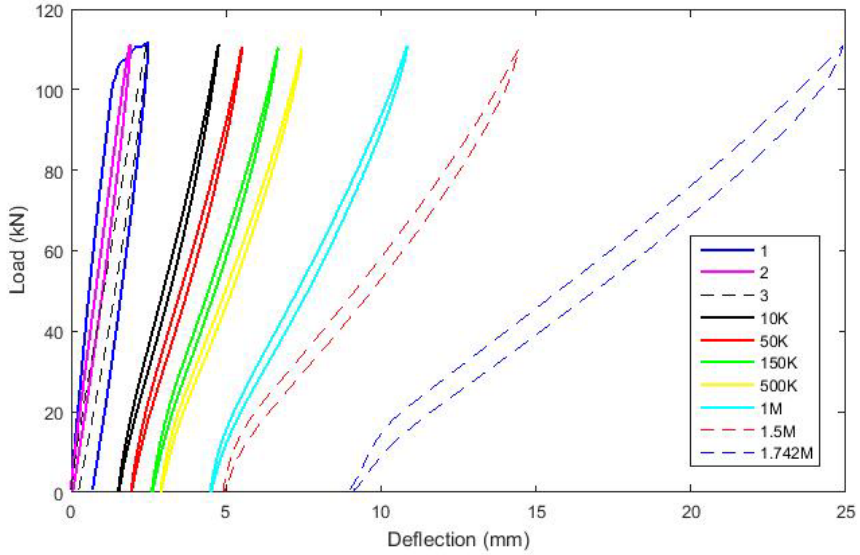

Figure 4-84. RB-1: Load-deflection curves at various load cycles with the initial deflection adjusted for plastic deformation during fatigue.

Figure 4-85 shows the strain in the bottom longitudinal bars, Figure 4-86 shows the strain in the top longitudinal bars, Figure 4-87 shows the strain in the transverse bars and Figure 4-88 shows the concrete strains. One of the primary notes of interest from these plots is from the transverse bar strains. The bottom strain gauges began to fail very early in fatigue testing. However, as the bottom bars began to break it can be seen that the top bars begin to significantly increase in strain.

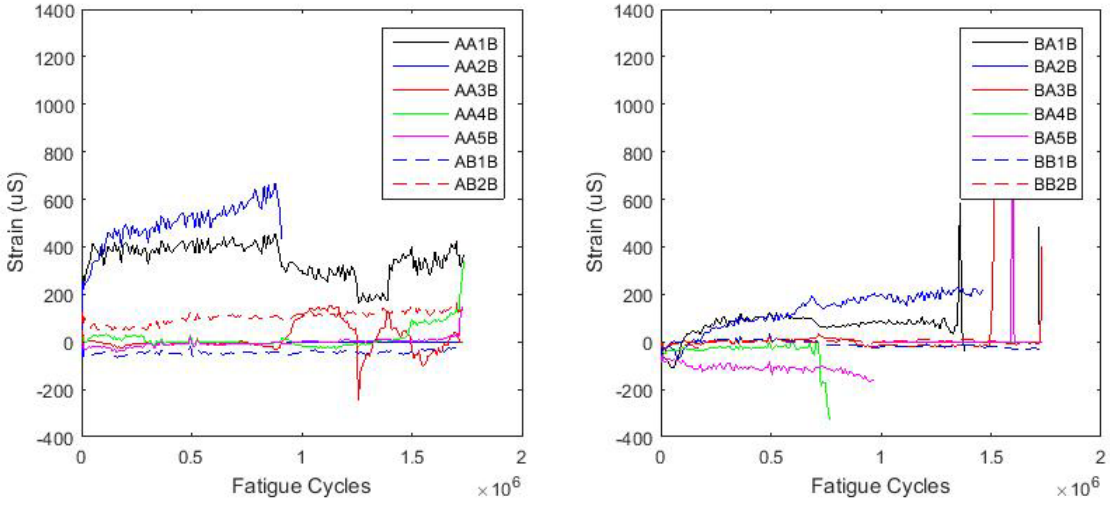

Figure 4-85. RB-1: Strain range for bottom longitudinal bars with load adjacent to closure strip.

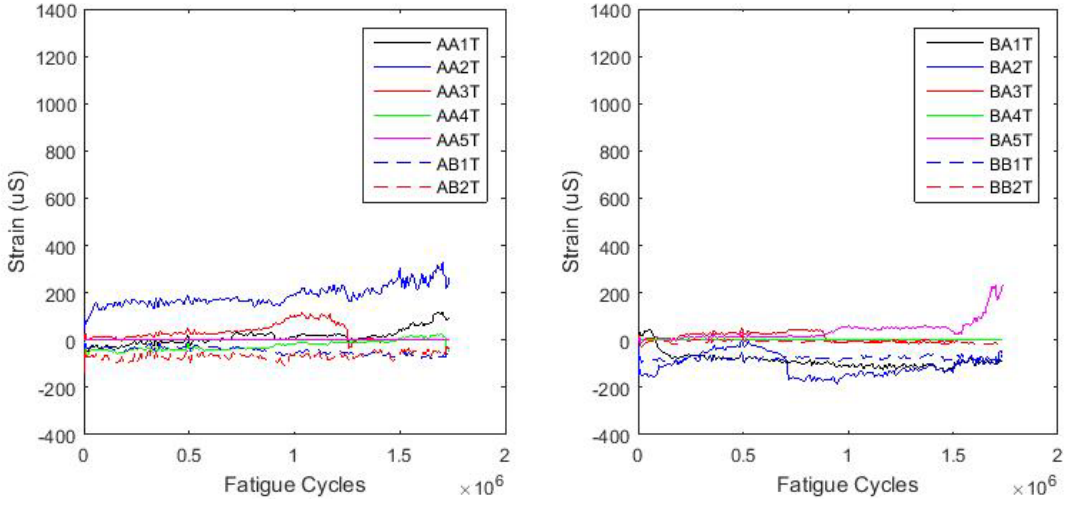

Figure 4-86. RB-1: Strain range for top longitudinal bars with load adjacent to closure strip.

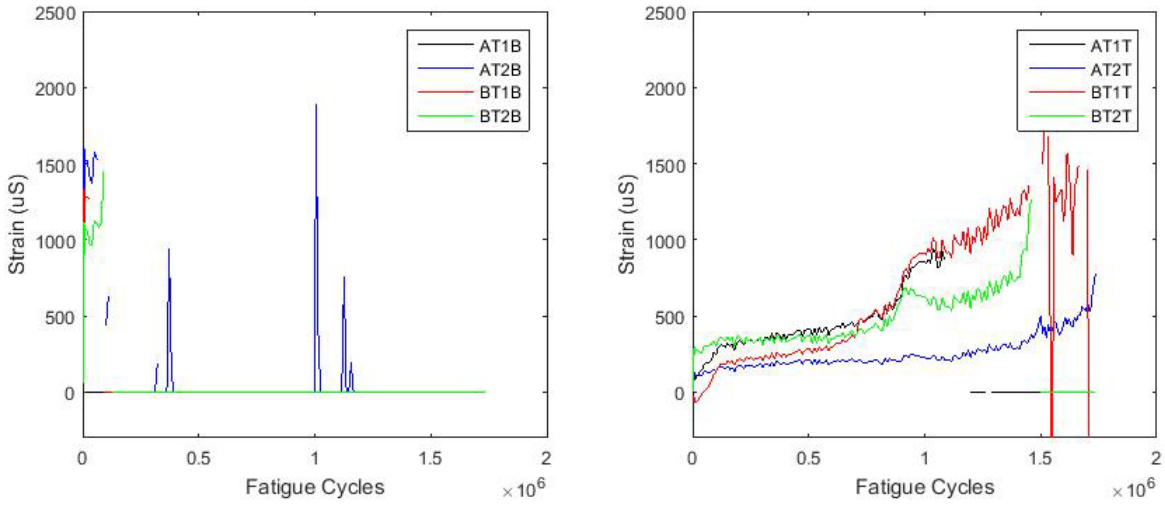

Figure 4-87. RB-1: Strain range for transverse bars with load adjacent to closure strip.

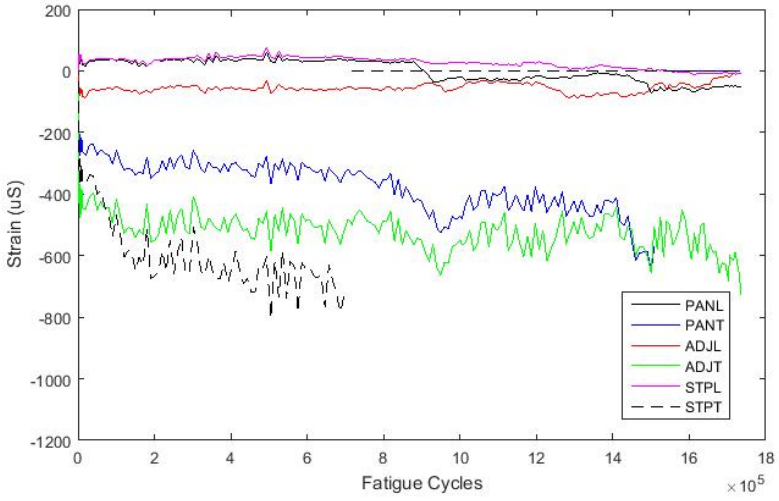

Figure 4-88. RB-1: Strain range for top fibre of concrete with load adjacent to closure strip.

The plots shown above similarly assist in demonstrating the redistribution of strain as the bottom transverse bars fractured. Unfortunately, the gauges on the bottom transverse bars ceased operation early in the test, but Figure 4-87 clearly shows a significant increase in strain range for three of the gauges on top transverse reinforcement at approximately 800,000 cycles. This significant increase in strain range indicates a failure of the bottom reinforcement resulting in increased strain experienced by the top reinforcement. The three gauges in this case are the top transverse bar below the first and second load location as well as the top transverse bar adjacent

to the closure strip within the panel loaded at the centre, which indicates that redistribution of strain was occurring across the entirety of the specimen. Similarly, the rapid changes in the strain ranges experienced in the longitudinal reinforcement shows the redistribution of strains as transverse stiffness is lost as bottom transverse reinforcement fractures and forces are redistributed longitudinally to regions of relatively high stiffness (where the bottom transverse reinforcement was still intact).

4.3.2.3 Failure Loads Under Static Loading

Following fatigue loading, the precast slab specimen was loaded to failure adjacent to the closure strip. Loading was applied in displacement control at a rate of 2 mm/min. Similar to the previously tested slab reinforced with ribbed GFRP bars (Specimen RB-3), the slab did not fail in punching shear, but rather experienced a concrete crushing failure along the length of the concrete slab. Figure 4-89 shows a photo of the top of the slab after crushing failure. Figure 4-90 shows the load versus displacement plot of loading to failure at this location with an ultimate load at failure of approximately 190 kN. Figure 4-91 shows three photos of the underside of the slab after failure and indicates the load location.

Figure 4-89. RB-1: Concrete crushing on top fibre following failure load.

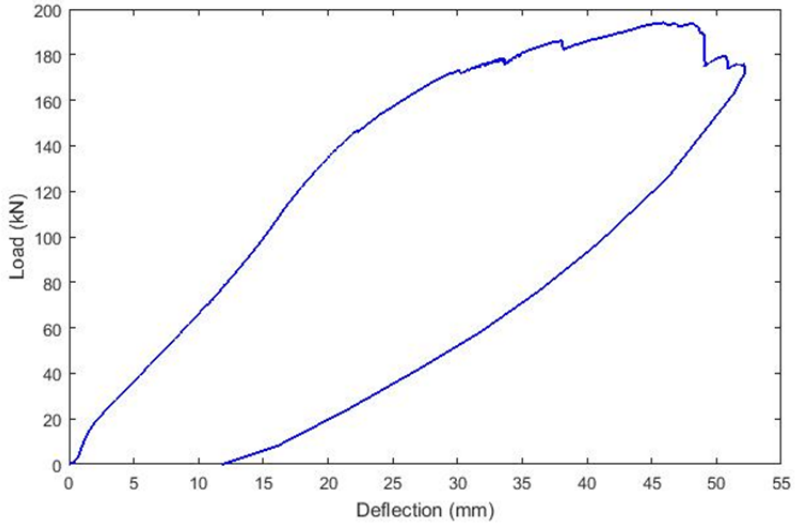

Figure 4-90. RB-1: Load-deflection curve for loading to failure adjacent to the closure strip.

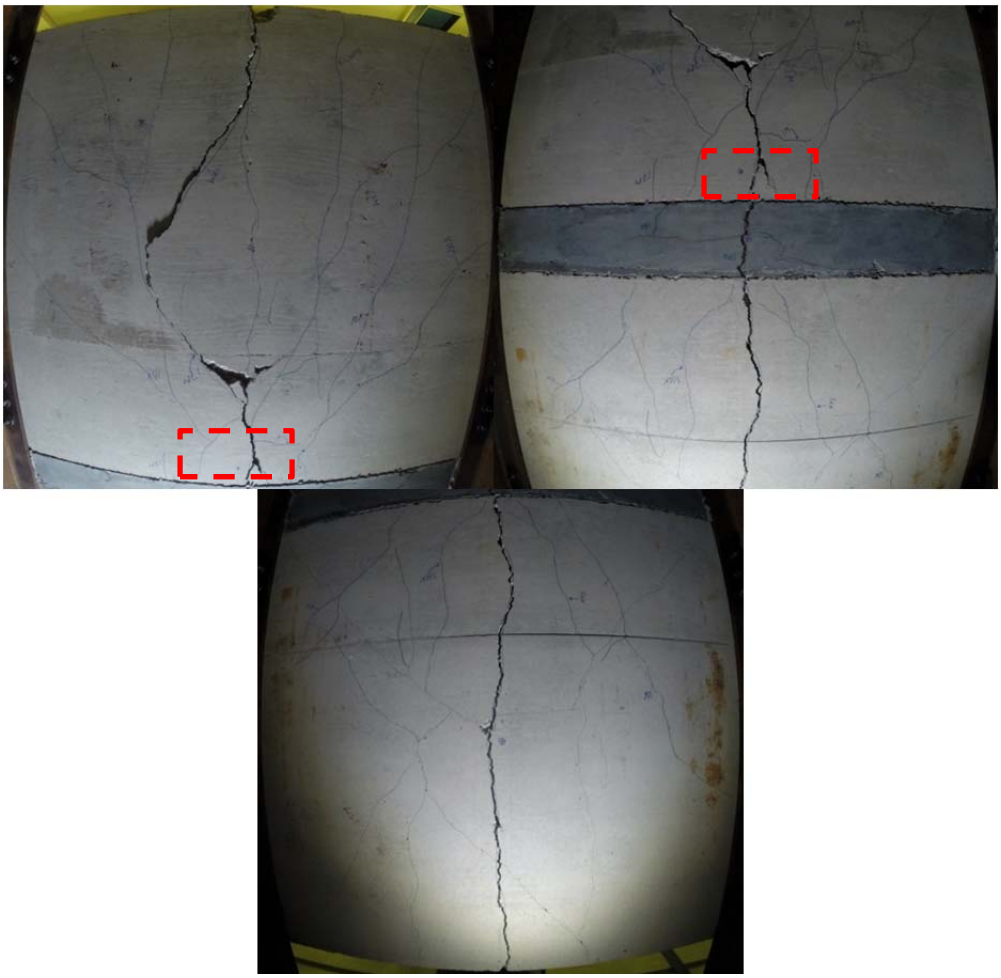

Figure 4-91. RB-1: Underside of slab after failure loading. (Top left: slab loaded adjacent to panel, Top Right: closure strip, Bottom: panel loaded in centre)

During static loading at this location, the slab underwent significant curvature in the transverse direction for the entire length of the slab due to significantly decreased stiffness caused by the fractured bars. The reduced stiffness in the transverse direction prevented the slab entering two-way bending, which would have resulted in a punching shear failure. The one-way action resulting from the reduced stiffness resulted in the concrete crushing due to excessive top concrete strain in the top fibre of the slab in the transverse direction. In addition, the precast concrete surrounding the corner shear pockets cracked resulting the slab slipping and creating an approximately 3 mm gap between the UHPC shear pocket and the precast concrete panel. Figure 4-92 shows a sample of cracking at the edge shear pockets.

Figure 4-92. RB-1: Concrete cracks near corner shear pocket during failure loading.

4.4 Precast Slab Specimen Autopsy After Completion of Testing

Once the fatigue and static testing was complete, the precast slab specimens were subjected to a destructive examination to further examine crack patterns and conditions at failure, and to confirm the occurrence of GFRP bar failures or other damage. The complete sub-assembly of the two precast slabs and the UHPC closure strip was removed from the steel girders by disconnecting the shear connection between the slabs and the girders by removing the bottom nuts on the shear bolts. The slabs were then moved outside to be cut using a concrete saw.

4.4.1 Slab Specimen SB-3 (Sand-Coated Bars Fatigued at 3 Locations)

This precast slab specimen failed in punching shear adjacent to the closure strip, followed by a less clear punching shear failure when loaded at the centre of the precast concrete panel. The conditions at the punching shear failure adjacent to the closure strip were the primary interest during the autopsy. The concrete in the punching shear cone region was removed in order to examine the failure surface and the reinforcement within the punched region. Figure 4-93 shows a photo of the top of the punching location before and after the punched concrete was removed.

Figure 4-93. SB-3: Top of punched location prior to (left) and after (right) concrete removal.

The reinforcement within this region was intact and undamaged for the majority of the punch cone. However, directly adjacent to the closure strip the top longitudinal reinforcing bar had undergone a direct shear failure. It is unclear if this failure occurred at the time of the punching failure or if it occurred after punching failure occurred while loading was continued. Figure 4-94 shows the shear failure location on the GFRP bar.

Figure 4-94. SB-3: Shear failure of top longitudinal GFRP bar after punching failure.

The slab was then turned over to examine the underside of the slab with the loose concrete removed as shown in Figure 4-95. The punching failure surface was observed to have an approximately fan shape with several extensions from the load point. This examination also clearly showed that the crack through the UHPC followed the centre longitudinal bar.

Figure 4-95. SB-3: Underside of panel after failure adjacent to the panel with concrete removed.

The failure pattern that was observed was similar to what would typically be anticipated. CSA A23.3 and CSA S6 both indicate that a punching shear failure would result in an approximate crack angle of 45°. The punching shear fan occurred at approximately this angle with the exception of one side with a slightly shallower angle. The other significant observation was the

clear separation between the UHPC and precast concrete with no interaction or ability to transfer shear remaining within the punched area.

4.4.2 Slab Specimen SB-1 (Sand-Coated Bars Fatigued at One Location)

This specimen was subjected to fatigue loading adjacent to the closure strip for 2,000,000 cycles. Following these fatigue cycles, the slab was loaded to failure (static loading) adjacent to the closure strip resulting in a three-sided punching shear cone failure. The slab was saw cut near the punching cone location in order to examine the cracks that form the punching cone. Figure 4-96 shows a photo of the cut section with the cone of failure clearly visible.

Figure 4-96. SB-1: Punching shear crack near the failure adjacent to the closure strip.

Similar to the previous test, the concrete from the punching cone was removed to examine the bars. However, unlike the previous test, none of the bars were noticeably damaged and none showed signs of shear failure. Figure 4-97 shows the punching cone location with the concrete removed.

Figure 4-97. SB-1: Punch location with the concrete removed viewed from top of slab.

Finally, the crack through the UHPC was observed to follow the location of the longitudinal bars which extend into the closure strip, as was observed for the other precast slab specimen with sand-coated GFRP bars. Figure 4-98 shows the crack in the UHPC with the broken steel fibres visible across the crack. The figure also shows a photo of the longitudinal bars extending into the UHPC closure strip. Note that there were no obvious signs of damage or broken glass fibres in the bars.

Figure 4-98. SB-1: Crack through the UHPC and longitudinal bar embedded in the UHPC.

Similar to Specimen SB-3, the failure pattern that was observed was similar to what would typically be anticipated. CSA A23.3 and CSA S6 both indicate that a punching shear failure would result in an approximate crack angle of 45°. The other significant observation was the clear separation between the UHPC and precast concrete with no interaction or ability to transfer shear remaining within the punched area regardless of the exposed aggregate finish.

4.4.3 Slab Specimen RB-3 (Ribbed Bars Fatigued at 2 Locations)

This specimen was subjected to fatigue loading at the centre of the panel for 2,000,000 cycles followed by 1,500,000 cycles adjacent to the closure strip. During fatigue loading, this specimen experienced failure due to fracturing of the bottom transverse GFRP reinforcement in the slabs. Initially, the specimen was saw cut to look more closely at the large crack which formed during this fatigue loading. Figure 4-99 shows a photo of the underside of the slab after it was turned over to examine the crack.

Figure 4-99. RB-3: Crack through the underside (shown up) of the slab and seen through a transverse cut through the slab.

It was determined that observing the bottom bars and their failure planes would be of use to understand what may have caused the bar failures. It was found that the top bars were undamaged. However, all bottom transverse bars were broken where they crossed the slab crack. Figure 4-100 shows a typical failure condition one of the reinforcing bars. Additional images are provided in Appendix A.

Figure 4-100. RB-3: Broken bar from bottom transverse reinforcement.

This failure type showed the bottom transverse bars to have fractured in a combination of tension and shear. The tension failure is due to the bending moment induced stress within the bar and the shear failure due to the shear force caused by the load acting directly adjacent to the crack, causing significant changes in shear stress in the slab. The fractures occurred near the edge of the load plate where shear stress would be greatest. The combination of these two failure modes caused the bars to fracture at a slight angle with the majority of the individual fibres fractured in tension. Another observation was that nearly all fractures occurred at the interior corner of a rib.

4.4.4 Slab Specimen RB-1 (Ribbed Bars Fatigued at 1 Location)

This specimen was subjected to fatigue loading adjacent to the closure strip for 1,735,000 cycles. At this point the slab failed due to fractures of the bottom transverse reinforcement. The slab was cut transversely to examine the depth of the crack, as shown in Figure 4-101.

Figure 4-101. RB-1: Crack through the slab, shown by cutting the slab transversely.

The conditions associated with the crack along the length of the slab were examined near the UHPC closure strip. The crack was observed to have followed the longitudinal reinforcement and extended through the closure strip as the slab was loaded to failure. Figure 4-102 shows a photo of the crack through the UHPC as well as a photo of one of the crack faces inside the UHPC closure strip. Note that the brown color in the photo on the right is a result of corrosion products from the steel fibres caused by the cracked specimen being placed outside for several days prior to autopsy.

Figure 4-102. RB-1: Crack through the UHPC closure strip as well as the interior of that crack.

All of the bars crossing the crack were removed for examination. All of the bottom transverse bars were broken while the top bars all remained intact. Figure 4-103 shows an example of the failure condition for one of the bottom bars. Additional photos are available in Appendix A.

Figure 4-103. RB-1: Failure location of one of the bottom transverse reinforcing bars.

Similar to Specimen RB-3, this failure type showed the bottom transverse bars to have fractured in a combination of tension and shear. The tension failure is due to the bending moment induced stress within the bar and the shear failure due to the shear force caused by the load acting on the bar. The fractures occurred near the edge of the load plate where shear stress would be greatest. The combination of these two failure modes caused the bars to fracture at a slight angle with the majority of the individual fibres fractured in tension. Another observation was that nearly all fractures occurred at the interior corner of a rib.

5 Predicted Slab Behaviour

This chapter compares the experimental behaviour of the precast slab specimens with predicted behaviour. Predicted slab behaviour was analysed by non-linear finite element (FEA) analysis using the commercial FEA software, ABAQUS. The slab behaviour was also predicted analytically using the provisions of two model codes: the Canadian building code requirements for concrete structures (CAN/CSA A23.3-04) and the Canadian Highway Bridge Design Code (CAN/CSA S6-06).

5.1 Finite Element Analysis of Slab Behaviour

ABAQUS is finite element software which allows for a wide variety of physical phenomena to be modeled. Of interest to this research is its ability to model solids using non-linear material properties, model the contact conditions between two surfaces, and provide contour plots indicating stress and strain locations throughout the material. The goal of utilizing this software was to create models that allow for a general understanding of the stresses and deformations which would be experienced by the experimental test setup. Additionally, the software provides contour plots for stresses and strains allowing for a better understanding of the global behaviour, rather than at discrete points in the experimental data.

The objective of this analysis was to understand the general behaviour of the slab under service load conditions and at failure loads. Due to the limited scope of this work, no mesh refinement or parametric analysis was completed. Any future research involving this model would require significant additional data regarding both material and contact properties. Additionally, a more in depth analysis would require parametric studies to identify the sensitivity of the analysis to changes of various parameters.

5.1.1 FEA Model Parameters

In order to build a model, several parameters required definition based on experimental data and engineering judgement. These parameters include material definitions, geometric definitions, element definitions, contact definitions, and boundary and support conditions.

5.1.1.1 Material Models

The concrete modeling used in the model was concrete damaged plasticity model. This model was selected over the two alternatives, smeared crack model and brittle crack model, due to its robust nature and ability to model concrete crushing failure in addition to the tension failure modelled by the two alternatives. The concrete compression is modeled as linear elastic initially until yield, at which point stress hardening governs until the ultimate concrete capacity is reached. Following the ultimate capacity, strain softening occurs. Figure 5-1 shows a plot of the uniaxial concrete compressive stress model used for concrete damaged plasticity (DSS, 2013).

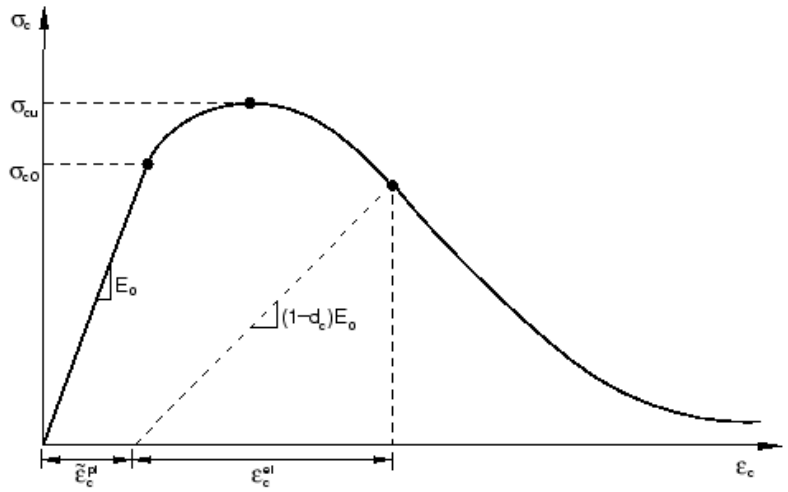

Figure 5-1. Uniaxial compressive stress behaviour of concrete (DSS, 2013)

In uniaxial tension, concrete is modeled as linear elastic until the ultimate tensile stress is reached. Following the creation of micro-cracking at the ultimate tensile stress, crack propagation leads to a strain-softening response post-peak stress. Figure 5-2 shows a plot of the general model used in concrete damaged plasticity to model concrete in tension.

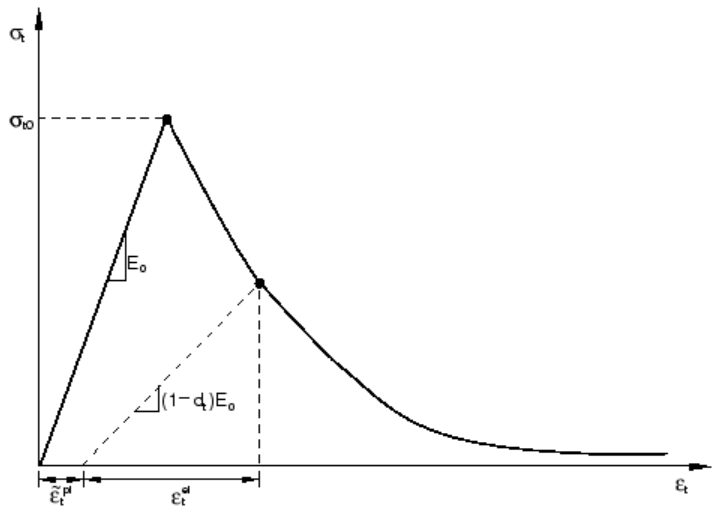

Figure 5-2. Uniaxial tension behaviour of concrete (DSS, 2013).

Three methods exist to define the modeling of the post-peak behaviour of the tensile response curve above; as a function of the cracking strain, a function of the crack-opening displacement, and as a prescribed value for fracture energy. The final method was utilized to model the tension stiffening in this research due to the availability of data based on the prism tests performed as well as the availability of values validated in previous research Figure 5-3 shows the linear stress-displacement curve that is assumed when utilizing this method, where the area under the curve, G_1, is the fracture energy prescribed. Note that this plot is in stress-displacement, rather than load-displacement shown in Chapter 4 to calculate the fracture energy. The difference between these two is that the area of the crack was input into the calculation of fracture energy after plotting the data whereas in Figure 5-3 the cracked area is utilized to find the stress used in the plot.

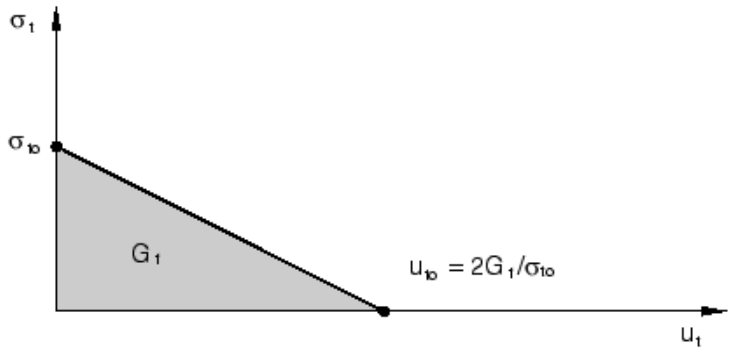

Figure 5-3. Fracture energy diagram for tension stiffening (DSS, 2013).

The concrete damaged plasticity model requires definition of several other parameters. Some of the concrete property data was defined based on the material properties determined experimentally (refer to Chapter 4) and the remaining properties were based work of a previous researcher (Stoner, 2015). Table 5-1 summarizes the prescribed values for the concrete material properties which were utilized for both types of concrete in the model.

Table 5-1. Concrete Properties for Damaged Plasticity Model

Property	Value
Dilation Angle	36
Eccentricity	0.1
F_{b0}/f_{c0}	1.16
K	0.667
Viscosity	0

Both the precast concrete and the UHPC were modeled utilizing the damaged plasticity model described above. These two types of concrete were assigned material-specific model parameters based on the material testing described in Chapter 3, as listed in Table 5-2.

Table 5-2. Concrete Properties for Precast and UHPC in Damaged Plasticity Model

Material	Elastic Modulus, E (GPa)	Poisson's Ratio, υ	Compressive Yield Stress, σ_{co} (MPa)	Compressive Ultimate Stress, σ_{cu} (MPa)	Tensile Ultimate Stress, σ_{t0} (MPa)	Fracture Energy, G_1 (N/mm)
Precast Concrete	32	0.15*	25*	45	3	0.1*
UHPC	50	0.2*	140	150	15.5	12

* indicates a recommended value

The GFRP was modeled using one general set of properties as a linear elastic material. This was done in lieu of prescribing properties for the sand-coated and ribbed bars since the properties were so similar and the purpose of this model was merely for general understanding and not specific values. The properties used to define the GFRP are listed in Table 5-3.

Table 5-3. GFRP Properties in ABAQUS.

Properties	Value
Young's Modulus	62.5 GPa
Poisson's Ratio	0.25
Yield Stress	1200 MPa

The final property which needed to be defined was steel. The steel was modeled as linear elastic to a yield stress of 350 MPa followed by a plastic behaviour to an ultimate failure stress of 450 MPa. The steel was utilized for both the support girder as well as the studs. The steel was defined as 350 W steel with properties defined in Table 5-4.

Table 5-4. Steel Properties in ABAQUS.

Properties	Value
Young's Modulus	200 GPa
Poisson's Ratio	0.3
Yield Stress	350 MPa

5.1.1.2 Element Definitions

The various elements of the model required different element definitions based on the specific characteristics of each component. Each component part of the model is meshed into elements with each containing a fixed number of nodes. A mesh refinement study was not completed for this analysis due to the preliminary nature of the model. For future finite element research regarding this model, a mesh refinement analysis would be required to maximize model accuracy.

The concrete was modeled using three dimensional quadratic tetrahedral elements called T3D10. This is a 4-noded element with only ten integration points to reduce computational load. These elements allow for the precast concrete to be modeled in three dimensions and for contact conditions to be defined between the UHPC and precast concrete panel. This type of element

was selected over similar three dimensional elements, such as cubes, due to its increased number of integration points per element. This allows for a decrease computational effort due to a reduced number of elements.

The GFRP was modeled using simple truss elements within the model. This was done utilizing 2-node linear truss elements referred to as T3D2. These elements are simple one dimensional objects that can only resist tensile or compressive forces, but are capable of being oriented in three dimensional space.

The steel girder was created utilizing plate elements for the flanges and the web. These elements were S4R elements, which are 4-node elements utilized for thin or thick shells. Finally, the shear studs (bolts) were beam using elements called B31. These elements are capable of transferring axial force, shear, and moment.

5.1.1.3 Geometric and Boundary Definitions

The dimensions of the setup were defined to be the same as the experimental setup described in Chapter 2. The GFRP reinforcing bars were embedded within the concrete panels and extended into the UHPC closure strip in which they were embedded. This embedment assumes a perfect bond between the reinforcement and the concrete substrate. Similarly, the studs were embedded into the concrete panels. However, the UHPC shear pockets were not explicitly modeled due to additional complexity. Based on engineering judgement, it was decided that the UHPC component of the shear pocket would have little effect on the overall stress and strain behaviour of the model. However, the studs were vital to the overall behaviour and they were positioned in the same locations in order to produce similar results to the actual stud pockets. The studs were then tied to the steel beam flange so that they act as a cantilever beam with the end attached to the flange acting as a fixed point. Figure 5-4 shows one of the stud regions in without the slab.

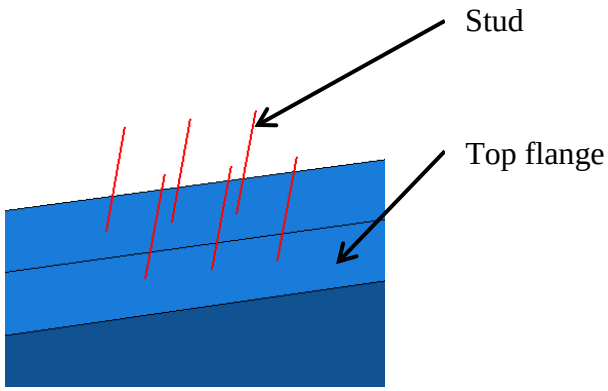

Figure 5-4. Stud cluster in FEA model (shown without slab).

The support conditions for the setup were idealized by restraining translation of the nodes the ends of the bottom flange at each end of each beam. These support points allowed rotation, but translation was restrained in all three principal directions. Finally, in order to reduce the computational demands, only half of the full specimen was modelled by applying a symmetry boundary condition at midspan of the precast slab specimen. This mirrors all components of the diagram to simulate the behaviour of the full model while only doing calculations for half of the entire experimental setup. Figure 5-5 shows a diagram of the model geometry.

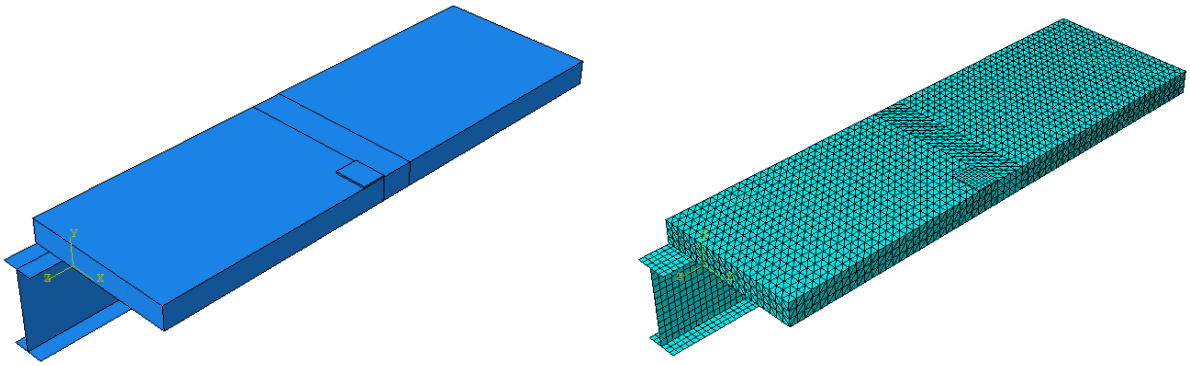

Figure 5-5. Geometry of ABAQUS FEA model (left) and native mesh (right).

5.1.1.4 Contact Conditions

One of the primary points of interest within the model is the contact behaviour between the UHPC and the precast slab concrete. Due to a lack of data regarding specific values of interaction properties between the UHPC and precast concrete at the closure strip interface, several parameters were defined based on engineering judgement. The first assumption was that

the cohesion between the two surfaces was negligible. The reason this assumption was made was to be a conservative estimate of the behaviour based on the separation noted after failure adjacent to the closure strip. The contact was defined as "hard". This parameter ensures that no overclosure will occur between the two surfaces.

The friction coefficient between the two surfaces was defined as 1.0. This value is based on literature indicating that this value can be used for concrete cast against an intentionally roughened existing concrete surface (NCHRP, 2007). This friction was defined as a penalty condition in which a force is allowed at contact points to ensure overclosure does not exist. The maximum shear stress was defined as 5 MPa. This value was selected based on engineering judgement as a place-holder value in lieu of available data. In order to gain a more accurate understanding of the behaviour of the interface between the two surfaces additional research would be required to evaluate values for the cohesion, friction, and shear capacity. Alternatively, future research would be required to perform a parametric analysis to evaluate the sensitivity of the model to these parameters.

5.1.2 Slab Behaviour at Service Load Levels

The first usage of the model was to apply the service load of 110 kN at each fatigue location and compare the model response to the experimental data. The data used for comparison are the initial static load cycle used for the specimens, which were only fatigued at one location and had static tests performed at the three load locations prior to any fatigue loading. In addition to the standard model with the UHPC closure strip, a continuous concrete model without the closure strip was also generated to compare the stress and behaviour change when the closure strip is present.

5.1.2.1 Model Results for Loading Adjacent to the Closure Strip

The load was applied adjacent to the closure strip as a pressure on a steel plate. The first point of comparison is the load-deflection curve from the FEA models versus that of the experimental data. Figure 5-6 shows the load deflection curves for the two models, with and without the closure strip, and the experimental responses for the two reinforcement types, ribbed and sand-coated. All diagrams showing load displacement were adjusted for the beam deflection in order

to isolate the slab deflection only. This was accomplished by removing the beam deflection from the measured deflection under the load in order to find the deflection of the slab only.

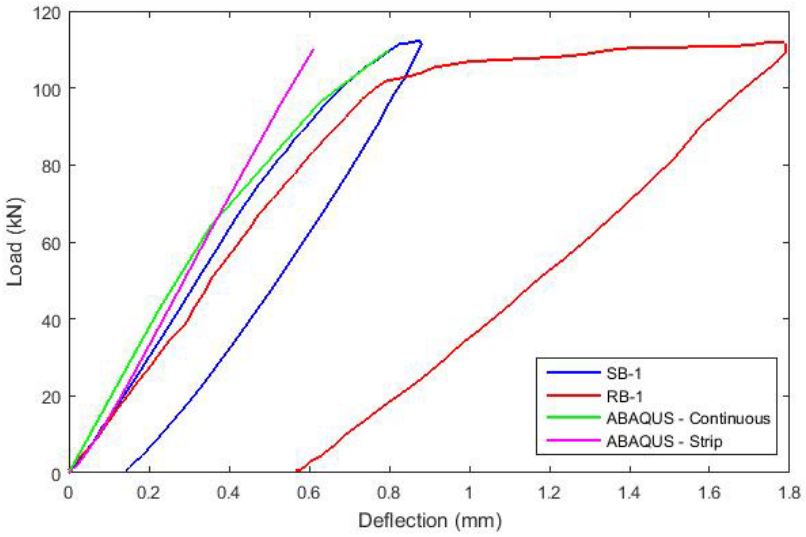

Figure 5-6. Comparison of load-deflection curves for ABAQUS and experimental setups for load adjacent to the closure strip.

The results show that the models were slightly stiffer than the experimental setup and only deflected to approximately 0.6 mm for the model with the closure strip and 0.8 mm for the continuous model compared to the experimental data which deflected 0.9 mm for the sand-coated bars and 1.8 mm for the ribbed bars. Another observation is that the continuous model seems to predict the onset of cracking at approximately 100 kN as the slope of the line decreases. The model with the closure strip appears to be linear elastic with no indication of cracking or loss of stiffness. Therefore, the continuous model coincides with the observed cracking, as both experimental data sets also experienced stiffness changes at approximately the same load level.

The concrete stresses experienced by the model were plotted as contours on the model. In order to simplify the output, the stresses of primary interest are those at the top and bottom face of the concrete in the two primary directions, lateral and longitudinal. Figure 5-7 shows a plot of the top and bottom faces of the concrete panels for the two models with the stress in the lateral direction shown. It is clear to see that, due to its relatively high stiffness, the UHPC sustains relatively high stress concentrations compared to the surrounding precast concrete. Additionally,

the closure strip causes stress discontinuities, whereas the continuous model has a smoother stress distribution.

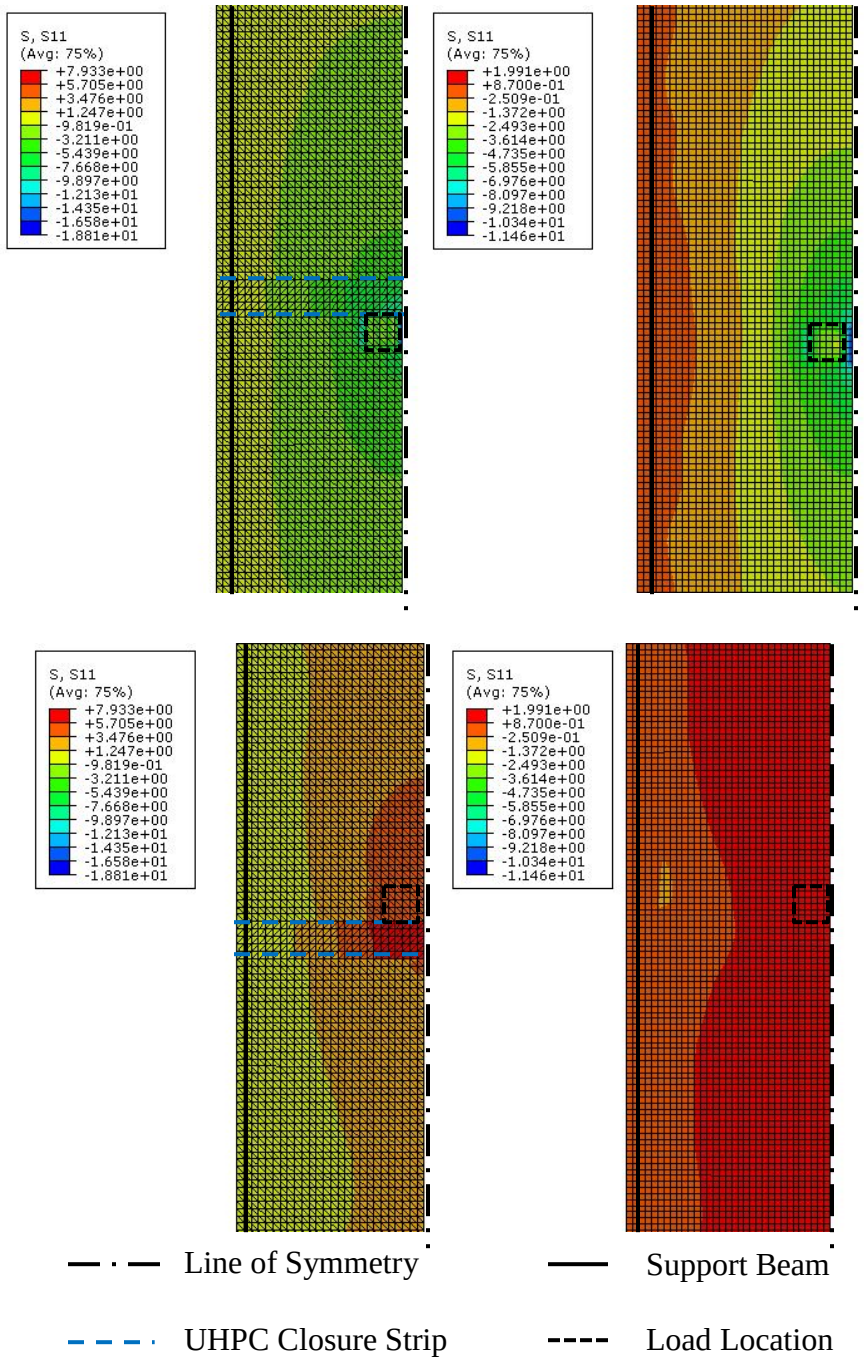

Figure 5-7. Stress diagrams in the transverse direction for load adjacent to the closure strip. (Top row: Top face, Bottom Row: Bottom face. Left side includes UHPC.)

The stress in the longitudinal direction was also plotted and can be seen in Figure 5-8. This shows similar characteristics to the transverse direction with the closure strip have sustaining

greater stress concentrations compared to the adjacent precast concrete due to the increased stiffness of the UHPC. The stud clusters can also be seen influencing the stress on the left side of the model on the bottom face.

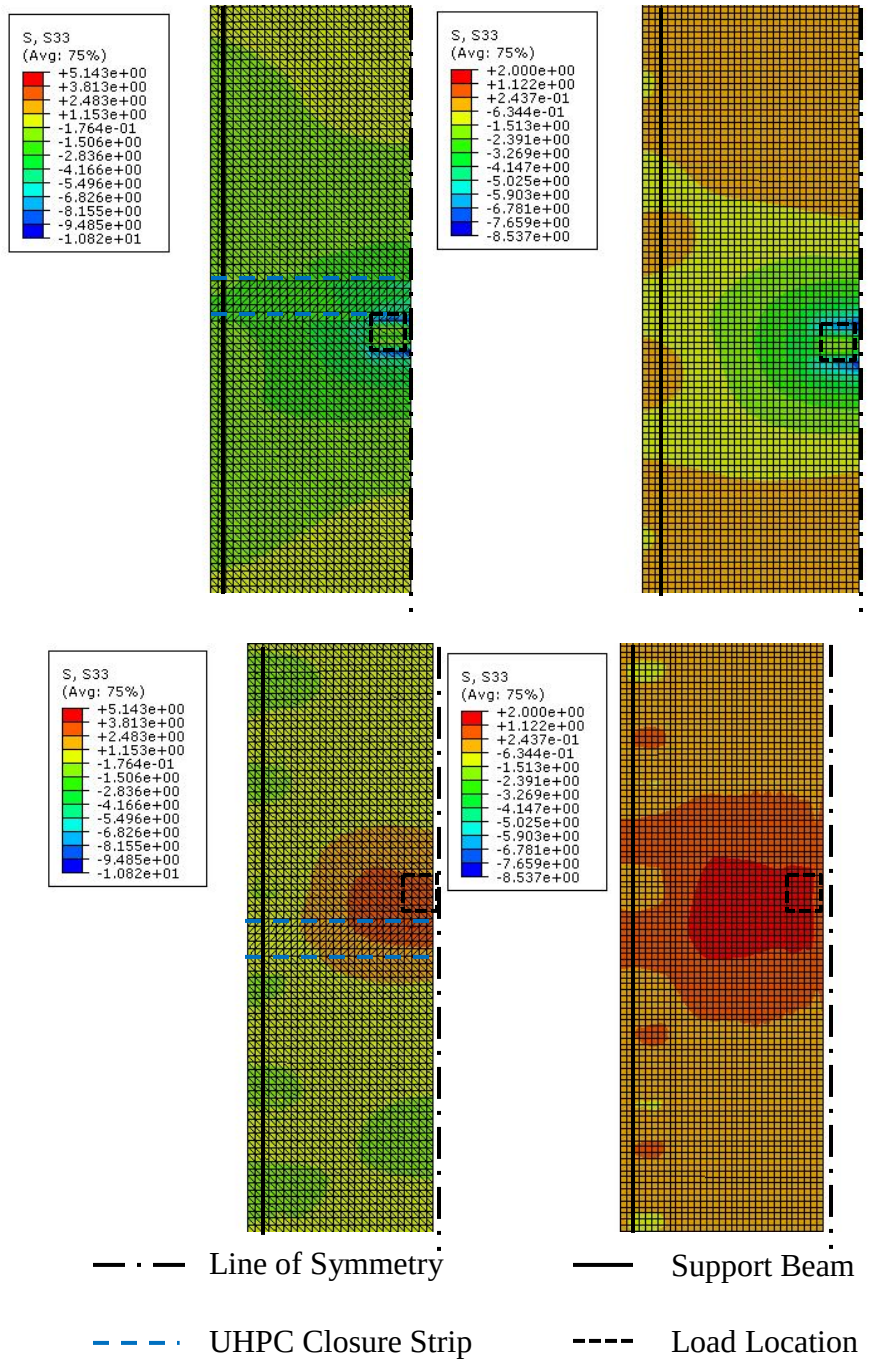

Figure 5-8. Stress diagrams in the longitudinal direction for load adjacent to the closure strip. (Top row: Top face, Bottom Row: Bottom face. Left side includes UHPC.)

The other significant point of interest in the model output is the variation of the maximum (tensile) principle strain as it correlates with the crack pattern of the slab under load. Only the underside of the slab is of interest since significant tensile strains were experienced on the top surface of the slab. Figure 5-9 shows the plot of maximum principle strain for the two models. Both models show maximum strain under the load point.

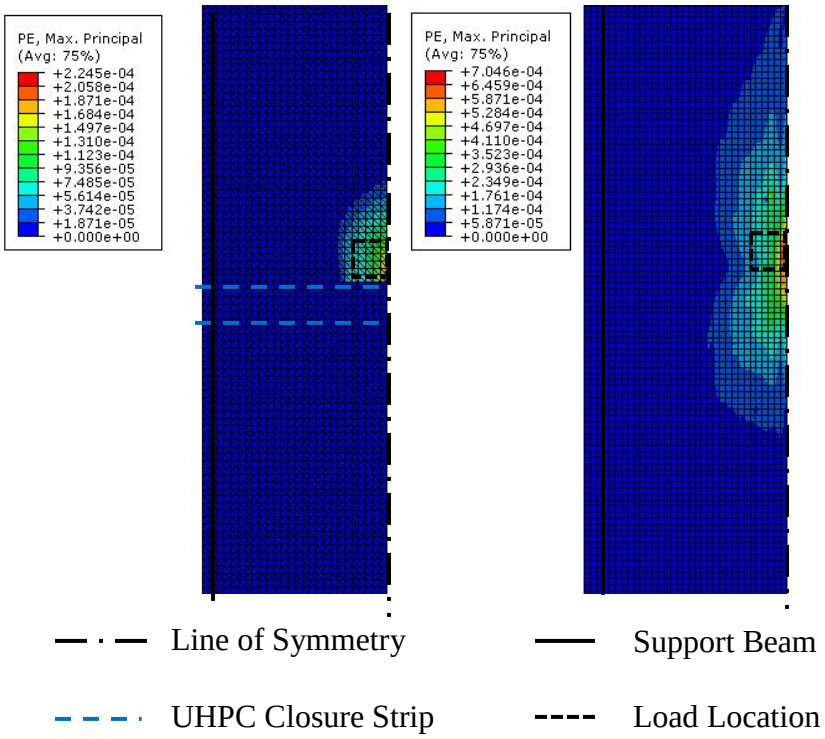

Figure 5-9. Maximum principle plastic strain diagrams for load adjacent to the closure strip (Left side includes UHPC.)

This diagram of maximum principle strain indicates that the UHPC closure strip truncates cracking of the loaded panel. This is likely due to its ability to withstand greater strains than normal strength concrete without cracking. Additionally, the presence of the steel fibres would help prevent cracking as shown in the model. This crack truncation is particularly noticeable when compared to the strain diagram for the model without the closure strip. This model clearly shows strains great enough to crack the concrete over a much larger area compared to the model with the closure strip.

5.1.2.2 Model Results for Loading at the Centre of the Panel

The load was applied on the centre of the precast panel or the equivalent location on the continuous concrete deck as a pressure on a steel plate. The first point of comparison is the load-deflection curve of the models versus that of the experimental data. Figure 5-10 shows the load-deflection curves for the two models, with and without the closure strip, and the experimental results for the two precast slabs with different reinforcement types, ribbed and sand-coated.

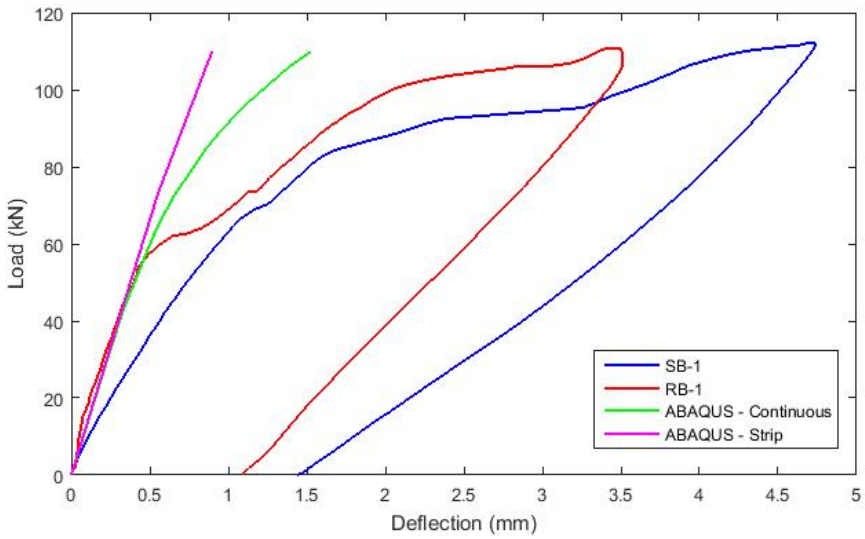

Figure 5-10. Comparison of load-deflection curves for ABAQUS and experimental setups for load on centre of panel.

It was observed that the model had similar stiffness to Specimen RB-1 initially and was stiffer than Specimen SB-1. Both the continuous model and the model with the closure strip failed to capture the bi-linear behaviour shown by both experimental data sets. There are a variety of reasons that this difference may exist. First, the model does not have any existing cracking prior to loading, whereas both experimental slabs were loaded prior to being loaded at this location. This prior loading may have decreased the slab stiffness causing the difference in initial stiffness. The lack of bi-linear behaviour by the models may be due to boundary conditions being set stiffer than the actual model. For instance, the support beam in the model may have greater stiffness near the edge of the slab due to the idealized support conditions, while the test setup had supports prone to settlement and differential stiffness based on the support beam. These changes in boundary conditions may have caused the free edge of the slab to become more stiff, limiting

one-way bending action and causing this location to act in two-way bending similar to the two central load locations..

The concrete stresses experienced by the model were plotted as contours on the model. In order to simplify the output, the stresses of primary interest are those at the top and bottom face of the concrete in the two primary directions, transverse and longitudinal. Figure 5-11 shows a plot of the top and bottom faces of the concrete panels for the two models with the stress in the lateral direction shown. It is clear to see that the stress distribution is fairly similar between the two models. The additional stiffness of the closure causes increased stresses within the strip creating stress discontinuities at the UHPC-precast concrete interface. However, compared to the stress discontinuities experienced in the models with the load applied adjacent to the closure strip, the stress contours are relatively continuous. This is likely due to the load being a sufficient distance from the closure strip to minimize the effect of the closure strip on the overall behaviour. This is reinforced when comparing the models with similar stress distributions between the model with the strip and without the strip.

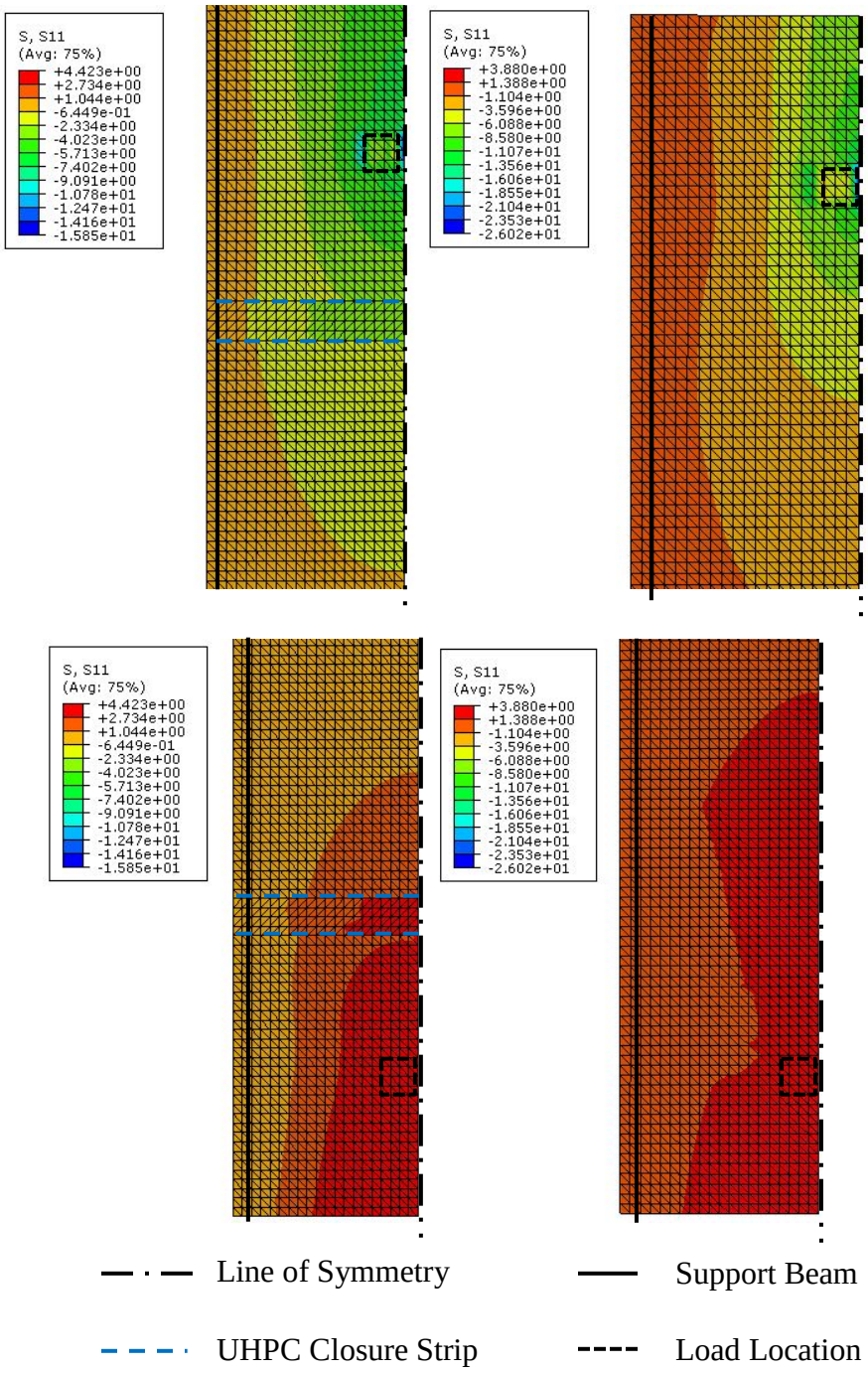

Figure 5-11. Stress diagrams in the lateral direction for load on centre of the precast panel. (Top row: Top face, Bottom Row: Bottom face. Left side includes UHPC.)

The stress distribution in the longitudinal direction was also plotted as shown in Figure 5-12. These figures show that the closure strip has little effect in the longitudinal direction when the load is applied away from the closure strip with minimal stress discontinuity between UHPC and

precast concrete interface. The stud clusters can also be seen influencing the stress on the left side of the model on the bottom face.

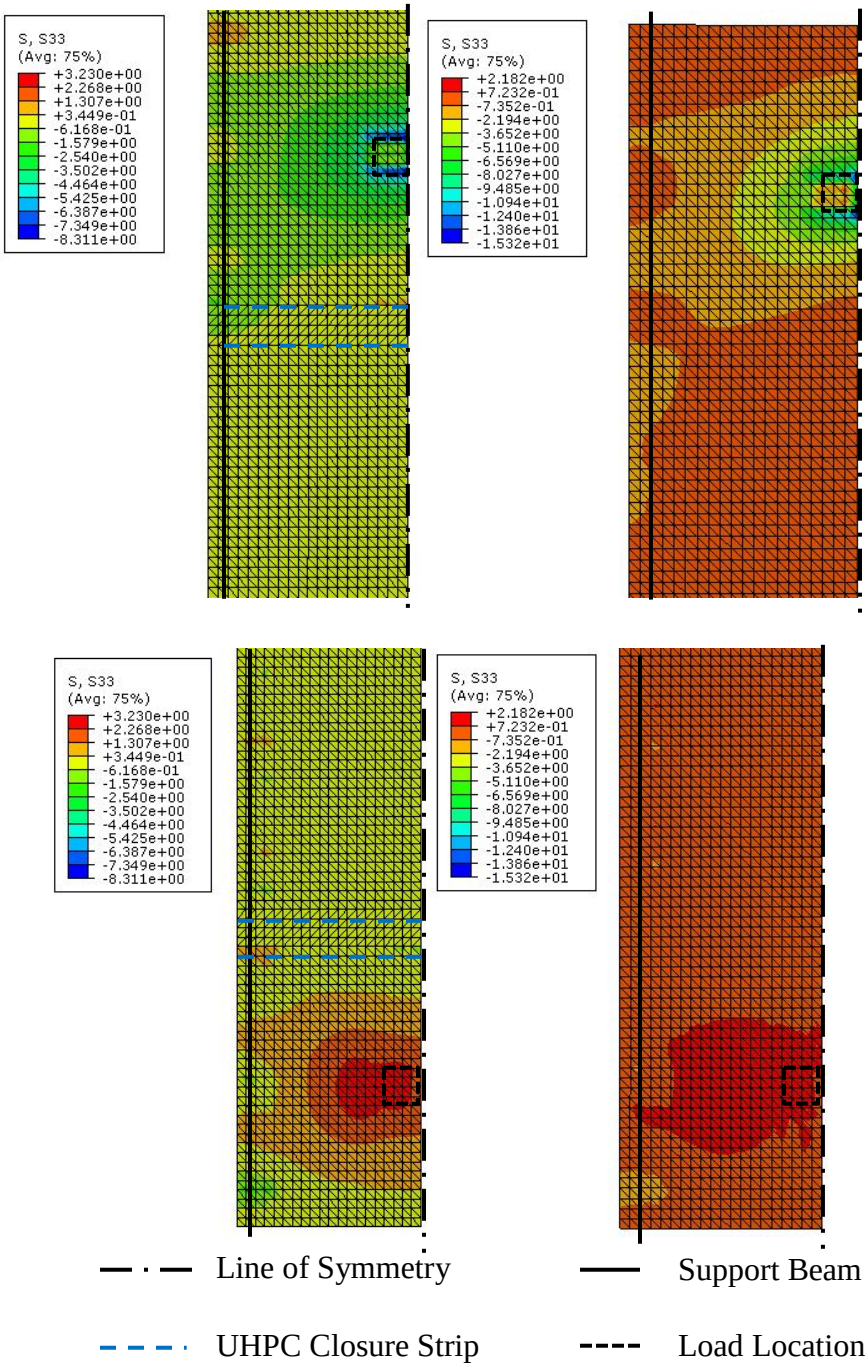

Figure 5-12. Stress diagrams in the longitudinal direction for load on centre of the precast panel. (Top row: Top face, Bottom Row: Bottom face. Left side includes UHPC.)

The other significant point of interest with these models is the ability to plot the maximum (tensile) principle strain. Figure 5-13 shows the plot of maximum principle strain for the two models. Both models show maximum strain under the load point.

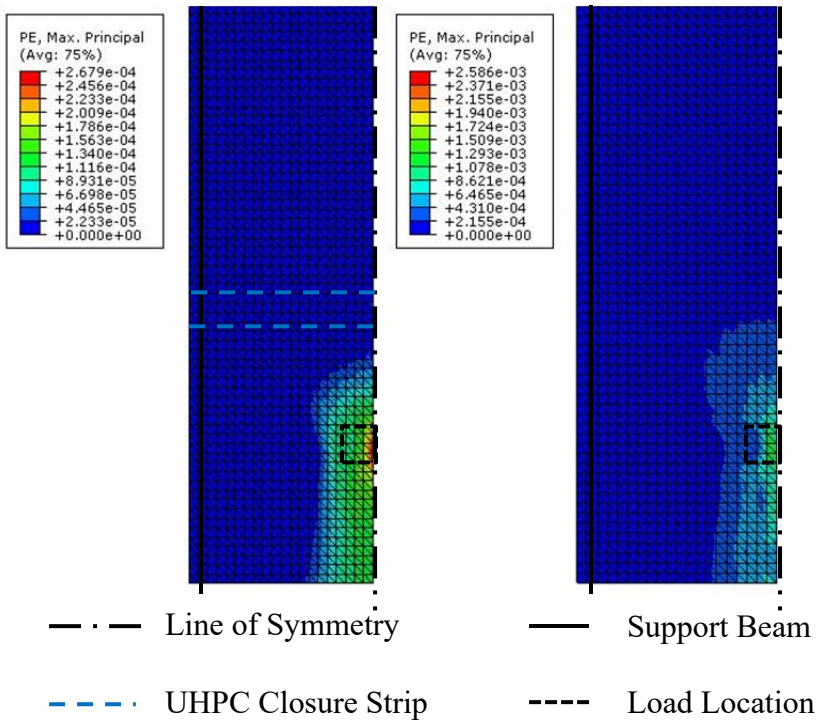

Figure 5-13. Maximum principle plastic strain diagrams for load on centre of the precast panel . (Left side includes UHPC.)

These plots show that the closure strip has negligible effect on the cracking behaviour of slabs loaded at this position. The two models are nearly identical in their crack pattern. The model with the UHPC closure strip does not have truncated crack patterns similar to the previous model with the load applied adjacent to the closure strip.

5.1.2.3 Model Results for Loading at Centre of Closure Strip

The load was applied on the centre of the UHPC closure strip or the equivalent location on the continuous concrete deck as a pressure on a steel plate. The first point of comparison is the load-deflection curve of the models versus that of the experimental data. Figure 5-14 shows the load deflection curves for the two models, with and without the closure strip, and the experimental results for the two precast slab specimens with ribbed and sand-coated reinforcement.

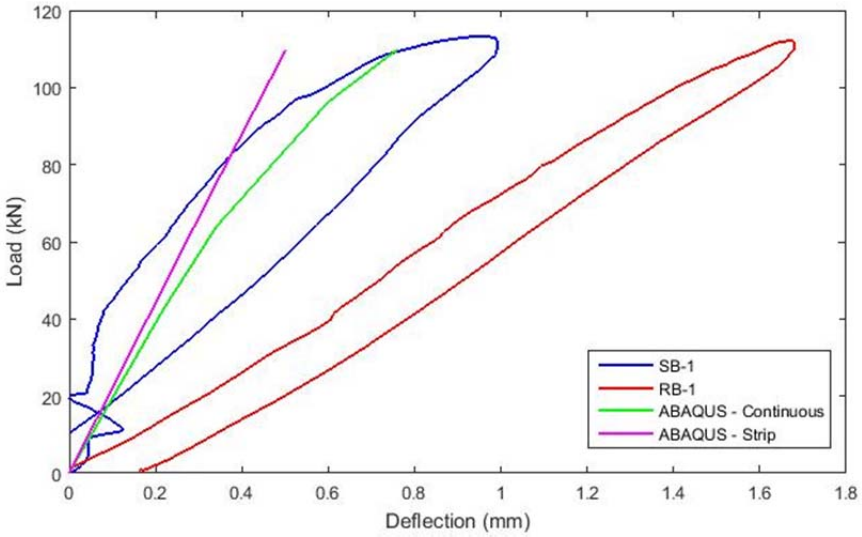

Figure 5-14. Comparison of load-deflection curves for ABAQUS and experimental setups for load on the closure strip.

The response of Specimen SB-1 was observed to be irregular due to the adjustment utilizing the beam deflection. The beam deflection data was non-linear early in the test with drastic changes in the measured deflection in both the positive and negative directions. This may have been caused by the displacement transducer 'sticking' under initial load, causing the data to appear irregular. It was observed that both models were more stiff than the experimental results. However, the stiffness of the models is much closer that observed with Specimen SB-1 while Specimen RB-1 displayed significantly less stiffness than either model. The primary cause of this decreased stiffness is the observed cracking which occurred when Specimen RB-1 was loaded adjacent to the closure strip prior to the load on the closure strip. Neither model exhibits cracking prior to the test. Similarly, no cracking was observed for Specimen SB-1 following the initial loading adjacent to the closure strip.. The model with the closure strip had an overall deflection of 0.5 mm while the model without the closure strip deflected 0.7 mm. These values are much less than the observed deflection in the experimental data sets with Specimen SB-1 deflecting 1.0 mm and Specimen RB-1 deflecting nearly 1.7 mm.

The concrete stresses experienced by the model were plotted as contours on the model. In order to simplify the output, the stresses of primary interest are those at the top and bottom face of the concrete in the two primary directions, transverse and longitudinal. Figure 5-15 shows a plot of

the top and bottom faces of the concrete panels for the two models with the stress in the lateral direction shown. It is clear to see that, due to its relatively high stiffness, the UHPC sustains slightly greater stress concentrations compared to the surrounding precast concrete. Additionally, the closure strip causes stress discontinuities at the UHPC-precast concrete interface, whereas the continuous model has a smoother stress distribution.

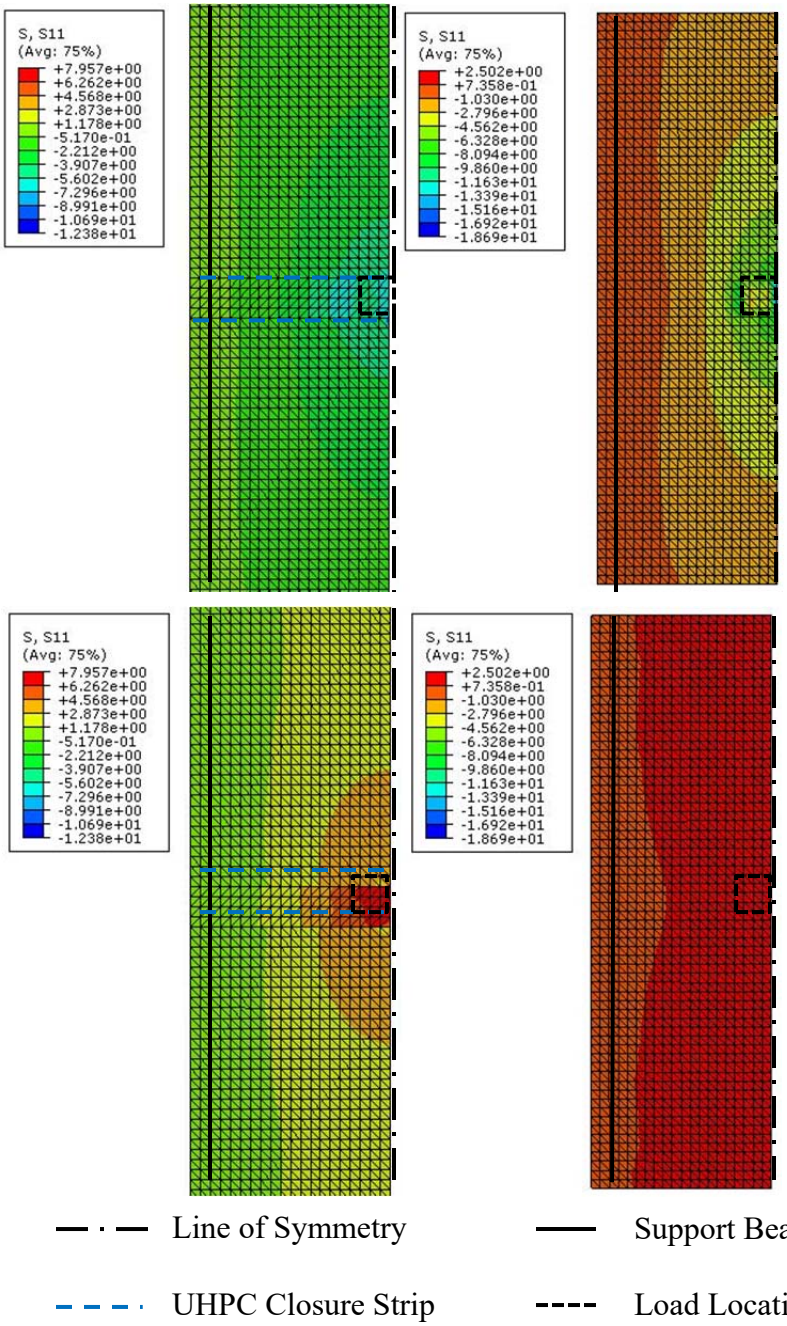

Figure 5-15. Stress diagrams in the lateral direction for load on centre of the closure strip. (Top row: Top face, Bottom Row: Bottom face. Left side includes UHPC.)

The stress in the longitudinal direction was also plotted and can be seen in Figure 5-16. This shows similar characteristics to the transverse direction with the closure strip have greater stress concentrations and causing stress discontinuity at the closure strip interface caused by the difference in stiffness between the normal strength precast concrete and the UHPC. The stud clusters can also be seen influencing the stress on the left side of the model on the bottom face.

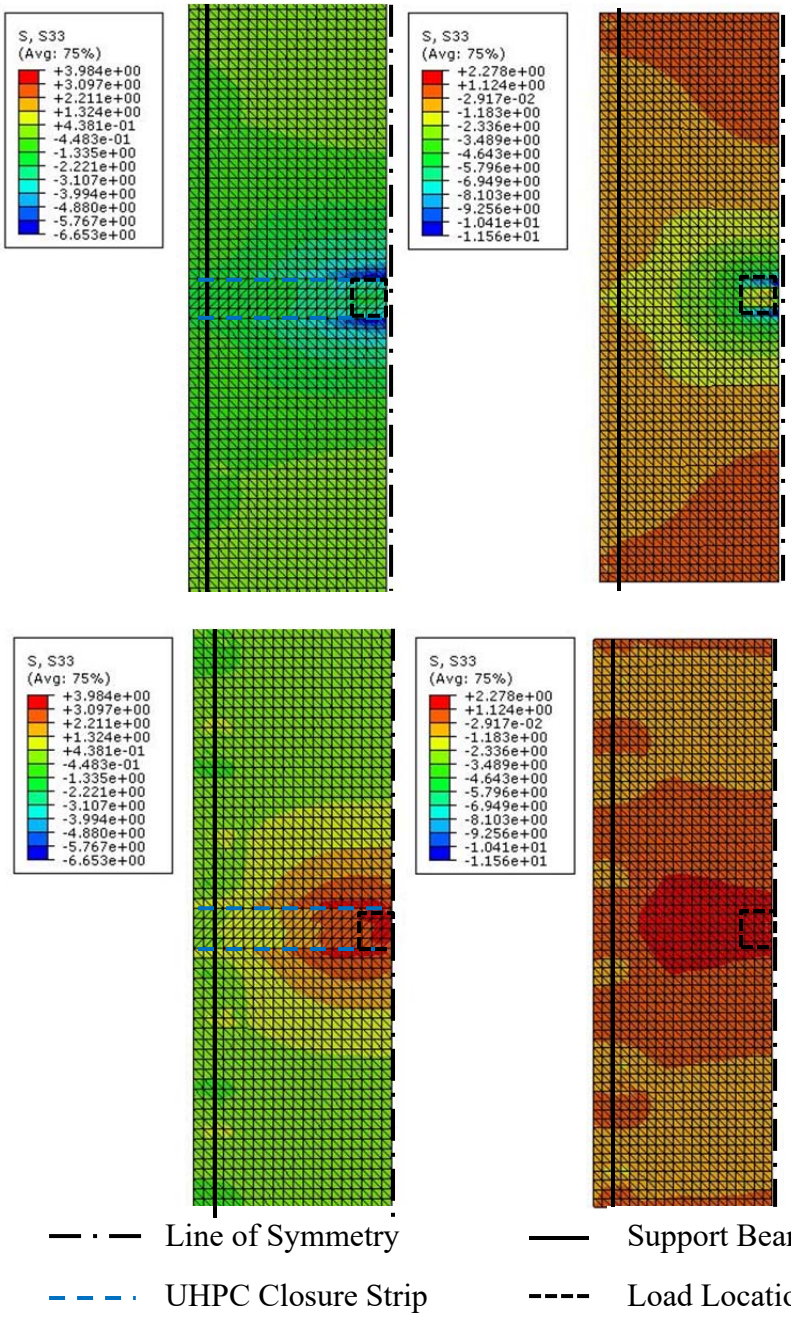

Figure 5-16. Stress diagrams in the longitudinal direction for load on centre of the closure strip. (Top row: Top face, Bottom Row: Bottom face. Left side includes UHPC.)

The other significant point of interest with these models is the ability to plot the maximum (tensile) principle strain. Figure 5-17 shows the plot of maximum principle strain for the two models. The model with the UHPC closure strip clearly shows less cracking than the hypothetical continuous model.

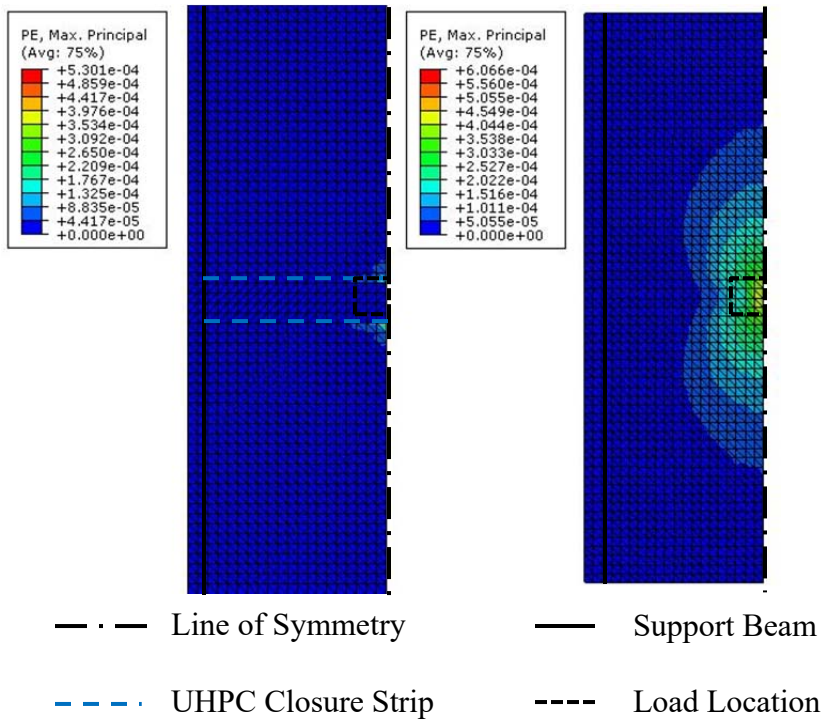

Figure 5-17. Maximum principle plastic strain diagrams for load on centre of the closure strip (Left side includes UHPC.)

This diagram of maximum principle strain indicates that the UHPC closure strip truncates cracking of the loaded panel on both sides of the closure strip. The cracked area is also significantly smaller than the cracked area of the continuous model. This is likely due to the ability of the UHPC to withstand greater strains than normal strength concrete without cracking. Additionally, the significant difference in stiffness between the UHPC and precast concrete causes a greater portion of the applied load be carried by the closure strip. This limiting of stress in the precast concrete also reinforces the reasoning for the decreased volume of cracks in the precast concrete.

5.1.3 Ultimate Load Locations

In addition to the predicted response at service load levels, the model was utilized to understand the failure mode of the slab. In order to model the ultimate behaviour of the slab while accounting for the effect of fatigue loading prior to loading to failure, several changes were imposed on the model parameters. The first change was to decrease the ultimate tensile strength in the precast concrete model parameters from 3 MPa to 2 MPa to represent the effect of the fatigue loading on the tensile strength of the panel concrete and increase the likelihood of cracking at lower applied load levels. The magnitude of this decrease was based on engineering judgement. The second change was to introduce a 2 mm wide, 100 mm deep crack through the UHPC closure strip at the centreline (line of symmetry) in the model geometry to simulate the precracked condition of the UHPC strip. The depth of the crack was approximated based on engineering judgement while the crack width was based on an average measured value.

Model loading was completed by imposing a set displacement on the load location. The displacement was set to continue for 65 mm based on the displacement observed in the experimental data at the time of failure. The load being applied through a fixed displacement was selected to coincide with the method of applying load to the test specimens. Figure 5-18 shows the experimental load-displacement plot for loading up to failure for the two specimens reinforced with sand-coated bars (SB-1 and SB-3) along with the FEA predicted response up to failure for the model with and without the UHPC closure strip.

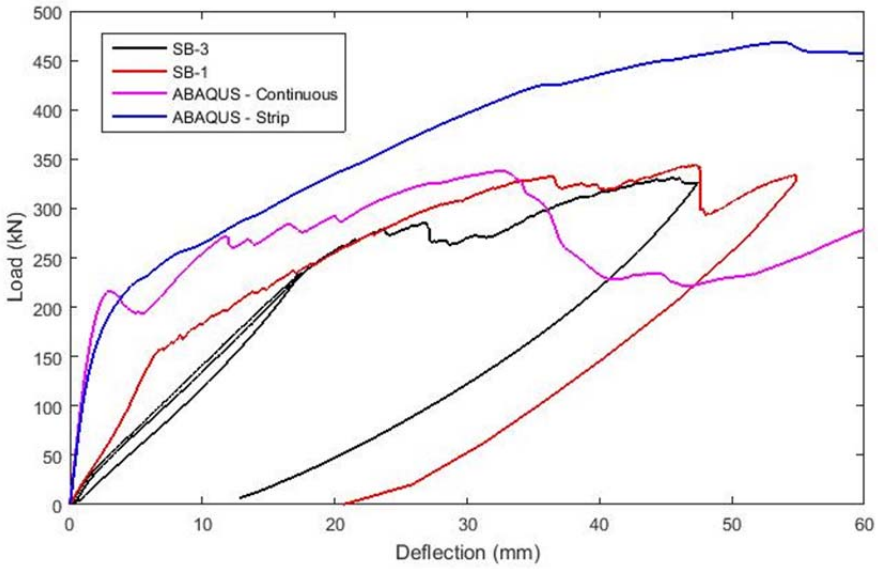

Figure 5-18. Load-deflection responses comparing ABAQUS models to experimental data for failure loads.

This plot shows that the FEA models display significantly greater stiffness than the experimental data during initial loading. The primary cause of this difference is due to the extent of cracking and stiffness loss caused by fatigue loading in the experiments; the models do not capture this stiffness loss. It was observed that the model without the closure strip failed at a load of 338 kN while and a deflection of approximately 32 mm. The model with the closure strip failed at a load of 468 kN at a deflection of approximately 52 mm. It is clear that the model predicts that the closure strip will increase the overall capacity of the slab, however the experimental data suggests that the behaviour is more similar to the modeled slab without the closure strip. This difference may be caused by differences between the model and the experimental data due to fatigue loading such as cracking at the interface, which was unobserved due to its small magnitude. Micro-cracks may have formed at the interface which would not be readily observable. Additionally, the contact conditions expressed in the model may be the cause of difference and further research would be required to accurately model these conditions.

In addition to the general behaviour shown above, the failure modes of the models were also a point of interest. The crack locations can be interpreted through the use of the maximum (tensile) principle strain diagram. Figure 5-19 shows the maximum principle strain diagrams for the model with the closure strip and the continuous model.

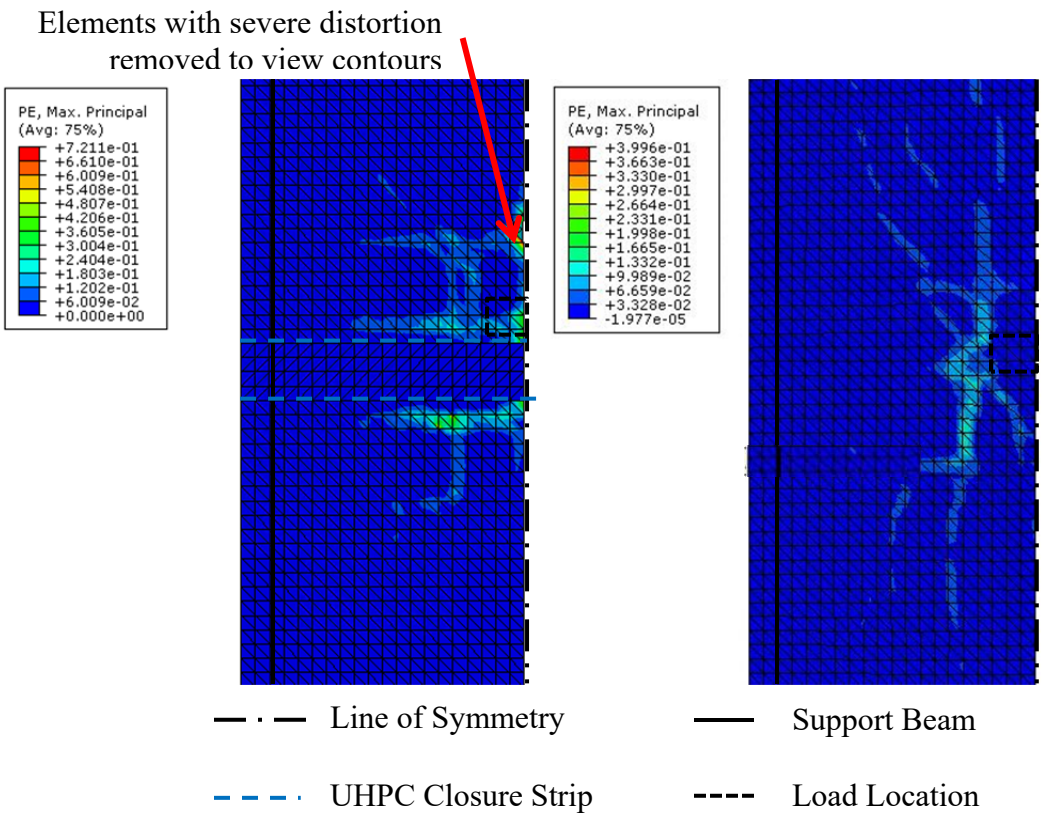

Figure 5-19. Maximum principle plastic strain diagrams after punching shear failure adjacent to the closure strip (Left side includes UHPC closure strip. Right side is continuous model.)

These maximum principle strain results show that both models fail with cracks in a fan or 'spider web' shape. One of the primary differences is that the UHPC closure strip does not show any cracks due to the existence of the pre-defined crack mentioned above. It can also be seen that there is separation between the UHPC closure strip and the precast concrete panels on both sides of the closure strip. However, the primary punching failure is only observed on the loaded panel. Several elements were removed in the figure shown due to deformation control discrepancies near the line of symmetry with the principle maximum strain (indicated by red arrow). This point of deformation caused the remaining cracks to be less visible on the figure due to the scale of the contour plot. This excessive deformation is likely inaccurate due to the boundary conditions prescribed.

5.2 Analytical Failure Load Prediction Using Code Provisions

Various building and bridge codes include provisions to estimate the anticipated punching shear strength of a slab for design purposes. The punching shear provisions of two codes are considered in the section and compared to the experimental results. The codes considered are the building code requirements for concrete structures, CAN/CSA A23.3-04 and the Canadian Highway Bridge Design Code, CAN/CSA S6-06. The slabs reinforced with ribbed bars were not be considered in this analysis since they failed through concrete crushing rather than punching shear.

5.2.1 CSA A23.3 Provisions for Punching Shear

The first code utilized to predict the failure load of slab adjacent to the closure strip was the punching shear provisions of CSA A23.3 (CSA, 2010), Clauses 13.3.3 and 13.3.4. Clause 13.3.4 predicts the failure shear stress as the minimum of Equation (16), Equation (17), and Equation (18).

$$v_c = \left(1 + \frac{2}{\beta_c}\right) 0.19 \lambda \phi_c \sqrt{f'_c} \tag{16}$$

$$v_c = \left(\frac{a_s d}{b_o} + 0.19\right) \lambda \phi_c \sqrt{f'_c} \tag{17}$$

$$v_c = 0.38 \lambda \phi_c \sqrt{f'_c} \tag{18}$$

Where β_c is the ratio of the long to short side of the load, α_s is a factor that adjusts the shear strength of concrete based on support dimensions, d is the distance from the extreme compression fibre to centroid of the tension reinforcement (mm), b_o is the critical section perimeter (mm), λ is factor for concrete density (1.0 for normal density concrete), ϕ_c is the resistance factor of concrete (1.0 for behaviour prediction), and f'_c is the compressive strength of concrete (MPa).

In order to apply the CSA A23.3 provisions to the deck loading position adjacent to the UHPC joint, it was assumed that the truncation of the failure cone by the UHPC had a similar effect to

that of an edge column. For this case, b_o is assumed to only occur on three sides of the loaded area at a distance of one-half of d from the load edge. As well, the bond between the precast panel and UHPC joint was assumed to be negligible, and the dowel action of the panel reinforcement extending into the UHPC joint was neglected. These assumptions were made in order to provide a conservative estimate of the punching shear capacity. In reality, the bond at the closure strip interface would have some shear capacity. This shear capacity would increase the predicted failure load compared to the three-sided failure by the area of the interface within the punching shear failure multiplied by the allowable shear stress. Using Equation (16) with β_c of 0.75 the shear stress was found to be 2.23 MPa. Using Equation (17) with α_s taken as 3 for a case with three planes of failure, the predicted failure shear stress for the load location adjacent to the panel would be 3.68 MPa, or with α_s taken as 4, the failure stress would be 3.27 MPa. Finally, Equation (18) finds a shear stress of 2.54 MPa. Based on this information, Equation (16) 13 governs both cases. For a four sided failure plane, the failure load is calculated to be 378 kN. However, assuming the failure area is the three sides of a punching failure cone defined by the depth of reinforcement and critical perimeter, b_o, the predicted punching shear failure load in this case is 226 kN using the shear stress from Equation (16). Figure 5-20 shows the load-displacement response up to failure for the two sand-coated specimens (SB-3 and SB-1) with the predicted failure loads for the three and four sided failure conditions shown.

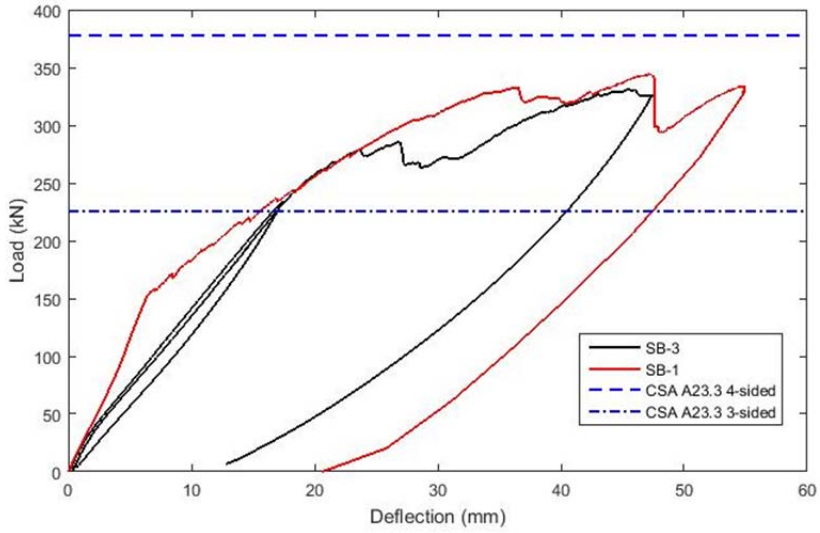

Figure 5-20. Comparison between CSA A23.3 punching requirements and experimental failure curves.

The difference between the actual punching shear capacity of the specimens and the code predicted value may be caused by the contribution of the shear or bond on the interface between the UHPC and precast panel which is insufficient to transfer the entire shear stress through the UHPC. Once the punching shear failure cone developed and slip occurred at the UHPC to precast concrete interface, the GFRP did not appear to provide significant shear resistance in dowel action. Based on the experimental results, CSA A23.3-04 cannot be directly applied to this load case. It is clear that assuming no shear stress transfer at the interface is overly conservative, however it is insufficient to calculate the failure as a typical four-sided punching shear failure. Further work would be required to modify the calculation of punching shear in this case to match the experimental data.

5.2.2 CSA S6 Punching Shear

The measured punching shear failure load was also compared to the punching shear strength predicted using the CAN/CSA S6 (CHBDC, 2013) Clause 8.9.4.3 provisions as given by Equation (19).

$$V_r = \left(\phi_c f_{cr} + 0.25 f_{pc}\right) b_o d + V_p \tag{19}$$

Where f_{cr} is the cracking strength of concrete (MPa), f_{pc} is the compressive stress in concrete after prestress losses (MPa), b_o is the critical section perimeter (mm), d is effective depth of reinforcement (mm), and V_p is the shear component from prestressing. For this case, it was assumed that b_o would be measured on the four sides of the loaded area and that d would be measured from the top fibre of the slab to the centroid of the bottom reinforcement layer. Using a resistance factor for concrete of 1.0 (for behaviour prediction rather than design strength) and omitting the prestressing contribution, V_p, since the deck was not prestressed, it was found that the calculated shear resistance of the slab should be 486 kN. This predicted value is significantly greater than the punching load experienced, however the predicted failure load does not account for pre-existing damage to the panel (from fatigue loading) and assumes that the failure plane is symmetrical and is centred on the load point. If the critical perimeter is reduced to three sides as observed in the experimental failure, the shear resistance of the slab is reduced to 291 kN.

Figure 5-21 shows the measured load-displacement behaviour for the two slab reinforcement types along with the predicted failure values.

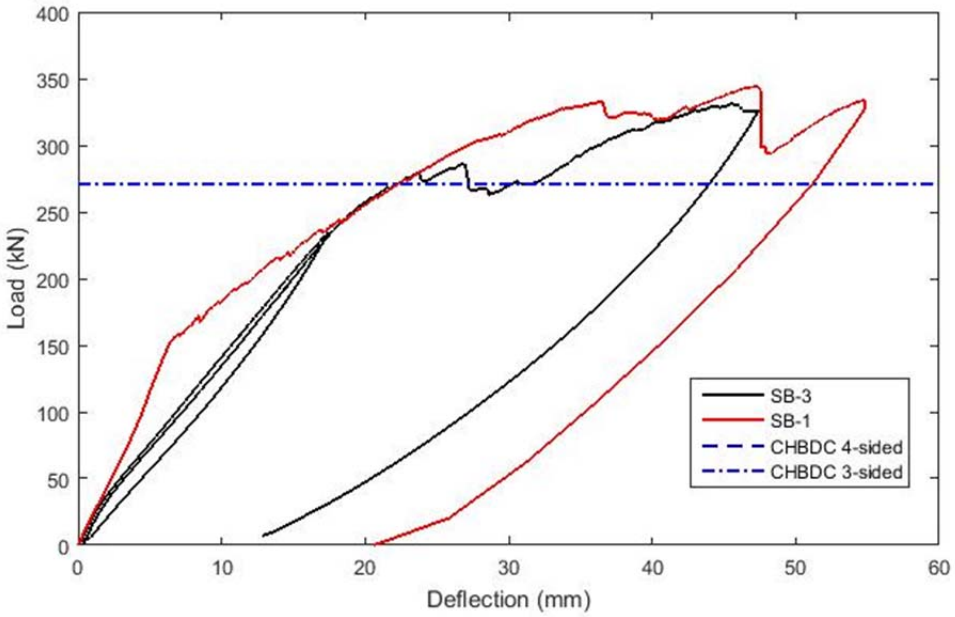

Figure 5-21. Comparison between CHBDC punching requirements and experimental failure curves.

Similar to the results of CSA A23.3-04 the experimental punching shear failures occur between the predicted four-sided and three-sided failure loads. Based on the experimental results, CSA S6 cannot be directly applied to this load case. It is insufficient to calculate the failure as a typical four-sided punching shear failure. However, the assumed three-sided failure with no shear contribution from the UHPC closure strip interface predicted a load similar to the punching load of Specimen SB-3 and about 50 kN less than Specimen SB-1. Therefore, the three-sided failure prediction may be a plausible model for the behaviour of the slab for this load condition. Further work would be required to collect a larger data sample to conclude if the three-sided failure prediction is accurate.

6 Discussion of Results

This chapter discusses the experimental and predicted results for the different specimens and models. This section explores the effects of various components of the testing and proposes future work to determine the effect of several parameters not evaluated in this research. The discussion includes behavioural effects due to: load location, bar type, fatigue, and presence of UHPC closure strip.

6.1 Effect of Load Location

The location of the load was observed to be a significant factor in the behaviour of the specimens. Comparing the load-deflection response of the second service load clearly shows that the specimen was significantly less stiff when the load was applied at the centre of the panel compared to the centre of the closure strip or adjacent to the closure strip. This behaviour was consistent for both types of bars. Figure 6-1 and Figure 6-2 show a comparison of the second static service load applied at the three locations for Specimen SB-1 and Specimen RB-1, respectively.

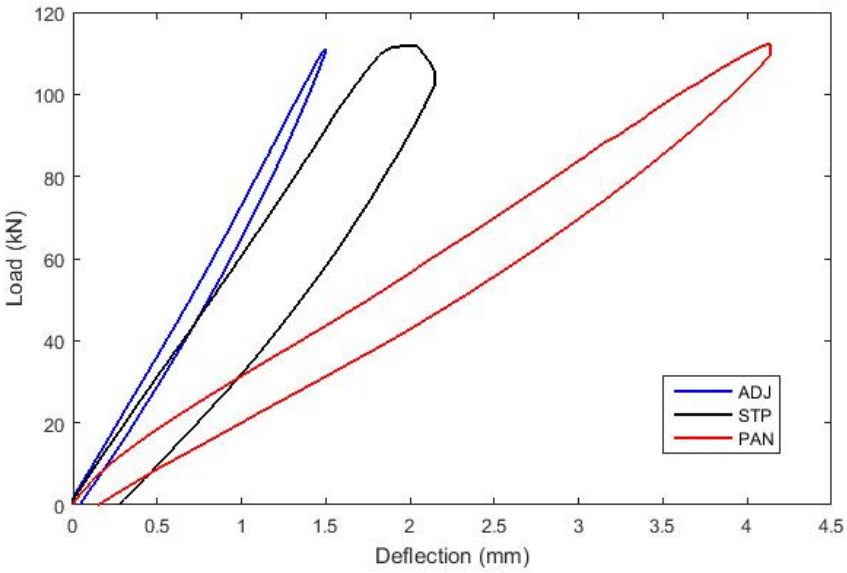

Figure 6-1. SB-1: Load-displacement response for second static load applied at the three load locations.

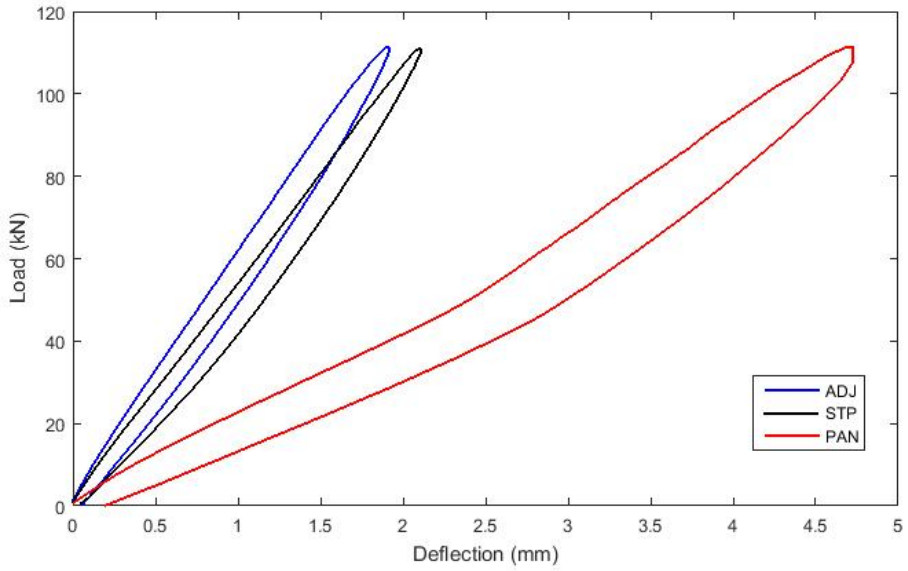

Figure 6-2. RB-1: Load-displacement response for second static load applied at the three load locations.

These plots also show that the slab is slightly less stiff when the load is applied on the centre of the closure strip compared to adjacent to the closure strip. This may be partially due to the lack of reinforcing bars within the closure strip, causing loads to be transferred away from the loading point, whereas the load adjacent to the closure strip is located directly above transverse bars (top and bottom). Alternatively, this minor difference may be due to the sequence loads were applied. Since the load was first applied adjacent to the closure strip, any cracking or damage from this load would have affected the response of the load applied on the centre of the closure strip due to their close proximity. The panel location is the least stiff due to the relatively close proximity of a free edge (slab edge unsupported by a beam). For the load adjacent to the closure strip the nearest free slab edge was 1350 mm away from the load edge. However, for the load on the centre of the panel, the nearest free edge is only 675 mm from the load edge. This causes half of the slab panel to act in one-way bending, while the other side behaves in two-way bending. Both central load locations behave in two-way bending due to the distance between the slab edge and the load.

Only Specimen SB-3 underwent fatigue loading at all three locations and was the only specimen to be loaded on the centre of the closure strip in fatigue. Figure 6-3 shows a diagram comparing the load deflection response for the three locations fatigued on Specimen SB-3.

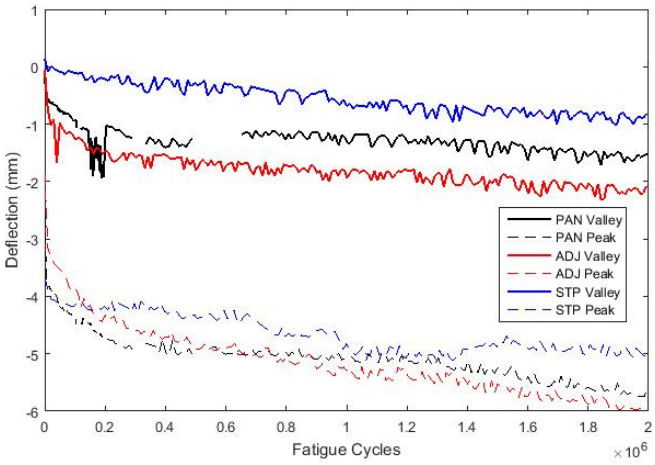

Figure 6-3. SB-3 Deflection response for the peak and valley loads for three load locations over fatigue loading.

During the fatigue loading, loads applied to both the centre of the panel and adjacent to the closure strip displayed similar initial behaviour as cracks propagated during the initial 20,000 cycles. This behaviour was not observed when fatigue loads were directly applied on the closure strip. The reason for this difference is likely due to the existing cracks caused by fatigue loading adjacent to the closure strip. Due to the close proximity of the two locations, any fatigue cracks caused by loading adjacent to the closure strip would have directly affected the behaviour of the slab when loaded on the centre of the closure strip. Additionally, any permanent deflection caused by fatigue loading at previous locations may have affected the response of the specimen at each location.

Specimen RB-3 underwent fatigue loading adjacent to the closure strip and on the centre of the panel. Figure 6-4 shows a comparison of the deflection caused by the peak and valley loads over the course of fatigue cycles.

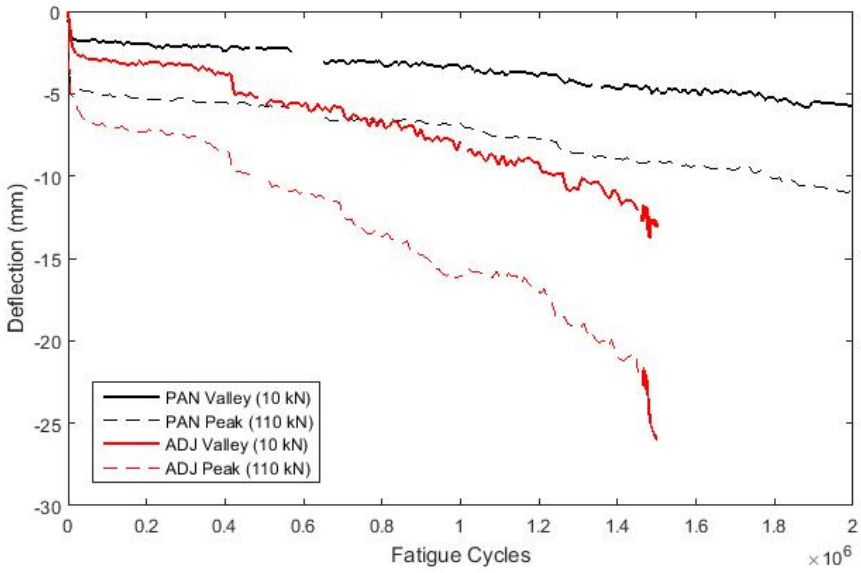

Figure 6-4. RB-3: Comparison of the deflection response to peak and valley loads under fatigue loads at two locations.

It is clear that the two data sets display significantly different behaviour. Following the initial cracking adjacent to the closure strip, the responses appear to decline at a similar rate for approximately 400,000 cycles. Beyond that point, when loading adjacent the closure strip the specimen began to deflect significantly due to the failure of bottom transverse bars. Therefore, due to the premature failure of the reinforcement, no definitive conclusions can be drawn from the effect of load location on the fatigue response of specimens reinforced with ribbed reinforcement.

6.2 Effect of Bar Type on Behaviour

The specimens tested clearly showed significant differences based on the type of reinforcement utilized. Both specimens reinforced with the sand-coated bars, SB-3 and SB-1, were able to undergo fatigue loading for the entire 2,000,000 cycles without any signs of failure. These fatigue tests were followed by both specimens being statically loaded to failure resulting in punching shear failures for both specimens. In contrast, both specimens reinforced with ribbed bars, RB-3 and RB-1, were unable to complete the fatigue load regimen due to premature failures of the bottom transverse bars. Both of these specimens failed through the top fibre of concrete crushing when loaded statically to failure. Figure 6-5 shows a plot of the peak and

valley strain on the bottom transverse bar below the applied load on the centre of the panel. Figure 6-6 shows the strain range of the reinforcement at the same location for the same load case.

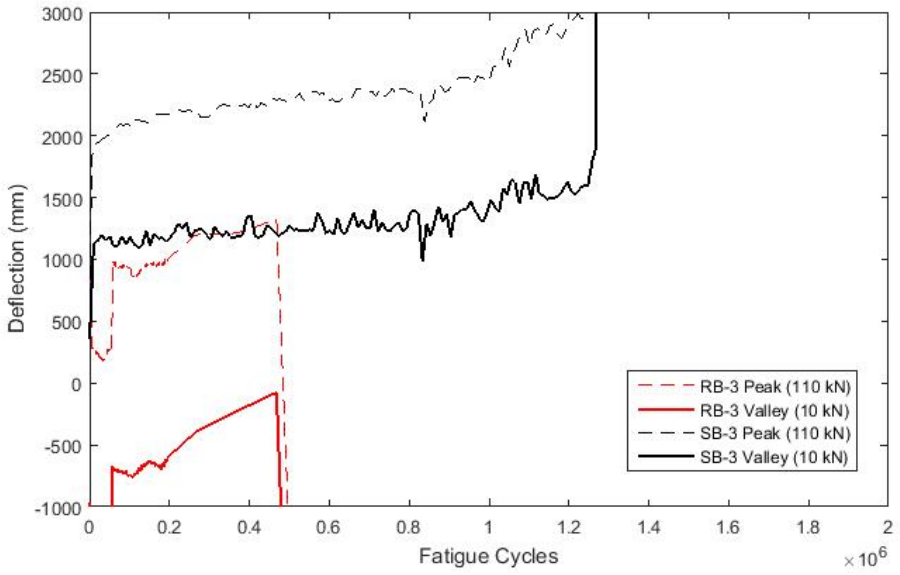

Figure 6-5. Strain peak and valley variation for bottom transverse bar below load on centre of panel.

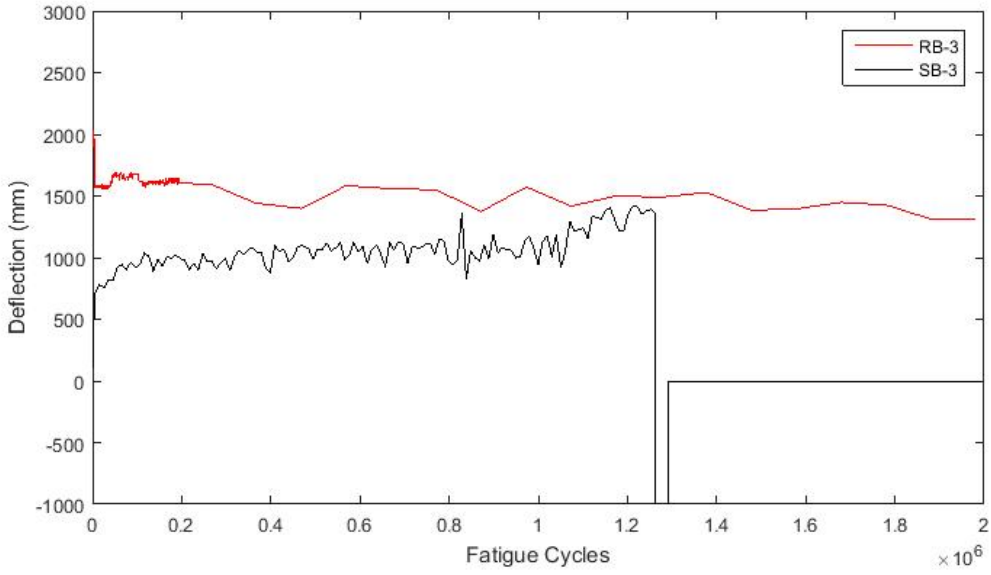

Figure 6-6. Strain range variation for bottom transverse bar directly below load on centre of panel.

These two figures show that the magnitude of strain was greater in the sand-coated reinforcement prior to gauge failure, however the strain range was slightly greater in the ribbed bars with an average value of approximately 1600 microstrain versus 1000 microstrain in the sand-coated bar. Unfortunately, due to the number of gauge failures during testing, no gauges located on bottom transverse bars were functional in specimens with each type of reinforcement and with the same load type to make direct comparisons. Therefore, further investigation is required to understand the strains experienced by each bar type and to evaluate the cause of the premature failure of the ribbed reinforcement.

6.3 Effect of Fatigue on Static Failure Results

Due to the limited number of specimens available for this research, no specimens were loaded to failure without sustaining fatigue loads prior to failure. Therefore, no conclusions on the effect of fatigue on failure results can be made based on experimental data. However, the FEA models were created without existing damage and can be used for a general understanding of the effect of fatigue on the failure results. It was clear that the model predicted a greater initial stiffness compared to the experimental results which was likely due to the presence of fatigue cracks prior to failure loads. Additionally, the models showed limited cracking compared to the cracks observed in actual testing, indicating that the fatigue at the various locations caused stiffness losses not captured by the model.

The ultimate capacity of slab was predicted to be greater than the observed value based on both code predictions (assuming four-sided failure) as well as the FEA model. However, it is unclear if this increased failure load was a result of the lack of fatigue damage in the model or an incorrect assumed parameter within the model. A parametric analysis of the various parameters would assist in understanding the affect these parameters have on the failure capacity of the slab. If it were determined that the parameters have a limited effect on the predicted failure capacity, a conclusion may be drawn that the difference in failure load is caused by the presence of fatigue damage. The code predicted three-sided failure was determined to be conservative despite the existing fatigue damage at the time of failure.

6.4 Effect of UHPC Closure Strip on Behaviour

Due to the limited number of specimens available, a continuous concrete specimen without a closure strip was not tested. Therefore, no conclusions from direct comparison can be drawn on the effect of the UHPC closure strip can be drawn from experimental data. However, it was noted during fatigue in that only one crack would form through the UHPC closure strip. This indicates that closure strip affected the crack pattern since the precast slabs were cracked in multiple locations and directions. Additionally, the closure strip clearly affected the punching shear failure due to the failure occurring on only three sides of the load.

However, the two FEA models created allow for a comparison between a slab with a closure strip and a continuous slab. Under service loads it was clear that the model with the UHPC closure strip increased the stiffness of the model relative to the continuous model. Similarly, at failure, the model with the UHPC closure strip sustained a greater load than the model without a closure strip. Further investigation is required to determine the effects of the closure strip on the behaviour of the slab. Particularly, a parametric study of the contact conditions at the interface between the UHPC closure strip and precast concrete would be required to determine the sensitivity of the model to changes in these parameters.

7 Conclusions

The research presented in this thesis examines the behaviour of prefabricated bridge deck panels utilizing closure strips filled with UHPC to connect panels transversely. Experimental tests were performed using nearly full scale bridge deck specimens undergoing fatigue loading and static loading to failure. The specimens were reinforced with either sand-coated or ribbed GFRP reinforcement. The experimental results are compared to ABAQUS finite element models to provide an understand of the stress patterns experienced by the slabs. The code predicted punching shear strengths of the decks are compared to the experimental behaviour.

7.1 Summary of Experimental Results

It was found that the slabs reinforced with the sand-coated GFRP bars behaved similarly regardless of where the loading was placed in fatigue. Each fatigue location showed the same behaviour of rapidly increasing deflection during initial fatigue cycles followed by a mild increase in deflection for the remainder of fatigue cycling. Following fatigue loading, the slabs were loaded to failure and failed through punching shear. When loaded adjacent to the closure strip, the punch cone was truncated by the UHPC for only a three sided failure, while loading at the centre of the panel resulted in a poorly defined punch cone due to existing damage from the failure adjacent to the closure strip. The slab that was fatigued at three locations (Specimen SB-3) failed at a load of 285 kN adjacent to the closure strip and 205 kN on the centre of the fatigued panel. The slab that was only fatigue adjacent to the closure strip (Specimen SB-1) failed at a load of 345 kN adjacent to the closure strip and 245 kN on the centre of the fatigued panel. Since no specimens were failed without prior fatigue loading, no experimental data was collected to ascertain the effect of fatigue on failure capacity. The only failure location that was not subjected to prior (direct) fatigue loading was the centre of the panel on Specimen SB-1. However, this location had undergone previous damage from the failure adjacent to the closure strip of this specimen and was therefore determined to behave differently from load locations near the closure strip based on static service load tests. Therefore, this data is inconclusive to compare the failure of a fatigued specimen to an unfatigued specimen.

The slabs reinforced with the ribbed GFRP bars had significant deflection increases throughout the fatigue loading. Neither slab was able to endure 2,000,000 cycles when cyclically loaded adjacent to the joint, as both experienced premature fatigue failures of the GFRP bottom (tensile) bars in the slab. These slabs were loaded to failure after fatigue cycling was stopped with both specimens failing when the top concrete fibre crushed.

7.2 Predicted Behaviour

Two finite element models were created in ABAQUS and used to compare the modelled results and the experimental results. One model was a continuous concrete slab and the other consisted of two slabs joined with a UHPC closure strip. These models were loaded similarly to the specimens in order to provide an understanding of the general slab behaviour including stress distributions. It was found that the models were typically stiffer than the experimental data initially. This difference in stiffness may be caused by model parameters requiring refinement or damage to the slab due to previous load tests.

The models that were loaded to failure showed similar behaviour with initial stiffness greater than the test setup due to the models being undamaged by fatigue loading. The continuous concrete deck model failed at a load similar to that observed in the tests, while the model with the UHPC closure strip had significantly greater ultimate capacity than that observed in the tests. The models also showed similar crack patterns to those noted on the experimental specimens, indicating that the UHPC closure strip was providing additional stiffness and causing three sided punching shear failures.

Two codes were utilized to predict the failure of the slabs in punching shear: CSA A23.3-04 and CSA S6-06. Both codes predicted a punching shear capacity greater than observed in the tests. This was due to both codes assuming a punching shear cone on all four sides of the load point and the test specimens failing on only three sides. When the code predictions were modified for three-sided failures, the predicted values were conservative compared to the experimental data. This indicated that the interface between the precast concrete and UHPC closure strip was able to withstand some shear stress, but not enough to reach the full, four-sided, failure predictions.

7.3 Recommendations for Future Work

It is recommended that future work be pursued in order to address some of the areas that this thesis was unable to cover. These recommendations include:

- Fatigue testing of full-scale bridge deck panels with multiple panels and closure strips in order to more accurately represent a full length bridge. This type of setup would allow for a more accurate comparison of the concrete panels in the centre to the behaviour near the closure strip due to consistent boundary conditions. Alternatively, a control specimen with no closure strip could be tested.
- Evaluate alternative joint shapes and designs including joints utilizing a shear key to increase the mechanical connection between the precast concrete and the UHPC as well as the possibility of including a single transverse bar within the closure strip to limit cracking through the UHPC. This potential increase in shear transfer between the UHPC closure strip and precast concrete panel may prevent slip at the interface during failure loads. This setup may result in failure loads similar to the code predicted values for a four-sided punching shear failure.
- Perform a refined FEA to evaluate the detailed aspects of the behaviour under fatigue loading and failure of slab. This new FEA model would require experimental data to define parameters for the contact conditions as well as the properties of fatigue damaged concrete. Additionally, a parametric study would be required to ascertain the sensitivity of the model response to changes in the various parameters. Finally, this model could include the ability to simulate fatigue damage.

References

AASHTO. (2012). AASHTO LRFP bridge design specifications. *Washington DC: American Association of State Highway and Transportation Office*.

AASHTO. (1980). T259-80 Standard method of test for resistance of concrete to chloride ion penetration. *American Association of State Highway and Transportation Office.*

ACI Committee 363. (1997). In Russell H. G., Moreno J. (Eds.), ACI 363R state-of-the-art report on high-strength concrete. *American Concrete Institute*.

ACI Committee 440. (2006). In Busel J. P., Shield C. K. (Eds.), ACI 440.1R-06 guide for the design and construction of structural concrete reinforced with FRP bars. *American Concrete Institute*.

Alves, J., El-Ragaby, A., & El-Salakawy, E. (2011). Durability of GFRP bars' bond to concrete under different loading and environmental conditions. *Journal of Composites for Construction, 15*(3), 249-262.

ASTM. (2011). C1609 - Standard test method for flexural performance of fibre-reinforced concrete (using beam with third-point loading). West Conshohocken, PA: *ASTM International*.

ASTM. (2011). C496 - Standard test method for splitting tensile strength for cylindrical concrete specimens. West Conshohocken, PA: *ASTM International*.

ASTM. (2015). C39 - Standard test method for compressive strength of cylindrical concrete specimens. West Conshohocken, PA: *ASTM International*.

ASTM. (1999). C944-99 - Standard test method for abrasion resistance of concrete or mortar surfaces by the rotating-cutter method. *ASTM International,*

ASTM. (2003). C666-03 - Standard test method for resistance of concrete to rapid freezing and thawing. *ASTM International,*

ASTM. (2003). C672-03 - Standard test method for scaling resistance of concrete surfaces exposed to deicing chemicals. *ASTM International,*

ASTM. (2005). C1202-05 - Standard test method for electrical indication of concrete's ability to resist chloride ion penetration. *ASTM International,*

ASTM. (2005). C1260-05 Standard test method for potential alkali reactivity of aggregates (mortar-bar method). *ASTM International,*

Au, A., Lam, C., & Tharmabala, B. (2010). Development of bolted deck slab system to expedite bridge construction. *8th International Conference on Short and Medium Span Bridges,* Niagra Falls, Canada. pp. 091-1.

Au, A., Lam, C., & Tharmabala, B. (2011). Investigation of closure strip details for connecting prefabricated deck systems. *PCI Journal, 56*(3), 75-93.

Baena, M., Torres, L., Turon, A., & Barris, C. (2009). Experimental study of bond behaviour between concrete and FRP bars using a pull-out test. *Composites Part B: Engineering, 40*(8), 784-797.

Biswas, M. (1986). Precast bridge deck design systems. *Journal - Prestressed Concrete Institute, 31*(2), 40-94.

Bouguerra, K., Ahmed, E. A., El-Gamal, S., & Benmokrane, B. (2011). Testing of full-scale concrete bridge deck slabs reinforced with fiber-reinforced polymer (FRP) bars. *Construction and Building Materials, 25*(10), 3956-3965.

Brunton, J., Bank, L. C., & Oliva, M. (2012). Punching shear failure in double-layer pultruded FRP grid reinforced concrete bridge decks. *Advances in Structural Engineering, 15*(4), 601-614.

Butler, L. (2012). Evaluation of recycled concrete aggregate performance in structural concrete. (Doctor of Philosophy, University of Waterloo).

Canadian Standards Association. (2004). *CSA standard A23.3-04: Design of concrete structures*. Canada: Cement Association of Canada.

Canadian Standards Association. (2013). *Canadian highway bridge design code* (Supplement No. 3 - March 2013 ed.). Mississauga, Ontario: Canadian Standards Association.

Cosenza, E., Manfredi, G., & Realfonzo, R. (1997). Behavior and modeling of bond of FRP rebars to concrete. *Journal of Composites for Construction, 1*(2), 40-51.

Culmo, M. P. (2011). *Accelerated bridge construction - experience in design, fabrication and erection of prefabricated bridge elements and systems* No. FHWA-HIF-12-013. Springfield, VA: National Technical Information Service.

Dassault Systemes Simulia (DSS). (2013). *ABAQUS 6.13 Analysis User's guide*. Providence, RI, USA:

Davalos, J. F., Chen, Y., & Ray, I. (2008). Effect of FRP bar degradation on interface bond with high strength concrete. *Cement and Concrete Composites, 30*(8), 722-730.

Dorton, R. A., Holowka, M., & King, J. P. C. (1977). Conestogo river bridge - Design and testing. *Canadian Journal of Civil Engineering, 4*(1), 18-39.

El-Ragaby, A., & El-Salakawy, E. F. (2011). Effect of severe environmental and loading conditions on GFRP-RC bridge deck slabs. *American Concrete Institute, ACI Special Publication, , 2.* (275 SP) pp. 1095-1114.

Gar, S. P., Head, M., Hurlebaus, S., & Mander, J. B. (2013). Comparative experimental performance of bridge deck slabs with AFRP and steel precast panels. *Journal of Composites for Construction, 17*(6)

Graybeal, B., & Tanesi, J. (2007). Durability of an ultrahigh-performance concrete. *Journal of Materials in Civil Engineering,* (October), 848.

Graybeal, B. A. (2007). Compressive behavior of ultra-high-performance fiber-reinforced concrete. *ACI Materials Journal, 104*(2), 146-152.

Graybeal, B. A., & Hartmann, J. L. (2003). Ultra-high performance concrete material properties. *Transportation Research Board Conference.*

Issa, M. A., Idriss, A., Kaspar, I. I., & Khayyat, S. Y. (1995). Full depth precast and precast, prestressed concrete bridge deck panels. *PCI Journal, 40*(1), 59-80.

Issa, M. A., Yousif, A. A., & Issa, M. A. (2000). Experimental behavior of full-depth precast concrete panels for bridge rehabilitation. *ACI Structural Journal, 97*(3), 397-407.

Khalafalla, I. E., & Sennah, K. (2013). Development of prefabricated bridge girder system with closure strips incorporating sand-coated GFRP bars with headed ends. *Proceedings, Annual Conference - Canadian Society for Civil Engineering, 3.* (January) pp. 2222-2231.

Kim, Y. H., & Trejo, D. (2014). Shear-transfer mechanism and design of shear connectors for full-depth precast deck panel system. *ACI Structural Journal, 111*(4), 935-944.

Kumar, S. V., & GangaRao, H. V. S. (1998). Fatigue response of concrete decks reinforced with FRP rebars. *Journal of Structural Engineering, 124*(1), 11-16.

Lafarge North America. (2016). *Ductal mechanical performances.* Retrieved 05/01, 2016, from http://www.ductal.com/en/wps/portal/ductal/6_5-Mechanical_performances

Lee, C. H., Kim, Y. J., Chin, W. J., & Choi, E. S. (2012). Shear strength of ultra high performance fiber reinforced concrete (UHPFRC) precast bridge joint. *RILEM State of the Art Reports*, Vol. 2, 413-420

Ma, J., Orgass, M., Tue, N. V., Dehn, F., & Schmidt, D. (23004). Comparative investigations on ultra-high performance concrete with and without coarse aggregate. *International Symposium on Ultra High Performance Concrete (UHPC)*, Kassel, Germany. (9)

Matthys, S., & Taerwe, L. (2000). Concrete slabs reinforced with FRP grids. II: Punching resistance. *Journal of Composites for Construction, 4*(3), 154-161.

NCHRP. (2007). Report 584: Full-depth precast concrete bridge deck panel systems. *National Cooperative Highway Research Program,*

Ocel, J., & Graybeal, B. A. (2007). Fatigue behavior of an ultra-high performance concrete I-girder. *Concrete Bridge Conference*,

Perry, V. H., Krisciunas, R., & Stofko, B. (2012). MacKenzie River twin bridges - The largest field-cast UHPC connections project in North America. *PCI Journal, 59*(2), 40-48.

Reza Esfahani, M., Rakhshanimehr, M., & Roohollah Mousavi, S. (2013). Bond strength of lap-spliced GFRP bars in concrete beams. *Journal of Composites for Construction, 17*(3), 314-323.

RILEM TC-50 FMC Fracture Mechanics of Concrete. (1985). Determination of the fracture energy of mortar and concrete by means of three-point bend tests on notched beams. *Rilem.*

Stoner, J. G. (2015). *Finite element modelling of GFRP reinforced concrete beams.* Unpublished Masters of Applied Science, University of Waterloo, Waterloo, ON, Canada.

Sullivan, S. R. (2003). *Behavior of transverse joints in precast deck panel systems.* Unpublished Master of Science, College of Engineering and Technology of Ohio University,

Swenty, M. K., Roberts-Wollmann, C. L., & Cousins, T. E. (2014). Transverse panel-to-panel connections for full-depth precast concrete bridge deck panels on continuous steel girder bridges : Part 1, experimental. *PCI Journal, 59*(2), 62-77.

Taylor, S., & Mullin, B. (2006). Arching action in FRP reinforced concrete slabs. *Construction and Building Materials 20,* 71-80.

Wambeke, B. W., & Shield, C. K. (2006). Development length of glass fiber-reinforced polymer bars in concrete. *ACI Structural Journal, 103*(1), 11-17.

Zheng, Y., Robinson, D., Taylor, S., Cleland, D., & Shaat, A. (2008). Analysis of compressive membrane action in concrete slabs. *Bridge Engineering, 161*(BE 1), 21.

Appendix A: Photos of Specimen Autopsies

Specimen SB-3

Figure A-1. SB-3: Top longitudinal bar fractured at UHPC interface.

Figure A-2. SB-3: Reinforcement after removal of the punched concrete cone.

Figure A-3. SB-3: Bottom matt after punched concrete removal.

Figure A-4. SB-3: Underside of shear pocket.

Figure A-5. SB-3: Underside of slab following concrete removal.

Figure A-6. SB-3: Underside of panel follow punch on centre of panel.

Specimen RB-3

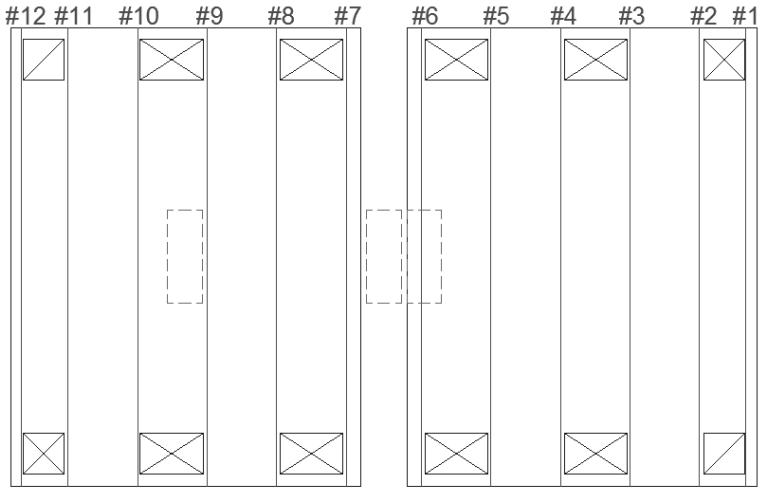

Figure A-7. RB-3: Transverse bar layout with bars numbered for reference.

Figure A-8. RB-3: Bottom Bar #1 fracture plane.

Figure A-10. RB-3: Bottom Bar #2 fracture plane.

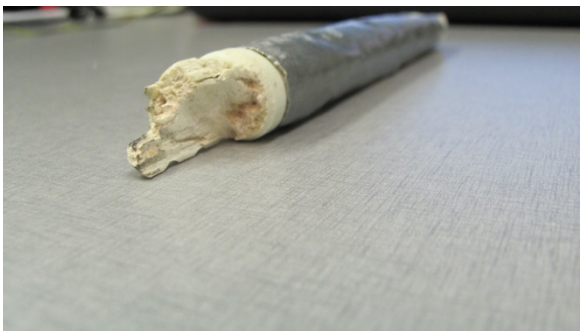

Figure A-9. RB-3: Bottom Bar #1 fracture surface.

Figure A-11. RB-3: Bottom Bar #2 fracture surface.

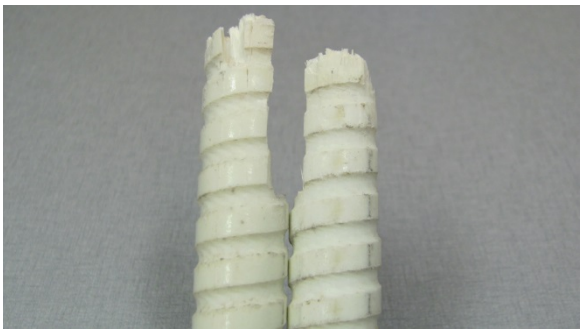

Figure A-12. RB-3: Bottom Bar #3 fracture plane.

Figure A-13. RB-3: Bottom Bar #3 fracture surface.

Figure A-14. RB-3: Bottom Bar #4 fracture plane.

Figure A-15. RB-3: Bottom Bar #4 fracture surface.

Figure A-16. RB-3: Bottom Bar #5 fracture plane.

Figure A-17. RB-3: Bottom Bar #5 fracture surface.

Figure A-18. RB-3: Bottom Bar #6 fracture plane.

Figure A-19. RB-3: Bottom Bar #6 fracture surface.

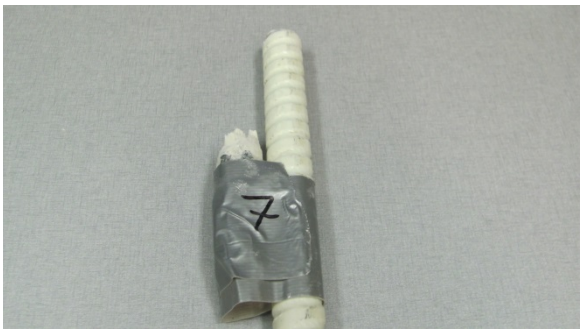

Figure A-20. RB-3: Bottom Bar #7 fracture plane.

Figure A-21. RB-3: Bottom Bar #8 fracture surface.

Figure A-22. RB-3: Bottom Bar #9 fracture plane.

Figure A-23. RB-3: Bottom Bar #9 fracture surface.

Figure A-24. RB-3: Bottom Bar #10 fracture plane.

Figure A-25. RB-3: Bottom Bar #10 fracture surface.

Figure A-26. RB-3: Bottom Bar #11 fracture plane.

Figure A-27. RB-3: Bottom Bar #11 fracture surface.

Figure A-28. RB-3: Bottom Bar #12 fracture plane.

Figure A-29. RB-3: Bottom Bar #12 fracture surface.

Specimen SB-1

Figure A-30. SB-1: Punch crack seen along section cut adjacent to load point in centre of panel.

Figure A-31. SB-1: Punch crack seen along cut adjacent to load point adjacent to closure strip.

Figure A-32. SB-1: Punch location adjacent to closure strip with concrete removed.

Figure A-33. SB-1: Underside of punch location with concrete removed.

Figure A-34. SB-1: Crack through UHPC.

Figure A-35. SB-1: Top view of punch location with concrete removed.

Specimen RB-1

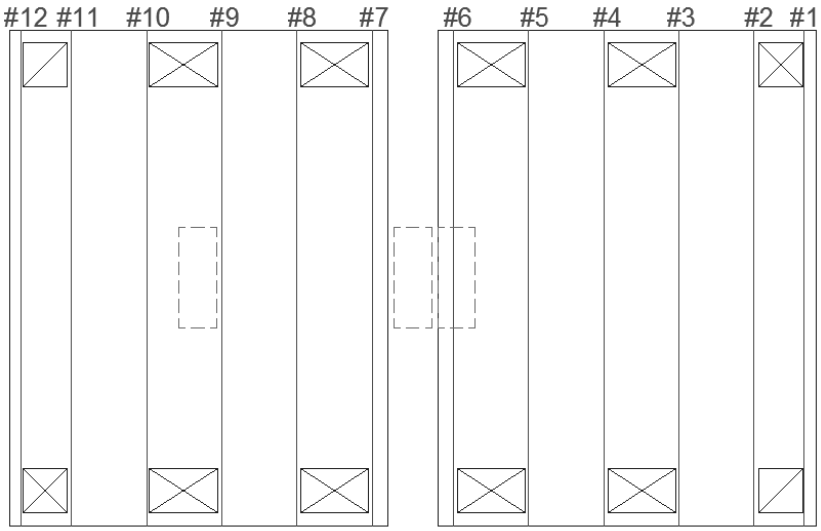

Figure A-36. RB-1: Transverse bar layout with bars numbered for reference.

Figure A-37. RB-1: Crushed concrete on top of specimen following failure.

Figure A-38. RB-1: Crack through UHPC (upside-down) at centre longitudinal bar.

Figure A-39. RB-1: Cut through longitudinal bars in UHPC closure strip.

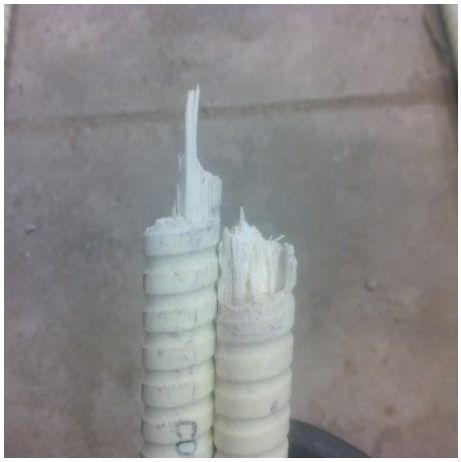

Figure A-40. RB-1: Bottom Bar #1 fracture plane.

Figure A-41. RB-1: Bottom Bar #1 fracture surface.

Figure A-42. RB-1: Bottom Bar #2 fracture plane.

Figure A-43. RB-1: Bottom Bar #2 fracture surface.

Figure A-44. RB-1: Bottom Bar #3 fracture plane.

Figure A-45. RB-1: Bottom Bar #3 fracture surface.

Figure A-46. RB-1: Bottom Bar #4 fracture plane.

Figure A-47. RB-1: Bottom Bar #4 fracture surface.

Figure A-48. RB-1: Bottom Bar #5 fracture plane.

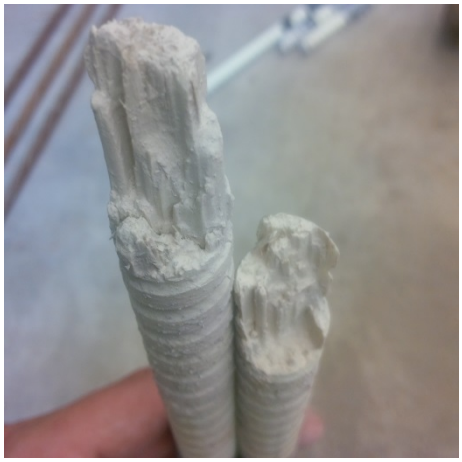

Figure A-49. RB-1: Bottom Bar #5 fracture surface.

Figure A-50. RB-1: Bottom Bar #6 fracture plane.

Figure A-51. RB-1: Bottom Bar #6 fracture surface.

Figure A-52. RB-1: Bottom Bar #7 fracture plane.

Figure A-53. RB-1: Bottom Bar #7 fracture surface.

Figure A-54. RB-1: Bottom Bar #8 fracture plane.

Figure A-55. RB-1: Bottom Bar #8 fracture surface.

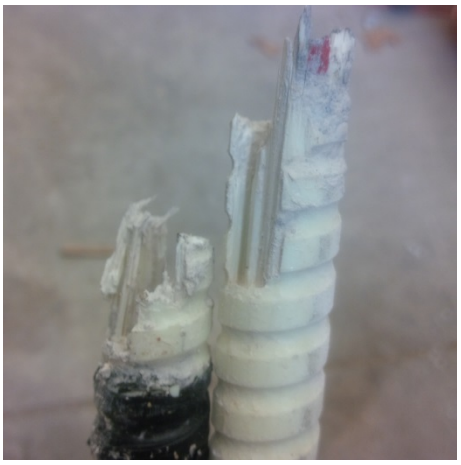

Figure A-56. RB-1: Bottom Bar #9 fracture plane.

Figure A-57. RB-1: Bottom Bar #9 fracture surface.

Figure A-58. RB-1: Bottom Bar #10 fracture plane.

Figure A-59. RB-1: Bottom Bar #10 fracture surface.

Figure A-60. RB-1: Bottom Bar #11 fracture plane.

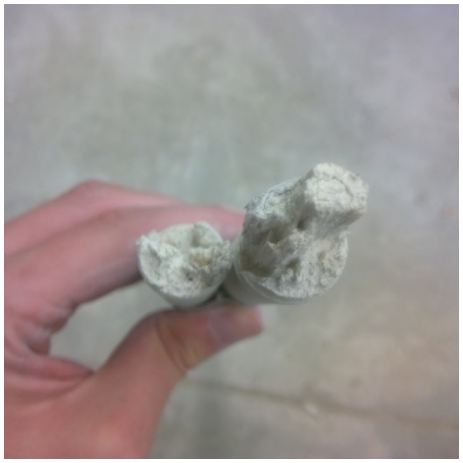

Figure A-61. RB-1: Bottom Bar #11 fracture surface.

Figure A-62. RB-1: Bottom Bar #12 fracture plane, bar still partially connected.

Appendix B: Calculations for Code Predictions

CSA A23.3 Calculations

Calculate shear stress based on Equation (16) (CSA A23.3 Eq-n 13-5)

$$v_c = \left(1 + \frac{2}{\beta_c}\right) 0.19 \lambda \phi_c \sqrt{f'_c}$$

where,

$\beta_c = 400/150 = 2.67$

$f'_c = 45MPa$

$\lambda = \phi_c = 1.0$

therefore,

$$v_c = \left(1 + \frac{2}{2.67}\right) 0.19\sqrt{45} = 2.23MPa$$

Calculate shear stress based on Equation (17) assuming four sided failure (CSA A23.3 Eq-n 13-6)

$$v_c = \left(\frac{a_s d}{b_o} + 0.19\right) \lambda \phi_c \sqrt{f'_c}$$

where,

$\alpha_s = 4$

$d = 110mm$

$b_o = 2(400 + 150 + 110 + 110) = 1540mm$

$\lambda = \phi_c = 1.0$

$f'_c = 45MPa$

therefore,

$$v_c = \left(\frac{4 \bullet 110}{1540} + 0.19\right)\sqrt{45} = 3.19MPa$$

Calculate shear stress based on Equation (17) (CSA A23.3 Eq-n 13-7)

$$v_c = 0.38 \lambda \phi_c \sqrt{f'_c}$$

where,

$\lambda = \phi_c = 1.0$

$f'_c = 45MPa$

therefore,

$$v_c = 0.38\sqrt{45} = 2.55MPa$$

Based on the stress calculated above, Equation (16) governs when assuming a four sided failure. In order to calculate the punching load, the stress is multiplied by the critical perimeter and d.

$$V_c = \upsilon_c \bullet b_o \bullet d = 2.23(1540)(110)$$

$$\boxed{V_c = 377.8kN}$$

Calculate shear stress based on Equation (17) assuming three sided failure (CSA A23.3 Eq-n 13-6)

$$\nu_c = \left(\frac{a_s d}{b_o} + 0.19 \right) \lambda \phi_c \sqrt{f'_c}$$

where,

$\alpha_s = 3$

$d = 110mm$

$b_o = 2(150 + 55) + 400 + 110 = 920mm$

$\lambda = \phi_c = 1.0$

$f'_c = 45MPa$

therefore,

$$\nu_c = \left(\frac{3 \bullet 110}{920} + 0.19 \right) \sqrt{45} = 3.68MPa$$

Since the shear values for Equation (16) and Equation (18) remain the same, Equation (16) still governs, therefore, for a three sided failure the punching load would be:

$$V_c = \upsilon_c \bullet b_o \bullet d = 2.23(920)(110)$$

$$\boxed{V_c = 225.7kN}$$

CSA S6 Calculations

Calculate shear stress based on Equation (19) for a four-sided failure (CSA S6 Cl. 8.9.4.3)

$V_r = \left(\phi_c f_{cr} + 0.25 f_{pc}\right) b_o d + V_p$

where,

$\phi_c = 1.0$

$f_{cr} = 0.4\sqrt{f'_c} = 0.4\sqrt{45} = 2.68 MPa$ (Normal-density)

$f_{pc} = V_p = 0$

$d = 110 mm$

$b_o = 2(400 + 150 + 110 + 110) = 1540 mm$

Therefore,

$V_r = (2.68)(1540)(110)$

$\boxed{V_r = 454.0 kN}$

Calculate shear stress based on Equation (19) for a three-sided failure (CSA S6 Cl. 8.9.4.3)

$V_r = \left(\phi_c f_{cr} + 0.25 f_{pc}\right) b_o d + V_p$

where,

$\phi_c = 1.0$

$f_{cr} = 0.4\sqrt{f'_c} = 0.4\sqrt{45} = 2.68 MPa$ (Normal-density)

$f_{pc} = V_p = 0$

$d = 110 mm$

$b_o = 2(150 + 55) + 400 + 110 = 920 mm$

Therefore,

$V_r = (2.68)(920)(110)$

$\boxed{V_r = 271.2 kN}$